# Efficiency calibration of a gamma-ray detector for measuring environmental radiation

**Avuyile Sisanda Bulala**

A thesis submitted in fulfilment of the requirements for the degree of Master of Science in the Department of Physics, University of Cape Town

**Supervisors:** Prof. Saalih Allie, Dr. Peane P. Maleka and Dr. Ntombizikhona B. Ndlovu

Department of Physics, University of Cape Town

Department of Subatomic Physics, iThemba LABS, Cape Town

12th August 2020

# Declaration

I know the meaning of plagiarism and hereby declare that this thesis is my own work and effort and that it has not been submitted anywhere for any award. Where other sources of information have been used, they have been acknowledged.

Signature: ... Signed by candidate ...............................................................

Date: ..........12 August 2020..........................................................................

# Abstract

The Environmental Radioactivity Laboratory (ERL) of iThemba LABS conducts research into levels of natural and anthropogenic radioactivity in the environment. The laboratory-based measurements are conducted using a low-background Hyper Pure Germanium (HPGe) detector system. A critical aspect of such measurements involves calibrating the detector about energy and detection efficiency. The present study details experiment that were carried to determine both energy and efficiency calibrations for various sample geometries using gamma-ray spectrometry.

The measurements using reference sources of known activity were carried out using two sample holders (Marinelli Beaker (1000 ml) and, a cylindrical pill bottle (100 ml)), and a point source. The IAEA reference materials (RGU-1, RGTh-1 ore and RGK-1) were prepared and used to fill the Marinelli beaker and pill bottles. Certified reference point sources ($^{60}$Co, $^{152}$Eu, $^{137}$Cs, $^{22}$Na, $^{241}$Am and $^{133}$Ba) were obtained from the National Metrology Institute of South Africa (NMISA).

Experiments consisted of exposing the HPGe detector to various gamma-ray sources prepared using various sample holders and the point source geometry. The counting time for each measurement was 24 hours. Each spectrum was analysed by inserting region of interests around suitably selected photo-peaks and the counts associated with these photo-peaks were automatically determined and corrected for background by the software. The full energy peak detection efficiency was then determined from the background corrected counts, the known activity of the source and the implicit in measurement (solid angle).

The experimental and simulated spectra using point sources and volume sources were compared. Both experimental and simulated spectra presented showed a good agreement in terms of shape and varying intensities as expected. Additional photo-peaks were observed from $^{22}$Na, $^{60}$Co, $^{133}$Ba and $^{152}$Eu (point sources) and $^{232}$Th and $^{238}$U (volume sources) experimental spectra these effects were not observed in the simulated spectra. These additional peaks observed are the result of coincidence summing in some of gamma emitting radionuclides.

Efficiencies that were experimentally determined, were compared with the calculated efficiencies from Monte Carlo simulations using MCNPX. Efficiency calibration parameters (power fit function) for the volume sources were determined from experimental and simulated data; a = 2.58; b = -0.75 experimental and a = 1.01; b = 0.65 simulated (100 mL pill bottle) and a = 2.07; b = -0.75 experimental and a = 1.61; b = 0.66 simulated (1 L Marinelli beaker).

The simulated parameters for the efficiency as determined can be used for future calculations of activity concentrations when the 100 mL pill bottle or 1 L Marinelli Beaker sample holder is used. Further improvement in these calculations can be achieved by considering the sample density. The simulation input files used to generate these values is available and can be modified to match any sample holder geometry, as well as any density that might be required in future counting.

# Acknowledgements

"Be thankful in all circumstances, for this is God's will for you who belong to Christ Jesus (1 Thessalonians 5:18)". I would like to thank God Almighty for giving me strength, wisdom and knowledge to work on this thesis.

I am greatly appreciative to my supervisors who made this thesis successful:

- Prof Saalih Allie for always being there for me through the registration processes and taking his time to come at iThemba LABS for the work discussion meetings.
- Dr Peane P. Maleka, for guidance and support and for always availing himself whenever I needed help in simulations, analysis and guidance through this work.
- Dr Ntombizikhona B. Ndlovu for support and guidance and making sure that I had a productive thesis write-up.

I would like to acknowledge the South African Nuclear Human Asset and Research Programme (SANHARP) managed by the National Research Foundation (NRF) for their financial assistance. The NRF-iThemba LABS is also acknowledged for providing the top-up funding and equipment needed to carry out this study. I would also like to thank the University of Cape Town (UCT) Physics Department for their support including contributing toward my fees.

The iThemba LABS Department of Subatomic Physics (DSP) is appreciated for providing the necessary stationery for this study and for providing transport whenever I needed to go to UCT. Most importantly, I would like to thank the former and current managers of the NRF iThemba LABS DSP, Dr R.M. Nchodu and Dr M. Wiedeking, as well as the department secretary, Ms H. Wanana.

I am indebted to my parents and siblings: Andile Bulala, Thembela Bulala, Unathi Mbukwana, Ngawonke Bulala, Mzuvukile Bulala, Uzubenathi Bulala, Sibabalwe Bulala, Sikelela Mbukwana and Limise Mbukwana. I thank you for all the emotional support and encouragement.

I am grateful to my colleagues, friends and others who assisted: Mistura, Sizwe, Pheladi, Sinegugu, Nontobeko, Thuthukile, Sandile, Doris and Sibaliso for their productive inputs to this work, without forgetting all the students at iTL student office for all their inspiration and support; also to Mary Grace McGeehan for her detailed proof reading of the thesis.

# Dedications

I dedicate this work to my parents, Mr Andile Rayner Bulala and Mrs Thembela Gloria Bulala, for their support and unconditional love, and everyone who never forget to pray for me and my studies.

# Table of Contents

# List of figures

# List of tables

# Chapter 1: Introduction

Radiation has been present on Earth since its formation and is part of the environment we live in. Humans are continuously exposed to low levels of ionizing radiation. Radiation sources include water, soil, rocks, power plants, cosmic rays, and medical treatment as well as radiation emissions from natural radionuclides. The ionizing radiation effect depends mainly on the type of radiation, charge, energy and level of radioactivity. Radioactivity is the action of the transformation of unstable atomic nuclei together with the emission of nuclear photons [L'An07]. Radionuclide is an unstable parent nuclide that is transformed into a more stable daughter nuclide in the radioactive decay process [Lil01]. Radionuclides are found naturally in soil, water, air, plants and in our bodies.

## 1.1 Overview

Depending on their origin, radionuclides encountered in the environment can be classified into the following categories: primordial, cosmogenic and anthropogenic [Dem97]. Primordial radionuclides are those that have existed since the creation of Earth. Their half-life times are similar or longer when compared to the age of the Earth [Lil01]. Examples of these primordial radionuclides and their half-lives are listed later in table 2.1. Cosmogenic radionuclides are those that formed because of cosmic radiation interactions with elements in the atmosphere [Sal17]. Cosmic radionuclides such as $^{14}C$, $^{22}Na$ and $^{7}Be$ are formed by rapid bombardment of the stable atoms in the atmosphere and biosphere by cosmic rays originating from outer space [Lil01]. Anthropogenic radionuclides are those that result from human activities, e.g. detonation of nuclear weapons in the environment [Sal17]. Nuclear accidents such as the Chernobyl accident [Kno10; Lil01] and the disaster that occurred at Fukushima in 2011 (which was triggered by an earthquake and tsunami) [Lip13] also results in anthropogenic radionuclides being transmitted to the environment. A more detailed explanation on these radioactive types will be discussed in Chapter 2.

Studying radionuclides via gamma radiation emitted by radioactive sources is one of the primaries means to acquire knowledge about the structure of excited nuclear states [Gil08].

These radionuclides are studied by means of gamma ray detection, which is relatively easy to achieve. Gamma-ray detection can be done with high energy resolution, where transitions which are merely 2 keV apart can be cleanly separated by high resolution (energy) gamma-ray detectors. Gamma-ray detection can also be done with high precision, where uncertainties can be of a few eV in typical cases and more than an order of magnitude better in the best cases [Gil08]. Information about locations and properties of excited states is essential for the evaluation of calculations based on gamma-ray spectroscopy, which is the most precise, direct, and often easiest way to obtain that information.

Gamma-ray detectors typically used for gamma-ray detection are categorized into three groups: namely gas filled, scintillation and semiconductors detectors [Kno10]. Gamma-ray spectroscopy can help to detect gamma-rays associated with decaying radionuclides. However, the effect of coincidence summing has a negative impact in this method when not corrected. Coincidence summing occurs due to a simultaneous detection of two or more gamma-rays, which are emitted within the detection resolving time of electronics [Kno90]. Coincidence summing reduces the number of counts from the photo peak (summing-out) and increases the counts in the continuum. It may also increase the number of counts (summing-in) of some peaks whose energy corresponds to the sum of the lower energy peaks [Kno90].

One way to overcome the effect of coincidence summing in gamma-ray detection experiments, is by means of Monte Carlo (MC) methods. Nowadays, MC simulations are useful for solving problems concerning radiation transport. These methods are powerful and flexible, as they can be applied to various types of radiation detectors [Fad15]. MC methods help to achieve a complete description of the attenuation process, which would include the directional and energy distributions of the outgoing electron and photons [Deb88]. Based on its physical interactions, each photon (either primary or secondary) is tracked from its formation until the end of the interaction process during MC calculations. A photon is created randomly by selecting its energy, the starting location and the initial direction [Mal10].

## 1.2 Motivation for this study

Environmental samples were collected and counted using the Environmental Radioactivity Laboratory (ERL) facility of iThemba LABS to determine the levels of radionuclides present in each sample. The method of choice used in these analyses is the gamma-ray spectroscopy. The goal of gamma-ray spectroscopy method deployed is to accurately determine the activity concentration of each radionuclide present. To determine activity concentrations of these radionuclides in the samples, the following expression is used

$A_c = \frac{Counts}{m* \ \varepsilon * B_r * t}$, where

> $A_c$ is the activity concentration (in Bq.kg$^{-1}$) per radionuclide present in the sample, *Counts* are net counts in photo peak after background subtraction, $\varepsilon$ is the detection efficiency of the detector as a function of gamma-ray energy, $m$ is mass of the sample in kilograms, $B_r$ is the gamma-ray emission probability branching ratio (i.e. the percentage of the decay of the nuclide that will proceed via the emission of a particular gamma-ray), and $t$ is the live time of the data acquisition system.

Each parameter in the expression above can be determined in various ways. For example, *t* (live time) is recorded directly from the software program that runs the code, whereas *m* is directly measured, and *Br* is taken from tabulated isotope information [Fir96]. The other two parameters, activity concentration ($A_c$) and efficiency ($\varepsilon$), cannot be determined directly. The efficiency is a property of the detector, influenced by the gamma-ray energy, sample density, sample geometry relative to the detector crystal and the branching ratio.

This study was undertaken to optimise the efficiency of the detector as a function of energy for various sample geometries. It will also be useful and relevant to future experiments that might arise, involving efficiency matters. To overcome and minimise the use of radiation sources, MC calculations are used to determine the photo-peak efficiency of the detector used. This approach is however limited in its accuracy due to the uncertainties in the parameters associated with the detector's geometrical dimensions and the material composition of the sample.

## 1.3 Aim and Objectives of this study

This study aims to use Monte Carlo simulations code, MCNPX version 274a, to benchmark parameters of the iThemba LABS ERL gamma-ray detector. This is done to determine the efficiency of the detector for various sample counting geometries as well as to optimise the parameters using certified point sources. The objectives of this study to achieve the above-mentioned aim are as follows:

- To use the available gamma-ray detector to count samples with known activity concentrations in various counting geometries (Marinelli beaker and pill bottle) and then determine the detection efficiency parameters (as a function of geometry and gamma-ray energy).
- To use certified reference point sources to optimise the detector parameters used for MC calculations. These point sources will be counted using the available gamma-ray detector and their MC simulations will be performed based on the similar setup.

## 1.4 Outline of this thesis

This thesis contains five chapters. **Chapter 1** consists of the introduction of the study, motivation, aims and objectives, as well as the outline of this study. In **Chapter 2**, there is a review of literature, mainly focusing on the background information as well as discussion of theory that is based on radioactivity and its decay. Interaction of gamma-ray with matter and the MC methods are also discussed in chapter 2. **Chapter 3** describes the radiometric measurements, experimental set-up and the methodology used in this study. MC simulations are presented in **Chapter 4**. In **Chapter 5**, the results and interpretation of data are presented (for both experiments and simulations). Also, in Chapter 5 is the presentation of the, summary and conclusion of the study.

# Chapter 2: Radiometric measurements

In this chapter, background information on radioactive decay processes is discussed. This includes properties and characteristics of radionuclides, as they are important when working with activity concentrations of the environmental samples. This study focuses on measuring γ-rays emitted by primordial (natural) radionuclides (such as; $^{238}$U, $^{232}$Th and $^{40}$K series), as well as anthropogenic (man-made) radionuclides using a gamma-ray detector. In addition, interaction of gamma-rays with matter and MC methods are discussed later in this chapter. Gamma-ray spectrometry (involving the HPGe detector) will be discussed extensively in the next chapter.

## 2.1 Environmental radioactivity

Radioactive materials can be found anywhere on earth, and they can be categorized into three types, namely primordial, cosmic and anthropogenic radionuclides [DeM97]. In the next subsection, these types of environmental radionuclides will be discussed in more details.

### 2.1.1 Primordial radionuclides

Primordial radionuclides are those that have existed since the formation of the Earth. Their half-lives are sufficiently long that they can be comparable to the age of the earth. Primordial radionuclides compose the bulk of the natural radioactivity in the environment, which forms background radiation in the environment. Some of these naturally occurring radioisotopes, such as $^{40}$K, decay directly to a stable daughter isotope. There are three naturally occurring radioactive series which have existed since the formation of Earth, about 4.5 billion years ago [Lil01]. Each naturally occurring radioactive series is headed by a very long-lived parent radionuclide, which can either be $^{238}$U, $^{235}$U or $^{232}$Th. Each parent radionuclide controls the decay of the radioactive daughters, which all have relatively much shorter half-lives [Lil01]. Table 2.1 presents only the primordial radionuclides that are of interest for this study.

**Table 2. 1:** List of primordial radionuclides [Fir96].

| Nuclide | Decay Mode | Half-life (years) | Isotopic abundance (%) |
|---|---|---|---|
| $^{232}$Th | $\alpha, \beta, \gamma$ | $(1.405 \pm 0.006) \times 10^{10}$ | 100 |
| $^{238}$U | $\alpha, \beta$ | $(4.468 \pm 0.003) \times 10^{9}$ | 99.3 |
| $^{40}$K | $\beta, \varepsilon, \gamma$ | $(1.277 \pm 0.008) \times 10^{9}$ | 0.0117 |

The radionuclides in each chain (decay series) decay by emitting α- and/or β-particles or sometimes γ-rays, until a final or stable nuclide is reached. Figures 2.1 and 2.2, show the decay chain of $^{232}$Th and $^{238}$U, respectively. In these figures, grey boxes represent the gamma-ray emitting nuclides. The decay process of $^{40}$K is also presented in Figure 2.3.

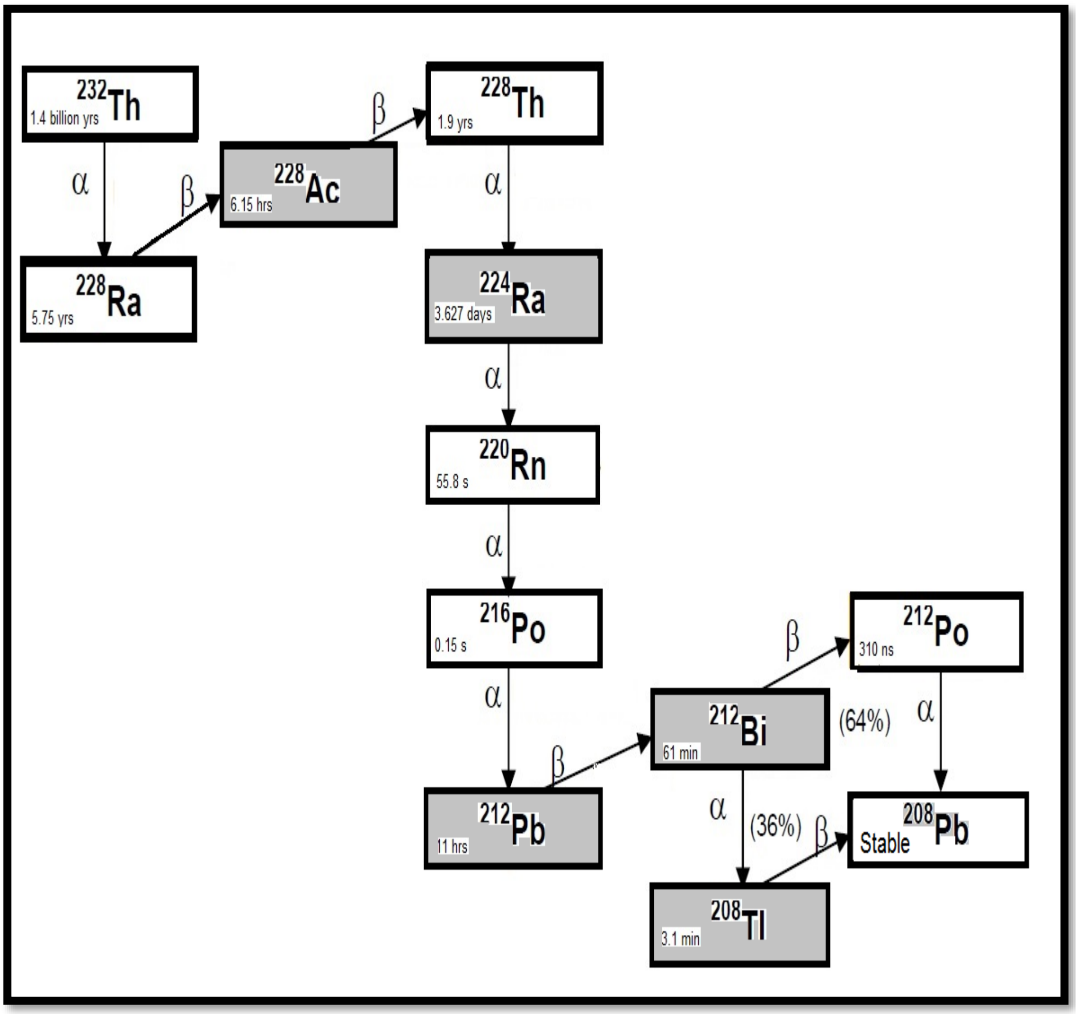

**Figure 2. 1:** Schematic diagram showing $^{232}$Th decay series [Gil08].

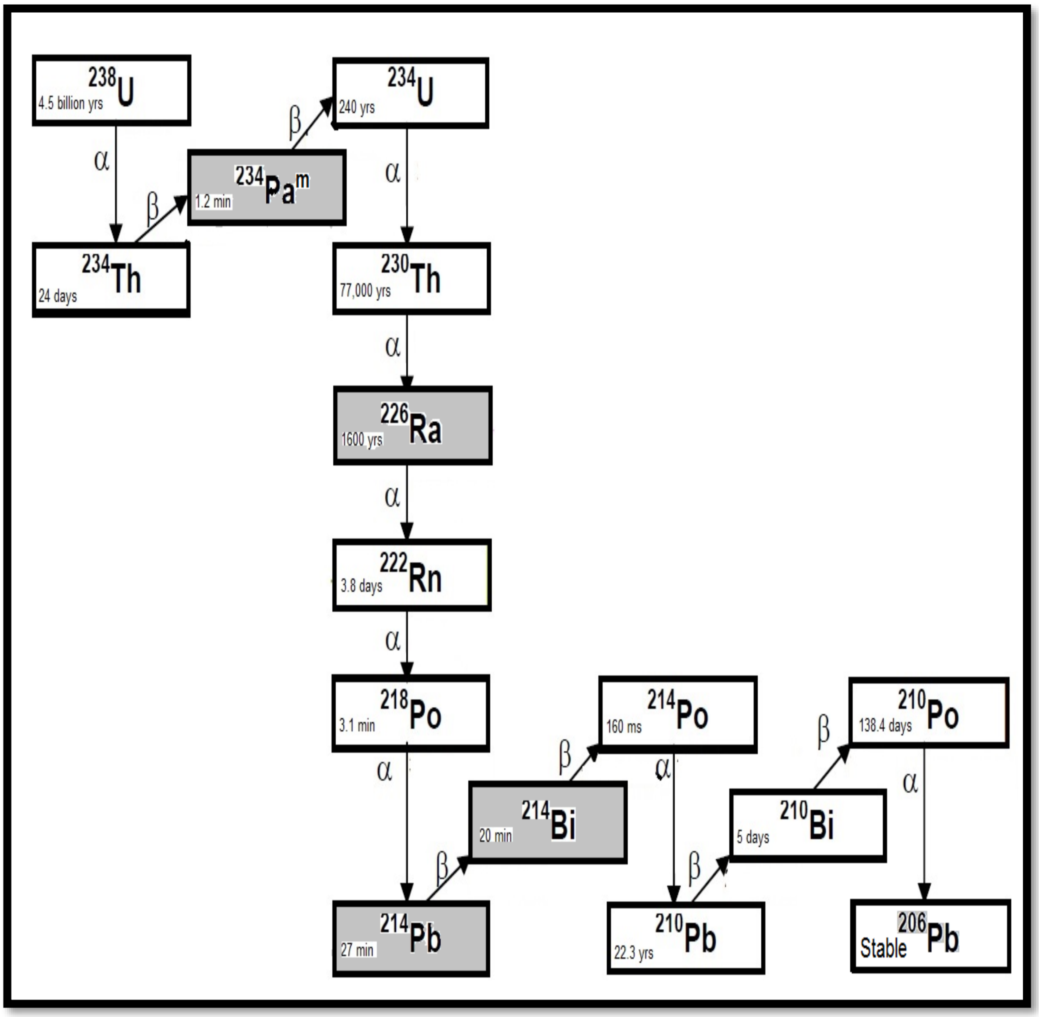

**Figure 2. 2:** Schematic diagram showing $^{238}$U decay series [Gil08].

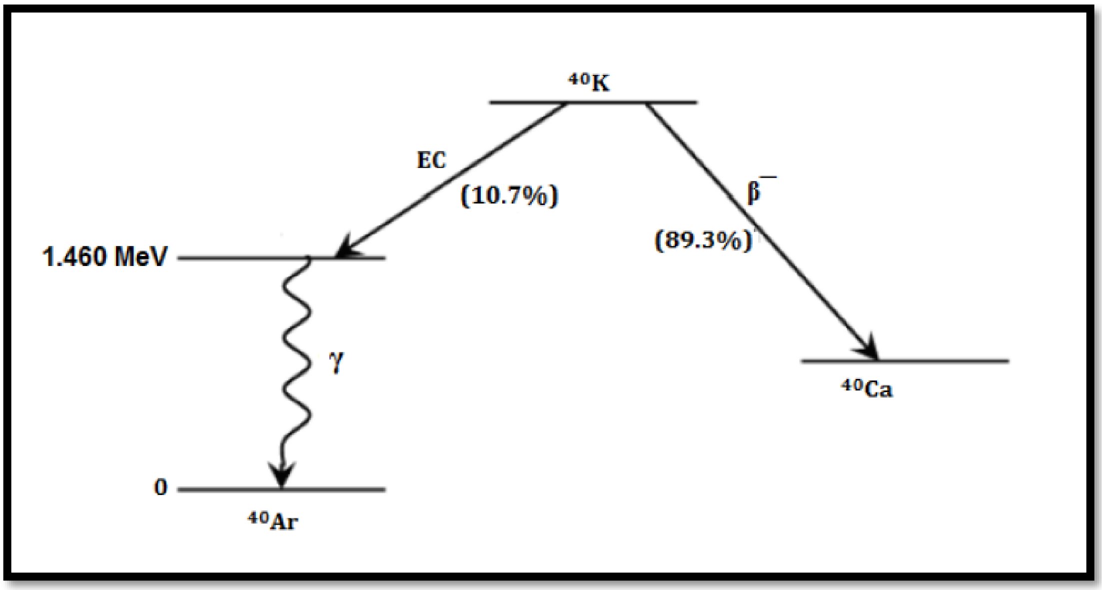

**Figure 2. 3:** Schematic diagram showing the $^{40}$K decay process [Fir96].

### 2.1.2 Cosmogenic Radionuclides

Primary cosmic rays are extremely energetic charged particles, usually protons and $\alpha$-particles, which are released onto the Earth from outer space [Lil01]. Cosmogenic radionuclides are formed because of the interaction of these cosmic rays with matter around the Earth and in the atmosphere. This interaction happens in the upper atmosphere and produce showers of gamma-rays and electrons, a fraction of which penetrates to the Earth's surface [Kno10; Lil01]. A huge number of cosmic rays produced by radioactive isotopes can be found all over the Earth. The atmosphere acts as a shield that reduces the intensity of cosmic radiation that reaches the Earth's surface. Cosmogenic radionuclides can be found to have long half-lives. However, most of them have shorter half-lives as compared to the primordial radionuclides. For examples, carbon-14 ($^{14}$C) has a half-life of 5730 years, while tritium-3 ($^{3}$H) has a half-life of 12.33 years [L'An07]. In addition, $^{10}$Be radionuclide is established among other isotopes of the light elements in cosmic rays with the half-life of 1.6 $\times 10^6$ years [Lil01].

### 2.1.3 Anthropogenic Radionuclides

Anthropogenic radionuclides are radionuclides formed because of human actions. Humans have built many devices that produce radiation, e.g. nuclear power stations and nuclear reactors. Radionuclides from these devices are carried into the atmosphere, where they remain for some time and later get dispersed and deposited around the world [Tyk95]. Major sources of anthropogenic radiation are radionuclides introduced into the environment by the testing of nuclear weapons and routine operations of nuclear installations during nuclear accidents. Some of these anthropogenic radionuclides include $^{90}$Sr, $^{99}$Tc, $^{129}$I, $^{131}$I, $^{137}$Cs, $^{239}$Pu and several other isotopes of plutonium [Lil01].

## 2.2 Radioactive decay

A radioactive source is defined based on the number of nuclei decaying per unit time. The activity of a specific radionuclide in a sample corresponds to the number of radioactive atoms available in that sample. As a result, the activity of a radionuclide is also a measure of its mass. The activity reduces with time because of radioactive decay. The half-life of the radionuclide may be very short (seconds or minutes) or very long (on the order of many years). The decay rates of some radionuclides may be so low that it is unfeasible to measure any change in radioactivity throughout their lifetime [L'An07]. The three primary types of radiation emitted by radioactive matters are alpha ($\alpha$)-particles, beta ($\beta$)-particles, and gamma ($\gamma$)-rays [Kra88].

**Alpha-particles** are $^4$He nuclei (like a bound system of two neutrons and two protons) and are generally emitted by heavy nuclei carrying too many nucleons to remain stable. Most naturally occurring heavy nuclei (with $82 < Z \leq 92$) (refer also Figures 2.1 and 2.2) and artificially produced transuranic elements (with $Z > 92$) decay by $\alpha$ emission, in which the parent nucleus loses both mass and charge. Hence $Z, A \rightarrow Z\text{-}2, A\text{-}4 + \alpha$ [Leo87; Lil01].

**Beta-particles** are described as fast positrons or electrons which result from a weak-interaction decay of a proton or a neutron in nuclei which carry an excess of the respective nucleon. In a neutron-rich nucleus, a neutron (n) can transform itself into a proton (p) via the $\beta^-$ process:

$$n \rightarrow p + e^{-} + \bar{v} \qquad (2.1)$$

where an electron ($e^{-}$) and antineutrino ($\bar{v}$) are emitted. In that case, the daughter nucleus left with one extra proton so that its atomic number is increased by 1 (refer also to Figure 2.3 whereby $^{40}$K decay to $^{40}$Ca). Similarly, in nuclei with too many protons, the $\beta^{+}$ decay can occur, whereby a positron ($e^{+}$) and a neutrino ($v$) are now emitted and the atomic number is decreased by 1.

$$p \rightarrow n + e^{+} + v \qquad (2.2)$$

The transitions between energy levels can be made by the emission or absorption of electromagnetic radiation of the correct energy. The energies of these photons, from a several keV to a several MeV, characterize the high binding energy of nuclei. These high energy photons were historically named gamma-rays, and like atoms, they show spectral lines characteristic of the emitting nucleus [Leo87]. A nuclide in an excited energy state is called a nuclear isomer, while the transition from a higher to a lower energy state is called an isomeric transition [L'An07]. Most gamma-ray sources are set in their excited states because of an $\beta$-disintegration, although excited nuclear states are also frequently formed in nuclear reactions. Since positrons and electrons are more easily absorbed in matter, $\beta$-particles in such sources can be filtered out by enveloping them with enough absorbing material and leaving only the more penetrating gamma-ray [Leo87].

Most nuclei are unstable, and they decay by spontaneously emitting a particle, thus producing another nucleus, which is known as a daughter nucleus, while the initial nucleus is often called the parent nucleus. The radioactive decay process can be described statistically. The statistical nature of the decay process is described by the radioactive decay law. It states that, if a sample contains *N* number of nuclei, the rate at which the nuclei decays (- $\frac{\mathrm{d}N}{\mathrm{d}t}$) is proportional to *N*. The negative sign shows that the number of nuclei decreases with time [Mic98].

Thus,

$$-\frac{dN}{dt} = \lambda N \qquad (2.3)$$

where $\lambda$ is the disintegration or decay constant, a characteristic of the nucleus concerned. Equation (2.3) can also be written as $\frac{dN}{N} = -\lambda dt$ . If the initial nuclei are $N_0$ at $t$ = 0, then integration of equation 2.3 gives

$$\int_{No}^{N} \frac{dN}{N} = -\int_{0}^{t} \lambda dt \qquad (2.4)$$

$$ln\ N - ln\ N_0 = -\ \lambda t$$

$$\Rightarrow N = N_0 e^{-\lambda t} \qquad (2.5)$$

## 2.2.1 Half - life

The transition of radioactive atoms is a gradual process. Unstable atoms do not all undergo transitions at the same time, they undergo transitions in a random manner. Each radionuclide undergoes a transition at a characteristic average rate so that the rate at which the number of radionuclides in a given sample decreases is not the same for all radionuclides. In the end, radionuclides undergo transitions to stable final products. Appropriately, the number of radioactive atoms will decrease with time [Van15]. Rates of radionuclides' decay are usually expressed in terms of half-life. Half-life, represented by symbol $t_{1/2,}$ is defined as the time ($t$) required for a given amount of radionuclide to lose 50% (half) of its intensity [L'An07]. The half-life of a radionuclide is a measure of the rate at which the nuclide undergoes radioactive transition. Every radionuclide has its own unique half-life, which is independent of its physical state. Half-lives of radionuclides range from nanoseconds to billions of years [Van15]. From equation 2.5, an exponential decrease in activity of a radioactive source is therefore governed by the decay constant. In practice, it is more habitual to use the inverse of $\lambda$,

$$\tau_m = {}^{1}/_{\lambda} \qquad (2.6)$$

which is known as the mean lifetime. This is the time it takes for a sample to decay to 1/e of its original activity. Equally in use is the half-life, $t_{1/2}$, which is known as the time it takes for the sample to decay to one half of its original activity [Leo87]. Thus,

$$N = N_o e^{-\lambda t} \text{ then,}$$

$$\frac{N_o}{2} = N_o e^{-\lambda t_{1/2}}$$

$$ln\left(\frac{1}{2}\right) = -\lambda t_{1/2}$$

$$t_{1/_2} = {}^{0.693}/_{\lambda} \tag{2.7}$$

Radioactive transition is a random process which follows a characteristic exponential curve, as shown in Figure 2.4. This is an example of exponential radioactive decay curve of $^{228}$Ac with a half-life of 6.15 hours [San12].

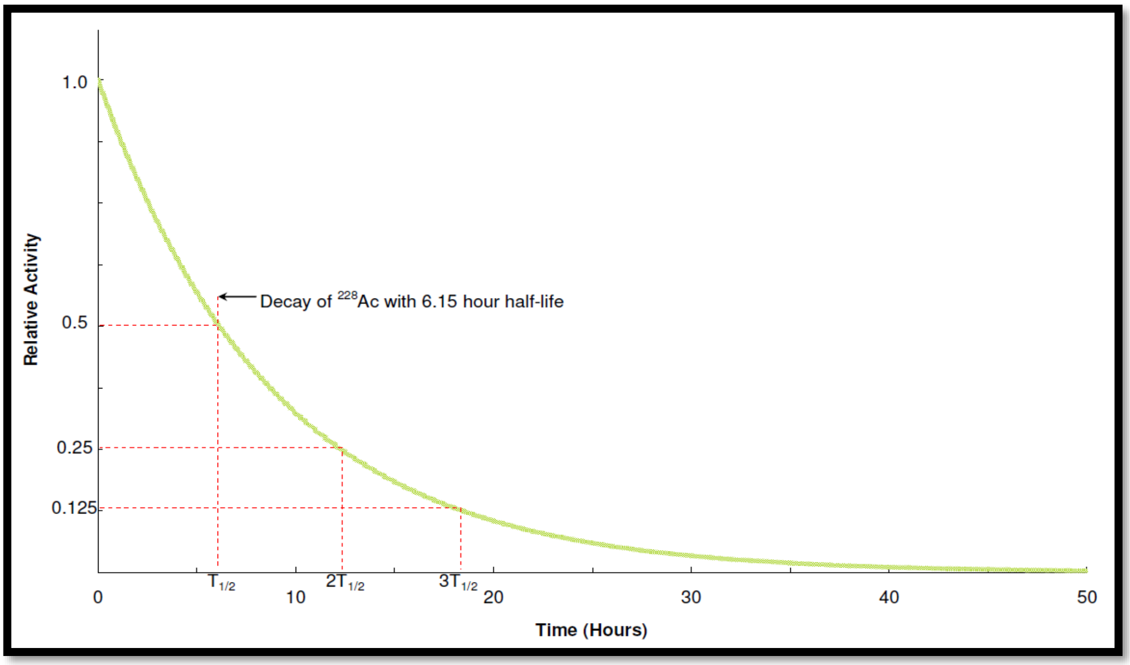

**Figure 2. 4:** The exponential radioactive decay curve of the $^{228}$Ac [San12].

## 2.3 Gamma-ray properties and interactions

Interpretation of the features of a measured gamma-ray spectrum needs a clear understanding of the interaction of gamma-rays with matter. The interaction of gamma-rays with matter plays a major role in gamma radiation measurements. These gamma-rays are electromagnetic waves produced spontaneously by radioactive elements. They are most efficiently detected by high atomic number (Z) materials. These radioactive particles are penetrative and have longer range in matter than other radioactive particles such as alpha and beta particles. However, gamma-rays can also be absorbed by matter. There are three dominant primary processes that are important when gamma-rays interact with matter

[Deb88; Kno00]. These processes are photoelectric absorption, Compton scattering and pair production.

## 2.3.1 Photoelectric Absorption

In the process of photoelectric absorption, interaction is between a photon and a bound atomic electron. Then an energetic free electron known as photoelectron is ejected from one of the electron shells, while the photon disappears [Tso83]. The electron energy ($\mathrm{E}_e$) is approximately equal to

$$\mathrm{E}_e = \mathrm{E}_\gamma - \mathrm{E}_b \tag{2.8}$$

where $\mathrm{E}_\gamma$ is an incident photon energy and $\mathrm{E}_b$ is the binding energy. Usually, the emission of a photoelectron is likely to originate from the K–shell of the atom. The binding energy of K-shell electrons is 11.1 keV for Germanium (Ge) and 1.84 keV for Silicon (Si). This binding energy varies from a few keV (for low Z materials) to tens of keV (for materials with higher atomic number) [Kno10; Deb88]. In Figure 2.5, a schematic diagram of photoelectric absorption process is presented. Photoelectric absorption cannot occur with an unbound electron since it would not be possible to conserve both momentum and energy. The ejected electron will be reduced in a nearby material and its energy will be absorbed there. This will leave a hole in a shell of the atom, and this atom will de-excite with the emission of one or more X-rays. In the case whereby an interaction takes place in bulk matter, these X-rays will also be absorbed in the surrounding matter. Therefore, in most cases, this interaction involves the transfer of all the photon energy to the matter near the interaction site [Deb88].

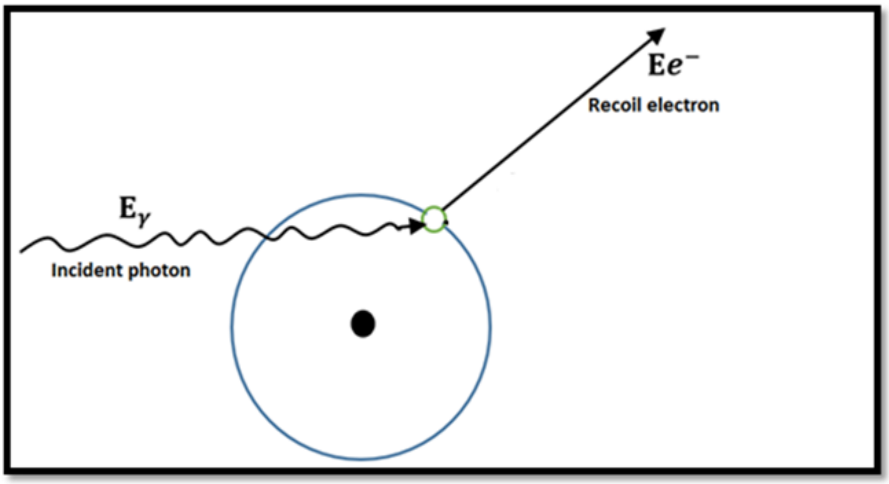

**Figure 2. 5:** Schematic diagram showing the mechanism of photoelectric absorption [Gil08].

Photoelectric absorption is a predominant mode of interaction for gamma-rays of low energies. This process is also enhanced for absorber materials of higher atomic number (Z). The probability of the photoelectric absorption per atom is approximated by the expression;

$$\tau \cong Const.\times \frac{Z^n}{E_\gamma^3} \tag{2.9}$$

Where *n* varies between 4 and 5 over the gamma-ray energy region of interest [Kno00]. The probability for photoelectric absorption increases as the atomic number Z increases, while decreasing fast with increasing gamma-ray energy and becoming smaller after the absorption edge. The probability is higher for more tightly bound electrons such as the electron in the K-shell.

### 2.3.2 Compton Scattering

Compton scattering is a collision between an incident gamma photon and an electron in the absorber. Unlike the photoelectric effect, only a portion of the photon energy is transferred to an electron. The other remaining photon energy appears as a secondary photon [Gil08; Deb88].

The schematic diagram in Figure 2.6 represents the Compton scattering process. During this process, an incident gamma ray photon having an energy, $\mathrm{E}_\gamma$, is deflected by an atomic electron, resulting in a scattered photon of energy. $E'_\gamma$ at an angle θ. Moreover, an electron is deflected at an angle $\phi$ to the trajectory of the incident gamma-ray photon $E_\gamma$.

The energy imparted to the recoil electron is given by

$$E_e = E_\gamma - E'_\gamma \tag{2.10}$$

An equation that is used to calculate the energy of a deflected photon is given by

$$E'_\gamma = \frac{E_\gamma}{1+E_\gamma/m_o c^2\,(1-cos\theta)} \tag{2.11}$$

where $m_0c^2$ is the rest mass energy of the electron equal to 0.511 MeV. The maximum energy transfer to the electron occurs for a scattering angle of θ = 0° which leads to $E'_\gamma = E_\gamma$ [L'An07; Lil01].

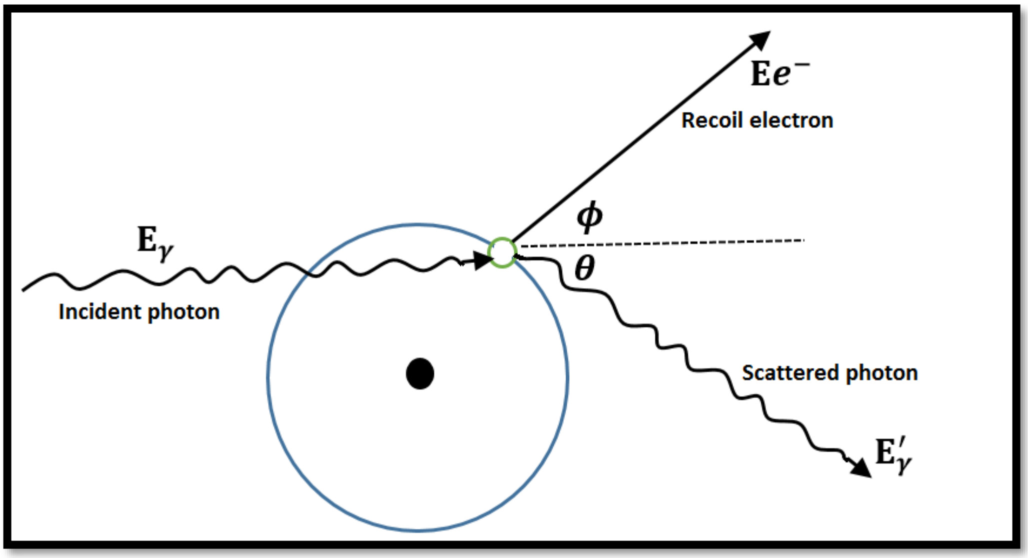

**Figure 2. 6:** Schematic diagram showing the mechanism of Compton scattering [Gil08].

The probability for Compton scattering process to occur largely depends on the energy of the gamma-ray and atomic number, Z, of the detector material. For instance, a gamma-ray can backscatter at ϕ = 180° conveying maximum energy to the electron; as a result, a Compton edge is produced in the gamma-ray spectrum. The probability of Compton scattering process per atom of the absorber depends on the number of electrons available as scattering targets, and consequently increases linearly with Z [Kno00].

### 2.3.3 Pair production

In the pair production process, there is a transformation of a photon into an electron and a positron. Pair production occurs near nuclei of the absorbing material because of the high electric field at this point. The incident $\gamma$-ray photon disappears, and an electron-positron pair is produced in its place. An energy equivalent to $2m_0c^2$ ($2 \times 0.511$ MeV) is required to create an electron-positron pair and hence a photon should have a minimum gamma ray energy of 1.022 MeV for pair production to occur. Any surplus energy is transferred into kinetic energy which is shared by the electron-positron pair. The total kinetic energy of the electron positron pair is given by

$$E_{e^-} + E_{e^+} = \mathrm{E}_\gamma - 2\,m_0c^2 \tag{2.12}$$

A schematic diagram in figure 2.7 shows the pair production process in a simplified form. In principle, an electron and a positron typically travel a few millimetres in the material before losing their energy in the absorbing medium.  A positron slows down due to collisions with electrons in the medium and as result can interact with another electron from the absorbing medium. This is introduced by an annihilation of both particles, which are replaced by two annihilation photons (each of energy 0.511 MeV energy), which are emitted back-to-back to conserve linear momentum [Kno00; Leo87]. On condition that the detector absorbs both annihilation gamma-rays, their interaction donates to the full-energy peak in the gamma-ray measured spectrum. Nevertheless, if one gamma-ray of the annihilation depart from the detector, the interaction donates to the single-escape peak at 0.511 MeV below the full-energy peak. Furthermore, on condition that both gamma rays escape, the interaction donates to the double-escape peak which is at 1.022 MeV below the full-energy peak [Par03].

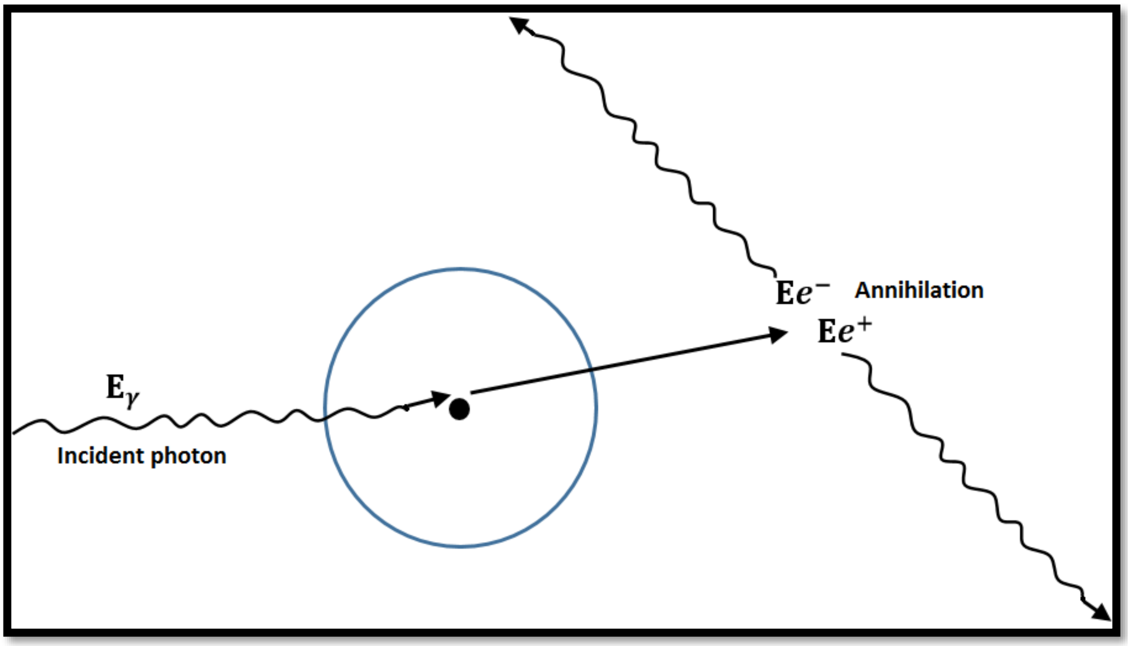

**Figure 2. 7:** Schematic diagram showing the mechanism of pair production [Gil08].

### 2.3.4 Attenuation coefficient

As a photon moves through matter, it is impossible to precisely know what type of interaction it will be involved in. Either photoelectric, Compton or pair production interactions will occur, thus absorption of some of the photons from the beam of particles. This process is known as attenuation [Kno00]. Suppose $N_0$ photons are moving through a slab of material at some distance, x, into the material. Then after exiting the material the number of photons in the beam is reduced. Equation 2.13 shows how the number of photons is reduced;

$$N_x = N_{0e^{-\mu x}} \tag{2.13}$$

Where μ is known as the linear attenuation coefficient and is the actual fraction of photons interaction per unit thickness of the material. The exponential decay in equation 2.13 comes from the reality that over a short distance, the probability of losing a particle from the beam is proportional to the number of particles left [Kno00].

## 2.4 Gamma-ray detection

Incident radiation interacts with atoms in the detector material by ionization or excitation, and results in the emission of many relatively low-energy electrons from their atomic orbits [Kra88]. Detectors used for gamma-ray detection can be classified into three categories, namely gas ionisation, semiconductors and scintillation detectors. The most widely used are the scintillation and semiconductor detectors. There are two types of scintillation material, organic and inorganic. The gamma-ray detectors are made of either gas, solid or liquid materials [Kno10; Lil01].

### 2.4.1 Semiconductor detectors

The type of detector used in this study is a semiconductor detector. A semiconductor is the material that can act as an insulator or a conductor. Silicon (Si) and Germanium (Ge) are the most widely used semiconductors. Semiconductors are referred to as solid-state detectors. Moreover, scintillation counters can also be described as solid-state detectors. The important advantage of semiconductors, as compared to other types of radiation counters, is their superior energy resolution [Kno10].

### 2.4.2 High Purity Germanium (HPGe) detector

Currently Ge (Germanium) detectors are widely exploited in high resolution gamma-ray spectroscopy experiments. This is due to their excellent energy resolution that gives them the best ability of identifying and differentiating any gamma-ray emitting isotopes. However, Ge detectors exist in a relatively low-energy needed to create an electron-hole (e-h) pair, which is about 3 eV at 77 K [Tyk95]. Much greater operational convenience is afforded by high-purity Ge (HPGe) detectors that became available in the early 1980s. Due to its much lower net impurity concentration as compared to ordinary Ge, HPGe provides an alternative of creating an intrinsic region in a Ge crystal. Detectors made from ultrapure Ge material are generally known as intrinsic or HPGe detectors [Deb88; Kno90].

## 2.5 Coincidence summing

Coincidence summing refers to the summing of two gamma-rays, or an X-ray and a gamma-ray emitted in coincidence. As with random summing, this event results in a summing in from gamma-ray full-energy peaks and a loss of efficiency [Gil08]. Hence, for measuring low-level environmental samples, the counting time is reduced by increasing the detection efficiency of the detector [Ram97]. More significantly, coincidence summing effects can also appear in the detector efficiency measurements. This is because efficiency measurements are carried out under the same measuring conditions as for the activity concentration determination [Ram97]. The probability of coincidence summing is related to nuclear decay scheme, transitions, and the detector full-energy peaks [Geh05]. Coincidence summing is geometrical dependent [Gil08]. It greatly depends on the geometry of sample and the detector. The reduction of the coincidence summing effect can be accomplished by increasing the source to detector distance [Geh05].

An example of $^{152}$Eu simplified decay scheme analysed by Gilmore [Gil08] states that atoms of $^{152}$Eu have a choice when they decay. The nuclide can emit a $\beta^-$ particle and become $^{152}$Gd or, on 72.08 % of occasions, experience electron captures and become $^{152}$Sm. In this decay scheme, every electron captures that decays to $^{152}$Sm is likely to be led by the emission of Sm X-rays [Gil08]. The daughter nucleus, resulting from any mode of decay in that moment, de-excites by emitting several gamma-rays. Figure 2.8 shows a decay scheme, whereby $^{152}$Eu decays by electron capture to $^{152}$Sm, which further decays by releasing cascades of gamma-rays. The 121.8 keV gamma-ray and the 1408.0 keV gamma-ray may produce on the gamma-ray spectrum what seems to be 1529.8 keV gamma-ray.

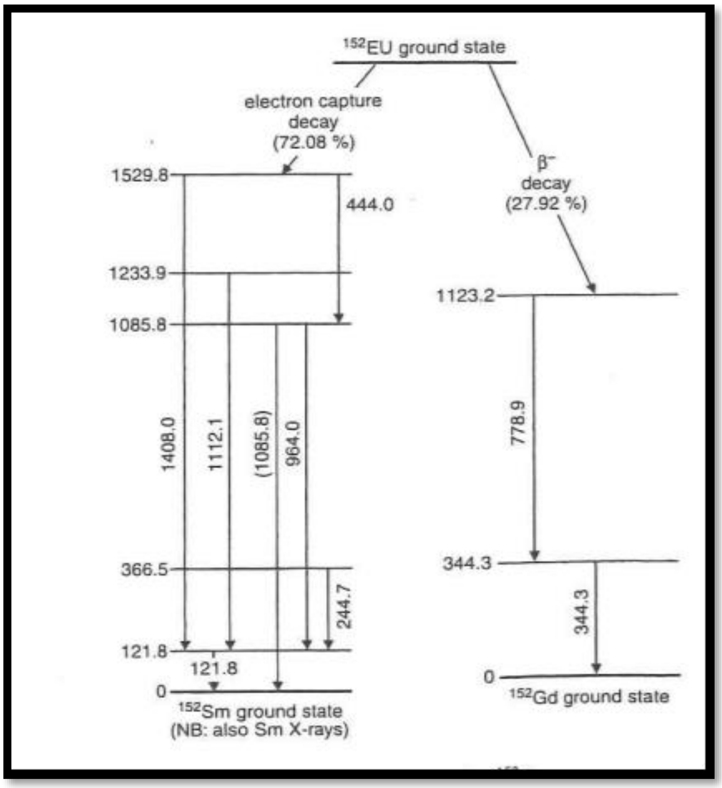

**Figure 2. 8:** Decay scheme for the $^{152}$Eu [Gil08]

## 2.6 Detection efficiency

Detection efficiency can be defined in many ways depending on how it is used. Since efficiency used in gamma-ray spectrometry can be defined in multiple ways, Table 2.2 provides a brief information on how efficiency can be defined.

Detection efficiency depends on various factors such as gamma-ray energy, sample and composition density and sample geometry (e.g. Marinelli beaker, pill bottle, point source, etc.). There is a method used by Quintana and Fernández [Qui96] from results of performed research. These days, their method can be applied to various experimental set-ups, which can be for both solid and liquid environmental samples [Daz01]. As an input, the method requires two different types of experimental measurements. The first type needs measurements with radioactive sources emitting cascades of gamma-rays which are covering the energy range of interest. The second type needs measurements with sources emitting isolated gamma-rays, to provide coincidence summing corrections [Daz01; Qui96].

**Table 2. 2:** Types of efficiency and their simplified meaning. The type of efficiency mostly used in this study is the one presented in bold [Gil95].

| **Types of efficiency** | **Definition** |
|---|---|
| Relative efficiency | The general performance measure of relating the efficiency of detecting of a $^{60}$Co gamma-ray at 1332 keV of the semiconductor detector to that of a NaI (Tl) 3"x 3" detector. |
| Intrinsic efficiency | A basic parameter of the detector and is independent of the source or detector geometry. It relates the counts in the spectrum to the number of incidents on the detector. |
| **Full energy peak efficiency** | **It relates the peak area at an energy, to the number of gamma-rays emitted by the radioactive source. It is dependent on the geometrical alignment of source composition (matrix effects resulting in self-absorption) and detector.** |
| Absolute total efficiency | It relates the number of gamma-rays emitted by the source to the number of counts detected wherever in the spectrum. It also includes the full-energy peak and all incomplete absorptions represented by Compton continuum. |

The establishment of this method is a general function to describe the energy dependence of efficiency for a geometry and source matrix. This method was used in 11 experimental arrangements to provide efficiency calibrations over 46.54 – 2000 keV energy range, with corresponding uncertainties ranging from 0.1% to 1.8%. The experimental arrangements accommodated high precision measurements with sources which generally have very low activities [Daz01].

The use of extended sources in gamma-ray spectrometry significantly improves the sensitivity of detection, hence enabling the measurement of low-activity samples. To achieve reliable measurements of radionuclides activity, information about the detector's absolute full energy peak efficiency in counting is needed. This is a challenge whenever there are many types of geometries and matrices involved in the measurements. The detector count rate depends on the characteristics of the geometry, matrix and detector configuration [Daz01; Deb88].

Another alternative for reducing the number of sources required in the experiment is to make use of radionuclides emitting several gamma-rays that account for the energy range of interest. Nevertheless, this gives rise to a new problem since these gamma-rays are usually emitted in cascade. In turn this introduces coincidence-summing effects in the measurements, causing it necessary to correct the experimental efficiencies acquired. Therefore, in measuring geometries where sources are placed on the detector window, coincidence summing effect must be considered. This means that the coincidence-summing corrections must be determined for each configuration due to their dependence on the counting conditions. Usually, these correction factors are acquired through a combination of numerical and theoretical calculations, which need approximations to consider extended sources and the complex decay schemes [Daz01].

An economical alternative to using radioactive sources is the computation of efficiency values using Monte Carlo (MC) simulations. However, inadequate knowledge about detector characteristics and matrix composition significantly increases the error on the low energy efficiency values. Methods based on MC simulations provide accurate results to within 3 % uncertainty, rising to more than 5 % at energies below 100 keV for complex matrices and extended sources [Daz01]. MC methods have been commonly used in the computation of the full energy peak efficiency (FEPE) calibration of HPGe detectors in vivo whole-body counting virtual calibration [Liy06]. In most cases the MC efficiency transfer method is used to determine full energy peak efficiency of two types of HPGe detectors, a coaxial n-type and a coaxial p-type [Liy06]. There exist two different ways for MC calculations of FEPE. The first is the direct MC calculation method that consists of calculating the FEPE directly by MC simulation, while the second is the MC efficiency transfer method consisting of calculating the FEPE by means of an energy dependent transfer factor [Var03; Liy06].

# Chapter 3: Experimental setup

Experimental setup for this study includes the ERL Hyper Pure Germanium (HPGe) detector as well as its properties, electronics and detector shielding. Experimental setup used to conduct this study and data analysis of the experiment will be discussed in this chapter. This will include samples and geometries used for measurements, as well as the experimental data analysis, energy and efficiency calibrations.

## 3.1 The ERL HPGe detector system

At the ERL facility, iThemba LABS, gamma-ray measurements are conducted using a low-background HPGe detector system. The available HPGe detector is a Canberra GC4520 *p*-type model, crystal diameter of 6.25 and 5.95 cm length and a built-in pre-amplifier (model 2002 CSL) [Can99]. The detector setup is encased in a 10 cm thick lead castle to reduce room background. The lead castle also has a 2 mm thick copper lining inside to absorb X-rays emanating from the lead. At 1.33 MeV, the detector has a 45 % relative efficiency and a Full Width at Half Maximum (FWHM) of 2.0 keV [Can99]. During the manufacturing of HPGe detectors, Canberra measures the number of counts in the 1332.5 keV peak of $^{60}$Co. Then, at half the photo-peak counts the width of 1332.5 keV peak or FWHM resolution is found. The Ge dead layer has the dimension of 0.5 mm [Dam05].

The HPGe detector crystal is upward facing and mounted in a vertical dipstick liquid nitrogen ($LN_2$) cryostat, which contains a detector vacuum chamber with a dipstick-like cold finger. This dipstick-like cold finger is inserted into the neck of the Dewar (double walled vacuum-insulated vessel). A cryostat consists of a vacuum chamber that houses the detector element plus a Dewar for ($LN_2$) cryogen. The ($LN_2$) causes any moisture in the system to freeze. This process helps to maintain the vacuum and is termed cryogenic pumping. The detector Dewar of the iThemba LABS is filled weekly with ($LN_2$), to keep the detector operating at liquid nitrogen temperatures. Figures 3.1 to 3.3 shows photographs of the ERL HPGe detection setup, showing the lead castle (for shielding), the Dewar ($LN_2$- storage tank), HPGe cross sectional view and a sketch of iThemba LABS experimental setup.

**Figure 3. 1:** A photograph of ERL HPGe detection setup and the view from the top with the lead-castle open revealing the front view of detector.

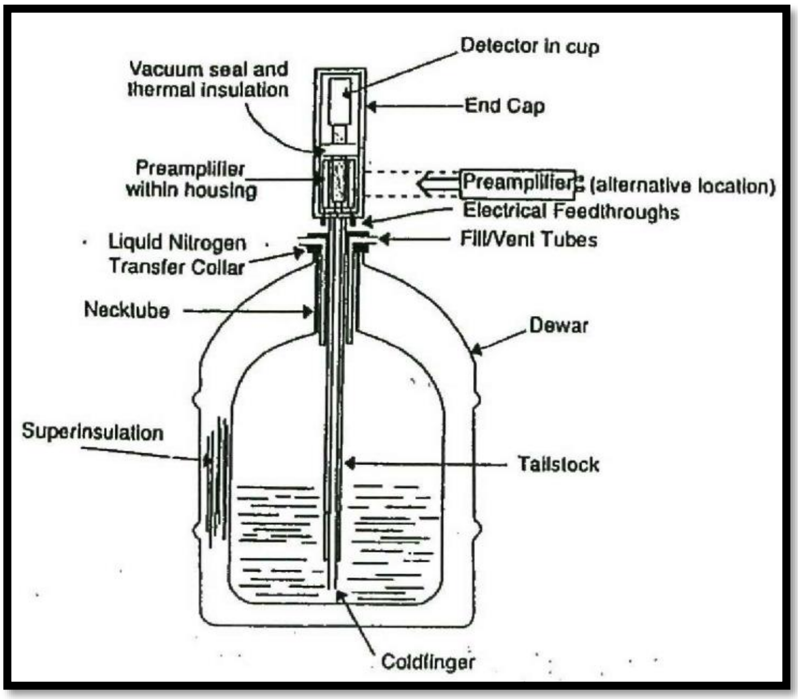

**Figure 3. 2:** Cross section diagram of the HPGe detector with liquid nitrogen Dewar [Gil08].

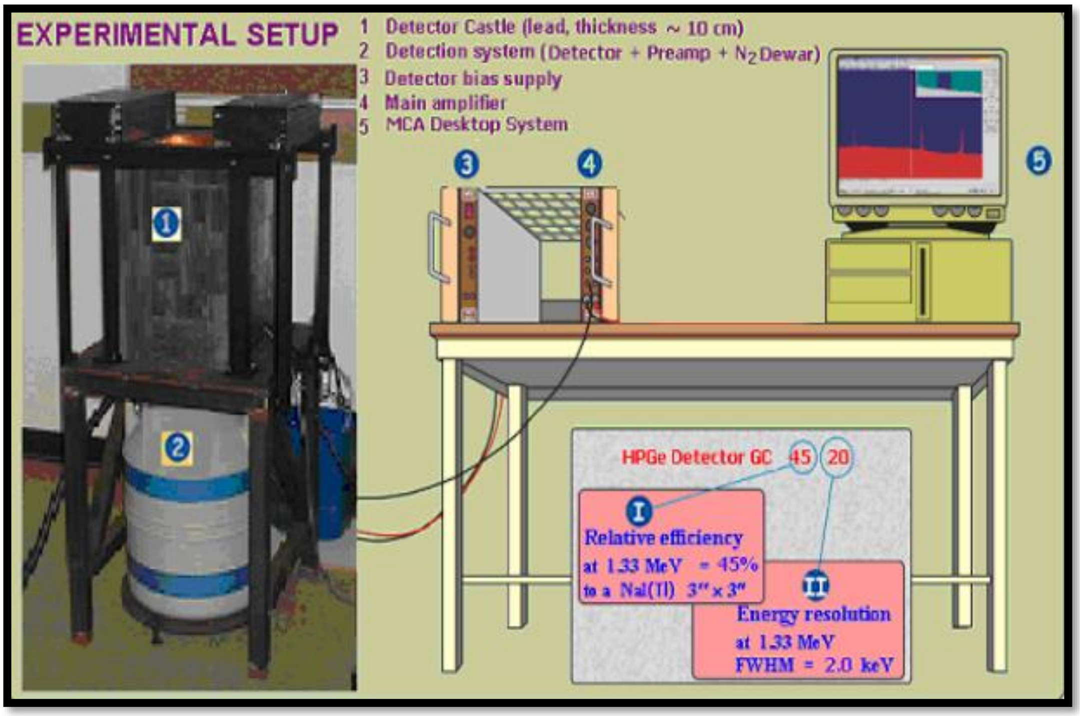

**Figure 3. 3:** Experimental setup of the HPGe gamma-ray spectrometry system [Dam05].

## 3.2 HPGe detector properties: Electronics and shielding

Illustrated in Figure 3.4 is the setup of the electronics of the semiconductor spectrometer available at the iThemba LABS ERL facility. The system consists of a detector bias supply (SILENA model 7716), preamplifier (model 2002 CSL), amplifier (model ORTEC 572), and multi-channel analyser (MCA) with ATOMKI Palmtop software installed on a desktop PC.

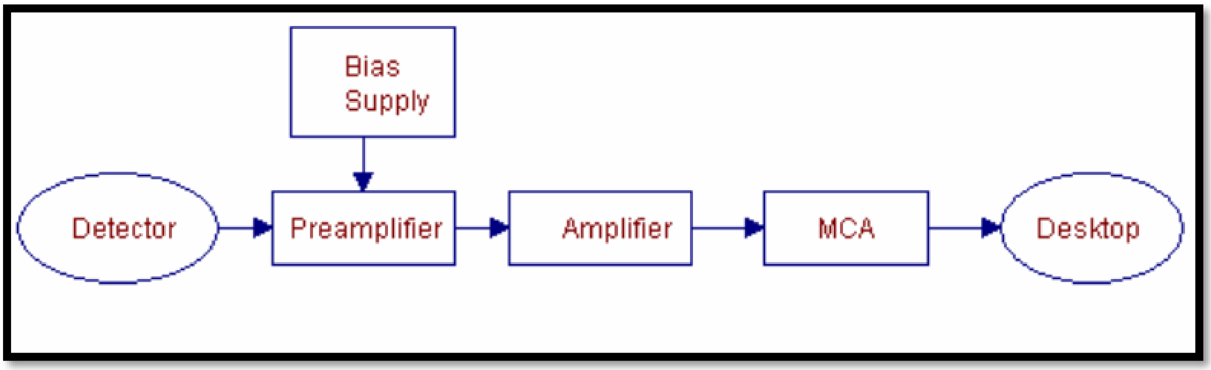

**Figure 3. 4:** Schematic diagram of the electronics of the HPGe detector [Mba07].

### 3.2.1 Detector bias (HV)

To collect the charge formed in the detector, a bias voltage must be placed across the detector. Radiation detectors need application of an external high voltage for their proper operation. This voltage is known as detector bias, and the high voltage supplies used for this task are often called detector-bias supplies [Deb88; Leo87]. For the ERL system, a SILENA model 7716 was used with a bias voltage of approximately +3500 voltage [Can99] applied across the detector junction to provide an electric field needed to clean up the charge produced in the detector crystal. The charge is collected by the preamplifier, and then moves to the amplifier. At the amplifier, the pulse shape is changed, increased in size and is more visible [Map04].

### 3.2.2 Preamplifiers

A preamplifier collects the charge pulse carriers from the detector and passes a voltage pulse to the amplifier. It provides a high impedance load for the detector and a low impedance source for the amplifier. The charge created within the detector by an interaction with the gamma radiation is collected by the preamplifier. A preamplifier may be sensitive to charge, current or voltage. It has advantages in terms of noise performance because the gain is independent of detector capacitance [Gil08]. The ERL HPGe detector has a built-in preamplifier (model 2002 CSL). To minimize the electronic noise, the input stage of the preamplifier (usually a field-effect transistor stage) is cooled in the same manner as the detector; this increases energy resolution, therefore reducing the chances for thermal excitation of charge, which could bring about leakage current [Deb88].

### 3.2.3 Amplifier

An amplifier is an electronic device for increasing the height of an electronic signal. In gamma-ray spectrometry, the amplifier performs many other pulse processing functions. The output signal from the amplifier is in a range of few millivolts. As a result, it cannot travel very far without losing information or being lost in the noise. The amplifier plays two roles: amplifying and shaping the signal. The signal needs to be shaped to increase the signal-to-noise ratio. An appropriate shaping time can minimize the noise contribution. The longer the amplifier's shaping time, the better the resolution for the peaks. The pulse requires to be shaped to a more convenient form. Hence, the amplifier's frequency response is set by a shaping time constant, τ, which is 6 µs for the ERL detector system [Can99]. The gain drift of the amplifier is caused by small changes in the characteristics of the resistors and capacitors, because of temperature changes [Gil08; Sed03]. The signal coming from preamplifier goes to the amplifier, which has the function of shaping pulses coming from the preamplifier and reducing pile-up.

### 3.2.4 Multi-Channel Analyser (MCA)

The MCA is used for collecting, counting and storing pulses as a function of their height. The pulse heights are in analog form from the amplifier and they are converted to digital quantities by the Analog-to-Digital Converter (ADC) within the Palmtop device. MCA stores the sorted data, displays the data, does the pre-analysis and prepares the results for the output on a desktop PC. The sorted data are first digitized, and then displayed as counts versus channel number [Hla07]. The ERL setup has ATOMKI Palmtop software installed on a desktop PC to process the data. The MCA diagram is shown in Figure 3.5:

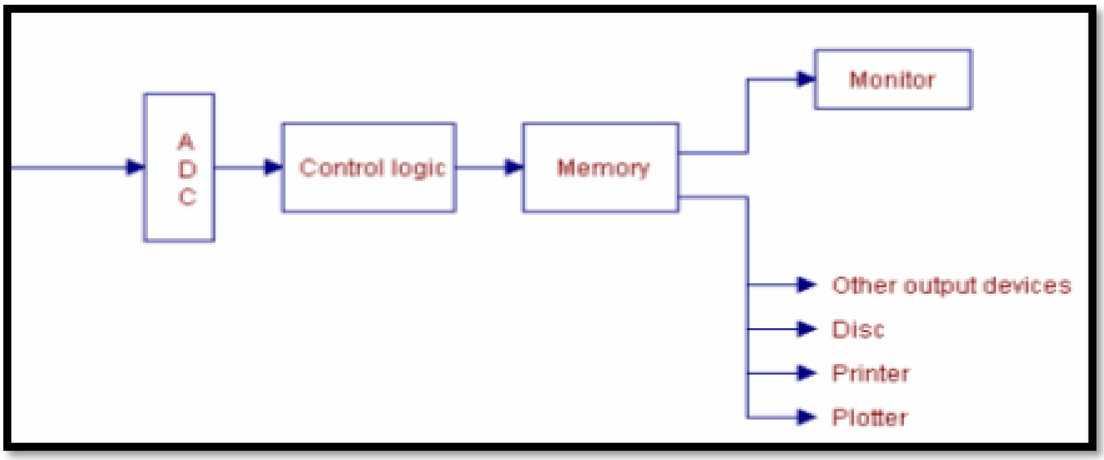

**Figure 3. 5:** Basic architecture of an MCA [Mba07].

### 3.2.5 Shielding

The HPGe detector system is placed in a low-background environment by surrounding the detector crystal with 10 cm thick lead castle to reduce room background. The castle has 2 mm thick copper lining inside to attenuate the low-energy X-rays generated by gamma-rays in the lead.

## 3.3 Sampling or samples

In this subsection, there will be a detailed discussion of various samples (mainly reference source materials) and how they were used in this study.

### 3.3.1 Types of samples (certified reference materials)

Types of sources under study includes point sources, powder and/or soil-like source, and liquid source. There are six certified reference point sources ($^{60}$Co, $^{152}$Eu, $^{137}$Cs, $^{22}$Na, $^{241}$Am and $^{133}$Ba). The point sources were prepared and certified by National Metrology Institute of South Africa (NMISA) (see details in appendix A, Table A.6). NMISA prepared the button source by dispensing an accurately weighed aliquot of a standardized point sources master solution into a Perspex disc and evaporated the liquid to dryness. The Perspex disc was sealed by gluing a Perspex lid on the top and an additional lid was glued to the button for reinforcement. The button source activity was determined gravimetrically. A wipe test was done on the button source to determine the integrity of the source. As a confirmation for the source activity determined gravimetrically, a comparative measurement was made with the NMISA secondary calibrated ionization chamber. The results of the measurements are traceable to the relevant national measurement standards [Nmi14].

Other types of reference samples used are standard reference sources from the International Atomic Energy Agency (IAEA), of which four were in powder (relatively fine) form and one soil (relatively coarse) form. The sources include $^{232}$Th ore (IAEA/RGTh-1), $^{238}$U ore (IAEA/RGU-1), $^{40}$K ore (IAEA/RGK-1), potassium chloride (KCl) and a soil reference source (IAEA-375). For counting and study purposes, these reference sources were transferred to 1 L Marinelli beakers and 100 mL pill bottle sample holders for this study. To remove moisture, sources were dried overnight at 105°C inside an Eco Therm LABOTEC oven. After drying, the sources were transferred directly into relevant sample holders. Then, the prepared samples were weighed before and after sealing with silicon sealant and their weights were recorded in the sample preparation book. Finally, a liquid standard source prepared by the Council of Scientific and Industrial Research (CSIR) in a 1 L Marinelli beaker volume, with a mixture of, $^{60}$Co, $^{137}$Cs and $^{152}$Eu radionuclides was also used in this study. Table A.4 shows the certification values, whereby source preparation procedures for this liquid standard source are stated.

## 3.3.2 Sample geometry

Table 3.1 summarises all radionuclides from the reference sources used in this study, with the type of sample holder geometries used. All sources were counted on the ERL HPGe detector system for 24 hours acquisition time. $\gamma$-emitting radionuclides from reference sources were used in this study. In Table 3.1, the tick (**✓)**, represents the availability of the $\gamma$-source in the given geometry. Altogether, 16 sources (6-point sources, 6 Marinelli beaker sources and 4 pill bottle sources) were available and listed in Table 3.1.

Figure 3.6 shows the reference sources used for the study of point source geometry. When measuring samples in large quantities or volumes, it is advisable to place samples closer to the detector crystal as to optimise the gamma-ray detection efficiency. Figure 3.7 shows the 100 mL polyethylene pill bottle with a length of 5.5 cm and diameter of 5.0 cm. In this study, the Marinelli beaker was a suitable and available sample holder to be used for large volume samples. The available Marinelli beaker used in the ERL is a 1 L polypropylene beaker, manufactured by AEC-Amersham, with an 85 mm annular bottom (so that it can slide over the HPGe detector). The first Marinelli beaker was designed by L.D. Marinelli in the early 1940s and was used mainly for biological applications in 1943. The Marinelli beaker reduces the effect of sample self-shielding and improves the detector's efficiency for counting emitted radiation from the sample [Oak99]. In Figure 3.8 the Marinelli beakers with yellow lid or cap are used for other solid samples (e.g. powder).

**Table 3. 1:** Table summarizing **$\gamma$**-source and geometries used for experiments in this study.

| **$\gamma$-Source** | **Point source** | **Pill bottle** | **Marinelli beaker** |
|---|---|---|---|
| $^{241}$Am | ✓ | | |
| $^{133}$Ba | ✓ | | |
| $^{60}$Co | ✓ | | ✓ |
| $^{137}$Cs | ✓ | | ✓ |
| $^{152}$Eu | ✓ | | ✓ |
| $^{22}$Na | ✓ | | |
| $^{40}$K | | ✓ | ✓ |
| $^{232}$Th | | ✓ | ✓ |
| $^{238}$U | | ✓ | ✓ |
| $^{134}$Cs | | | ✓ |
| $^{129}$I | | | ✓ |
| $^{226}$Ra | | | ✓ |
| $^{106}$Ru | | | ✓ |
| $^{125}$Sb | | | ✓ |

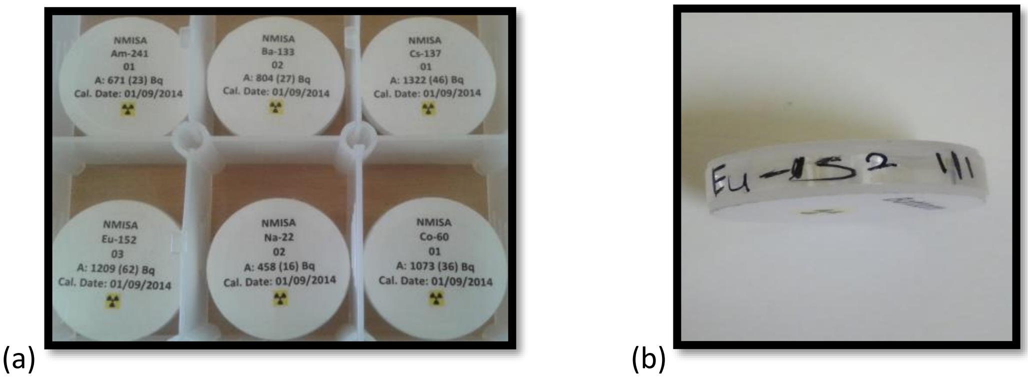

**Figure 3. 6:** (a) A photograph of six certified reference point sources and (b) a photograph showing a Perspex holding point source ($^{152}$Eu).

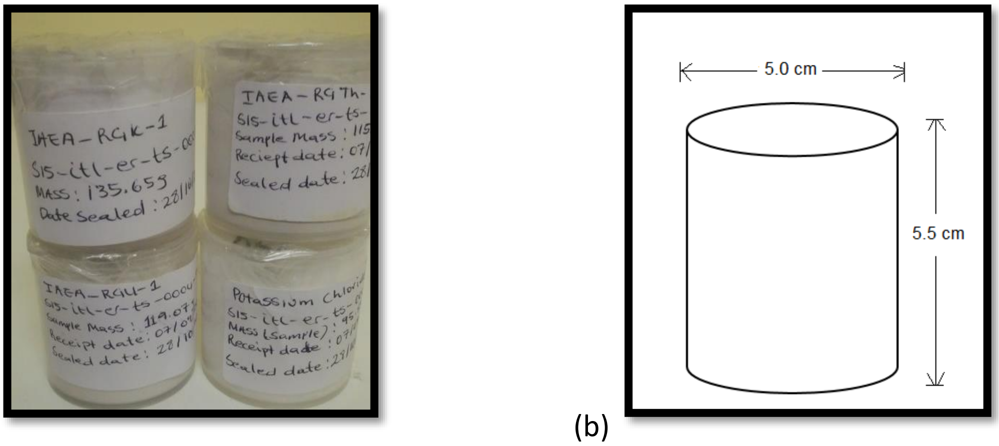

(a) (b)

**Figure 3. 7:** (a) A photograph of four pill bottles with prepared reference sources and (b) a schematic diagram showing all the pill bottle dimensions.

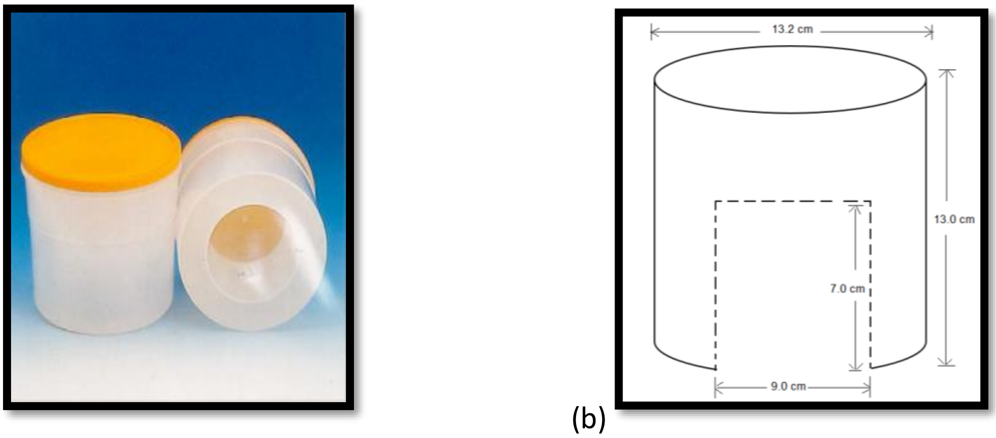

(a) (b)

**Figure 3. 8:** (a) A photograph of empty Marinelli beakers and (b) a schematic diagram showing all the Marinelli beaker dimensions.

(a)

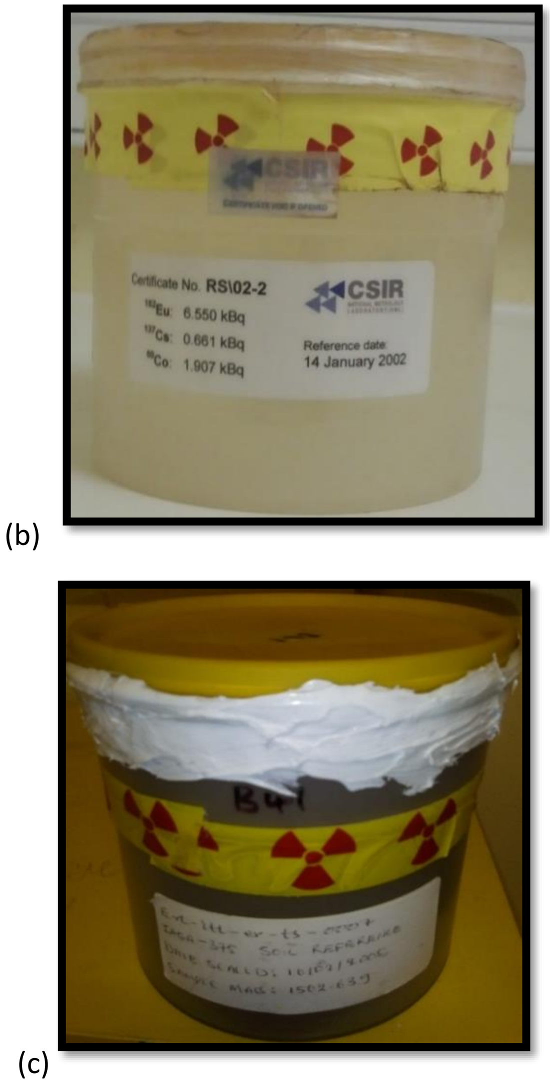

**Figure 3. 9:** (a) A photograph of four Marinelli beakers with powder reference sources, (b) liquid reference source, and (c) soil reference source.

## 3.4 Experimental Data Analysis

In this study, reported activity concentration of reference sources were used to calculate the detection efficiency. Activity concentrations of radionuclides present in samples can be determined using the following expression:

$$A_c(Bq/kg) = \frac{Counts}{m * \varepsilon * B_r * t} \tag{3.1}$$

All the parameters in equation (3.1) were described in the motivation of this study (see Section 1.1 of Chapter 1). The ATOMKI Palmtop software is used to set the regions of interest

(ROIs) manually around the full-energy peak of interest. The software uses its in-built algorithm to calculate the net peak counts as well as their errors [Ong13]. For reference sources used in this study, the activity concentrations of present radionuclides were given in the certificates.

Re-arranging equation (3.1), the full-energy peak efficiency is given by

$$\varepsilon = \frac{Counts}{A_c * B_r * t * m} \tag{3.2}$$

Equation (3.2) was used to calculate the full-energy peak efficiency for each gamma-ray energy of interest.

### 3.4.1 Standard reference sources in Marinelli beaker and pill bottle

The elemental concentrations of standard reference sources were converted from ppm (parts per million) to activity concentrations (Bq/kg). The standard reference sources were prepared for the Marinelli beaker and pill bottle sample holder geometries, which are; $^{232}$Th ore (IAEA/RGTh-1), $^{238}$U ore (IAEA/RGU-1) and $^{40}$K (potassium sulphate) (IAEA/RGK-1) as well as potassium chloride (KCl). The method used to determine the activity concentrations is presented below. This procedure is then followed by a table showing the activity concentrations of the standard reference sources, together with their corresponding masses for a sample holder.

The calculations of $^{232}$Th, $^{238}$U and $^{40}$K activity concentrations are shown in the following boxes, respectively. The activity concentration from Table 3.2 were calculated with the values of reference source concentrations given in IAEA certificate in Appendix A, Table A.1 to A.3.

$^{232}$Th concentration = (800 ± 16) µg/g

1 Bq/kg of Th is equivalent to 246 ng/g [Rad16]

Therefore, (800 ± 16) µg/g of $^{232}$Th = (**3252.0 ± 65**) Bq/kg

$^{238}$U concentration = (400 ± 2) µg/g

1 Bq/kg of U is equivalent to 81 ng/g [Rap16]

Therefore, (400 ± 2) µg/g of $^{238}$U = (**4938.3 ± 25**) Bq/kg

Potassium concentration= (44.8± 0.3) %

1 ppm is equivalent to 0.0001% [Rap16]

1 ppm ~1 x $10^{-6}$ = 0.0001%

Therefore, concentration of $^{40}$K = 448000×$10^{-6}$g/g

1 Bq/kg of $^{40}$K = 32.3x$10^{-6}$g/g [Rad16]

Therefore, (44.8± 0.3) % of $^{40}$K = (**13870 ± 93**) Bq/kg

Calculations of activity concentration of $^{40}$K potassium chloride (KCl) in pill bottle: 95.56 g:

- The number of moles in 95.56 g KCl is determined as:
  $$\frac{\mathrm{KCl_{mass}\ (g)}}{\mathrm{KCl_{molar-mass}\ (g.mol^{-1})}} = \frac{95.56\ \mathrm{g}}{74.551\ \mathrm{g.mol^{-1}}} = 1.28\ \mathrm{mol\ of\ KCl}$$
- 1.28 mol KCl is equivalent to about 7.7 x $10^{23}$ atoms of KCl from Avogadro's number [(6.02 x $10^{23}$) x (1.28)]. Hence there are 7.7 x $10^{23}$ atoms of K [Mal10].
- In nuclei of K, about 0.0117% is $^{40}$K [Fuj09]. Therefore, the number of $^{40}$K nuclei present is given by:

  $\mathrm{N} = (7.7 \times 10^{23}) \times (1.17 \times 10^{-4}) = 9.03 \times 10^{19}$ Nuclei of $^{40}$K.
- Activity (A) of a radioisotope source is defined as the rate of decay, the fundamental law of radioactivity [Kra88]:

$$\mathrm{A\ (Bq)} = \mathrm{N} \times (\ln 2/\mathrm{t}_{1/2}) \qquad (3.3)$$

Since $t_{1/2}$ of $^{40}$K = [(1.277 x $10^{9}$ years) x (3.154 x $10^{7}$ seconds)] 4.0298 x $10^{16}$ seconds [Fir96], the activity A (Bq) of $^{40}$K in the source was calculated to be **1553 Bq**

Thus, the $^{40}K$ activity concentration in KCl powder was found to be (**16251.6 ± 90)** Bq/kg

Calculation of activity concentration of $^{40}K$ in the RGK-1 ($K_2SO_4$) reference source in pill bottle: 135.65 g:

- The number of moles in 135.65 g $K_2SO_4$ are determined as:
  $\frac{135.65\text{ g}}{174.26\text{ g.mol}^{-1}} = 0.778\text{ mol of }K_2SO_4$

- 0.778 mol $K_2SO_4$ is equivalent to about 4.7 x $10^{23}$ atoms of $K_2SO_4$. Hence there are 9.4 x $10^{23}$ atoms of K [Mal10].
- In nuclei of K, about 0.0117% is $^{40}K$ [Fuj09]. Therefore, the number of $^{40}K$ nuclei present is given by:

  $\mathrm{N} = (9.4 \times 10^{23}) \times (1.17 \times 10^{-4}) = 1.1 \times 10^{20}$ Nuclei of $^{40}K$.

With $t_{1/2}$ of $^{40}K$ = [(1.277 x $10^{9}$ years) x (3.154 x $10^{7}$ seconds)] 4.0298 x $10^{16}$ seconds [Fir96], the activity A (Bq) of $^{40}K$ in the sample was calculated to be **1887 Bq**.

Thus, the $^{40}K$ activity concentration in $K_2SO_4$ was found to be **(13910.8 ± 93)** Bq/kg

**Table 3. 2:** Sample concentration taken from certificates and converted from ppm to Bq/kg (or Bq/L).

| ERL sample code | ERL spectrum code | Mass/Volume of the source | Activity Concentration |
|---|---|---|---|
| S15-itl-er-ts-0003-A | RTh-date | 0.12 kg | (3250 ± 70) Bq/kg |
| S15-itl-er-ts-0002-A | KCl-date | 0.10 kg | (16250 ± 90) Bq/kg |
| S15-itl-er-ts-0004-A | RGU-date | 0.12 kg | (4940 ± 30) Bq/kg |
| S15-itl-er-ts-0001-A | RGK-date | 0.14 kg | (13910 ± 90) Bq/kg |
| Erl-itl-er-ts-0006 | RTh-mb-date | 1.37 kg | (3250 ± 70) Bq/kg |
| Erl-itl-er-ts-0009-B | KCl-mb-date | 1.29 kg | (16250 ± 90) Bq/kg |
| Erl-itl-er-ts-0005 | RGU-mb-date | 1.41 kg | (4940 ± 30) Bq/kg |
| S10-itl-inh-ts-0009 | RGK-mb-date | 1.45 kg | (13910 ± 90) Bq/kg |
| Erl-itl-er-ts-0007 | Soil-mb-date | 1.50 kg | (2930 ± 120) Bq/kg |
| Erl-itl-er-tl-0001 | Liquid_source-date | 1.00 L | (3000 ± 200) Bq/L - Eu152, (900 ± 40) Bq/L - Co60 and (4610 ± 13) Bq/L - Cs137 |

ERL sample code notation in Table 3.2 are derived from the following information:

S15 represent Sample of 2015 - itl (from iThemba LABS) - er (from environmental radioactivity) - ts (type soil, or tl for type liquid) - 0003-A (sample number).

ERL (Environmental radioactivity laboratory)

inh (referring to in house sample).

### 3.4.2 Energy calibration

Energy calibration is often performed before acquisition of the spectrum as part of the setting-up procedure [Gil08]. The main purpose of the energy calibration is to derive the relationship between the peak position in the spectrum (channel number) and the corresponding gamma-ray energy. This is done by measuring the spectrum of a gamma-ray emitting source with precisely known energy and comparing it to the measured peak position. The energy calibration is obtained by determining the centroids of the gamma-lines with known energies, and by fitting a polynomial function to the curve of centroid versus gamma-ray energy. The MCA system allows one to specify the energy associated with each relevant centroid channel corresponding to a region of interest. By performing this action, the parameters for the fit, polynomial or linear can be obtained.

#### 3.4.2.1 ERL Energy calibrations

At the iThemba LABS ERL, the system is calibrated weekly (every Monday) with the $^{232}$Th Ore (IAEA/RGTh-1) reference source. The photo peak energy ($E$) is represented as a linear function of channel number;

$$E = A + B(Ch) \tag{3.4}$$

where $E$ is the energy (in keV) and $Ch$ is the channel number. $A$ and $B$ are the parameters determined for the energy as a function of channel number. The MCA system (ATOMKI Palmtop MCA) in use at the ERL allow the user to choose between first-order (linear) or second order (quadratic) equations that use a least square fit to data points. In the MCA system, one can specify the energy associated with each relevant centroid channel corresponding to a region of interest [Mba07]. Figure 3.10 shows an energy calibration curve from the energy gamma-ray lines (see Table 3.3) used in ERL for energy calibration.

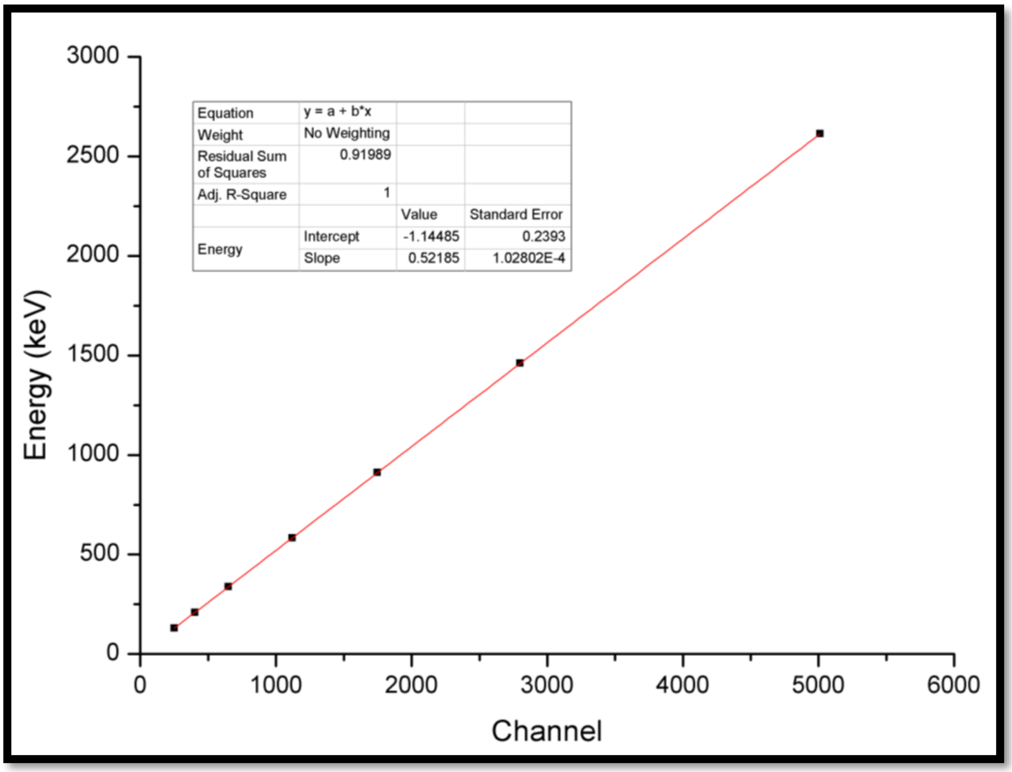

**Figure 3. 10:** Energy calibration curve from selected gamma-ray lines of $^{40}$K and $^{232}$Th decay series.

**Table 3. 3:** List of isotopes from $^{40}$K and $^{232}$Th decay series used for energy calibration.

| **Radionuclide** | **Energy (keV)** | **Corresponding Channel number** |
|---|---|---|
| $^{228}$Ac | 129.1 | 250 |
| $^{228}$Ac | 209.3 | 403 |
| $^{228}$Ac | 338.3 | 651 |
| $^{208}$Tl | 583.2 | 1120 |
| $^{228}$Ac | 911.2 | 1748 |
| $^{40}$K | 1460.8 | 2800 |
| $^{208}$Tl | 2614.5 | 5013 |

### 3.4.3 Experimental spectra for volume sources and background spectra

The full-energy count rate spectra (experimental) of environmental samples always require background subtraction. For the final spectrum of each sample/source, the background contribution must be subtracted to account for the contribution of the sample/source alone. The background and sample spectra are counted in fixed settings, while the background is counted with the empty lead (Pb) castle. For the arrangements at the ERL facility, background spectra are only collected over weekends, for about 2.5 days (Friday evening till Monday morning). The spectra as shown in Figure 3.11 shows consistencies with no major variation between the (three background) spectra collected in different months. The spectra total count rate for backgrounds 1, 2 and 3 have values of 2.285 cps, 2.274 cps and 2.288 cps respectively.

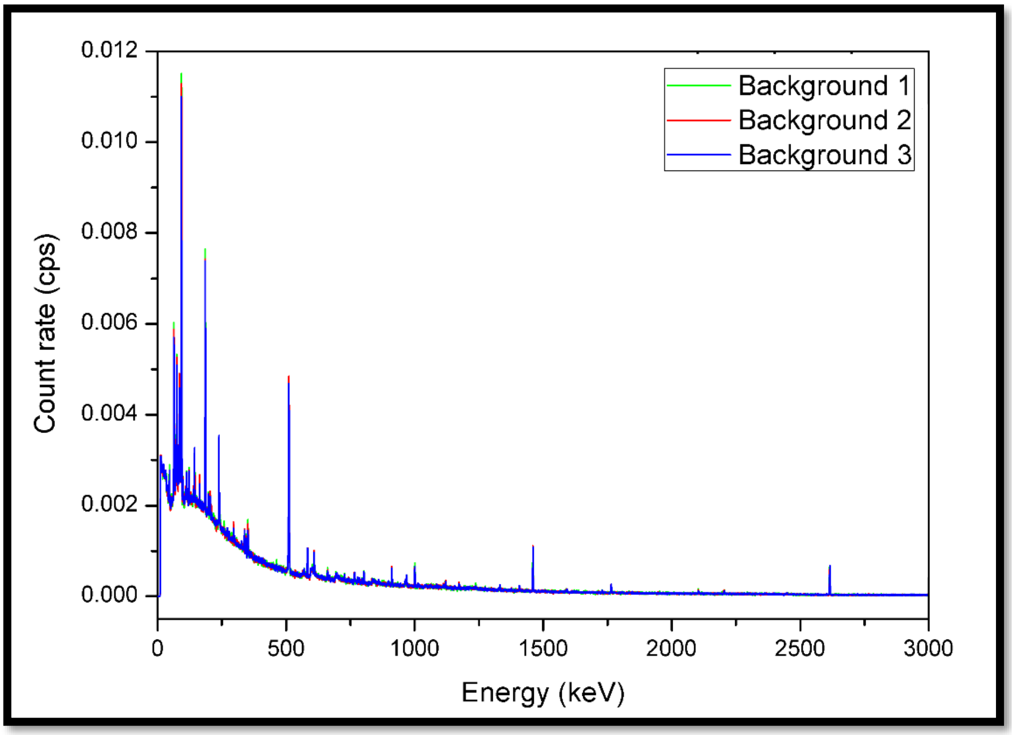

**Figure 3. 11:** Three different background spectra counted in different months [0 keV – 3000 keV].

# Chapter 4: Monte Carlo (MC) simulation

## 4.1 Introduction

In this study, MC simulations were used for volume source (pill bottle and Marinelli beaker) geometries to optimise the efficiency of the HPGe detector system as function of energy for various sample geometries. The MC method is a well-known application to reproduce the detector response and to perform the calibration for a variety of matrices and for accurate geometries [Azb15]. In another study by Azbouche *et al*. [Azb15], MC geometrical model was used to validate measurements obtained using standard sources provided by the supplier. In this study, the MC model was also used for similar measurement configuration, point source, pill bottle and Marinelli beaker geometries for the determination of the efficiency curve. All point sources available are single radionuclides, unlike the volume sources which are usually a combination. Thus, the point sources provide additional advantage in the optimization of the detector parameters. Monte Carlo N-Particle (MCNP) code [Pel08] is useful for coincidence summing correction and efficiency determination at various source to detector geometries, complex source shapes as well as Marinelli beaker models for HPGe detectors [Ewa01; Lab00].

To fulfil these conditions, the simulation method is to be compared with the experimental method of determining efficiencies at specific geometries using certified radioactive sources and gamma emission probabilities [Ewa01].

## 4.2 Monte Carlo methods

MC refers to a statistical method in which expected characteristics of particles are evaluated by sampling a substantial number of individual particle histories whose trajectories are simulated by a digital computer [Van15]. MC methods are used to model random processes. In the past, decades ago, the technique required the status of a developed numerical method capable of addressing most complex applications.

In numerous applications of MC, a physical process is simulated directly. The only condition is that the mathematical or physical system be described by probability density functions (PDFs). Once the PDFs are known, a random sampling from the PDFs can be proceeded by MC simulation. Many simulations are subsequently performed, and the desired result are taken as an average over the number of observations [Dam05]. In MC calculations, the histories or particle tracks are generated by simulating the random nature of the particle interactions with the medium. To perform this, mathematical expressions are required for the probability relationships, which are all stochastic variables. MC methods are used in radiation transport applications such as detector response determination, shielding analysis and dosimetry [Van15].

The fundamental advantage of MC techniques over numerical solutions is that the geometry and nuclear data are represented more accurately than in deterministic techniques [Van15]. Deterministic techniques need reasonably uncomplicated geometries for the numerical technique to work, and they use the multi-group approximation to cross-section data [Van15]. The disadvantage of the MC technique is that it is statistical in nature and does not supply an exact solution to the problem [Van15]. All results represented are estimated with associated uncertainties. Also, MC techniques can be computationally unfeasible if small uncertainties are needed. The relationship between deterministic techniques and MC techniques is that the deterministic techniques provide a highly exact solution to a significantly simplified approximation of the problem, while MC techniques provide an approximate solution to a highly exact representation of the problem [Van15].

A calculation approach that yields acceptable results is the MC method which is based on the simulation of individual photon histories. Every photon is tracked on its path from its origin inside the source through the source material into the detector. Each particle may experience several scattering interactions before leaking or being absorbed from the system. The photons interact by photoelectric absorption, Compton scattering or pair production, whereby electrons and positrons are created [Deb88; Van15].

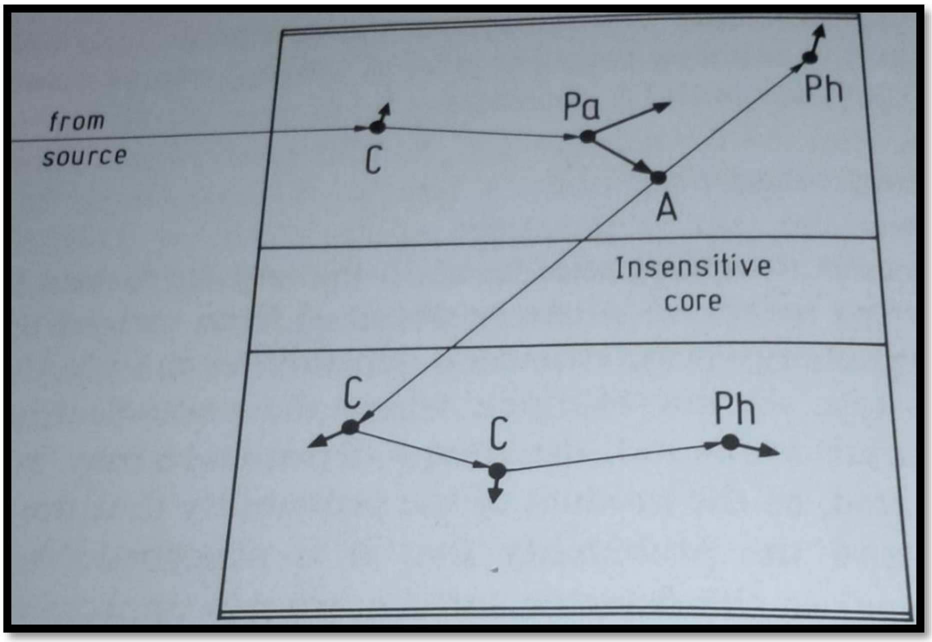

**Figure 4. 1:** Diagram showing the history of a photon in a coaxial detector Ph represents photoelectric absorption, C represents Compton scattering, Pa represents pair production, and A represents annihilation [Deb88].

In MC simulations, an individual particle or photon is tracked from its original creation up until termination with the interaction scheme, based on corresponding cross-sections and physical interactions. The particle or photon is created randomly picking the source energy (E), the initial direction (Ω), and starting location (r). During the particle or photon transport, for every interaction, a type and location are recorded. Therefore, a decision is made concerning the new remaining direction and energy. This process is repeated until the photon or source particle and all its secondary particles or photons have deposited all their energies or have reached a non-significant region [Hen02]. An example of MC simulation process for radiation transport in energy deposition estimator is shown in Figure 4.2. All processes are based on equations describing the physical processes and decisions based on random numbers and cross-section tables.

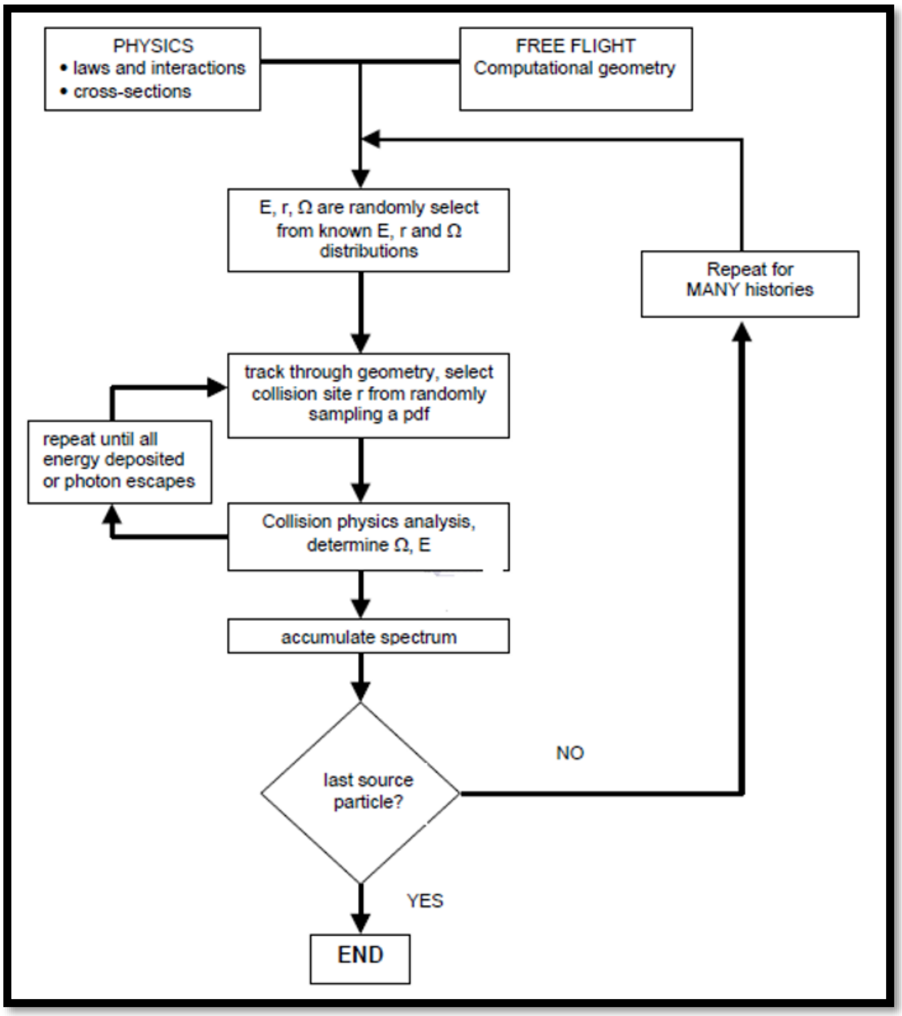

**Figure 4. 2:** An illustration indication radiation transport in MC simulation for energy deposition tally [Hen02].

## 4.3 MCNPX

There are various MC codes that are available for various applications. Some of the most popular codes include, MCNPX [Pel08], FLUKA [Fer05], PENELOPE [Sal01], and GEANT4 [Ago03]. For this study, the MCNPX simulation code was used. MCNPX stands for MC N-Particle eXtended code [Pel08]. MCNPX is a general-purpose MC radiation transport code designed to track about 34 particle types over a broad range of energies. MCNPX is the next generation in the series of MC transport codes that began at Los Alamos National Laboratory (LANL) nearly sixty years ago. MCNPX 2.7.0 is the latest Radiation Safety Information Computational Center (RSICC) release of the code, succeeding the 2005 release of MCNPX (2.5.0) [Pel08]. MCNPX is fully three-dimensional in its modelling abilities. It can model three-dimensional objects in space in exact or near exact geometry [Van15]. MCNPX includes many new capabilities, particularly in the areas of transmutation, delayed particle production and burnup [Pel08]. MC simulations are vital to assess the summing effect of radionuclides that emit gamma-rays in cascades [Pel08].

An estimate within MCNPX allows the calculation of the pulse-height distribution within the detector. In obtaining this estimate, the total energy deposited in the detector is simulated for every starting photon, including the energy deposited by all secondary events that are produced through its journey. Upon creation, these secondary particles are temporarily stored for later analysis, until the track of the primary event is completed. Afterwards, the track of each secondary event is simulated, and its contribution determined. At the end, the contributions are combined to constitute the total energy deposited in the detector for this primary photon. A histogram of the contribution of all primary particles gives the needed pulse-height distribution.

Because of the procedures, coincidence-summing effects cannot be simulated in standard MCNPX. The timing properties of the detector are not given as an input to the code, and no information is accessible on the duration of a complete photon track in real-time. It should be noted that the processes taking place in the detector system after the energy deposition in the detector (signal processing) are not simulated with MCNPX.

### 4.3.1 Structure of MCNPX input data file

In performing the MC simulations with MCNPX codes, it is required that the user provides an input file that extensively describes all characteristics of the simulated physical system [Pel08]. The MCNPX input file is categorised by three sections, namely cell cards, surface cards and data cards, and these sections are separated by blank space in between [Pel08]. More details regarding the command lines and requirements for the MCNPX input file can be found in the manual [Pel08] or any other MCNP-related documents.

Below is an extract and description of various input cards used in MCNPX. These cards are important in writing and running input file. To demonstrate the importance of input file, some sections from $K_2SO_4$ input used in this study will be presented. The box below describes the command line for the detector description used in the simulation for a cell card example. The first line starting with c is a comment line. In the second line, is the cell number represented by 1 (this is unique and cannot be repeated anywhere else again in the cell card). The cell number is followed by the material number, represented by 1, which will be defined at the data card section on the input. Following the material number is the material density, with a minus sign (referring to g.cm$^{-3}$ units). The material density is then followed by the boundary surface numbers (to be defined in the surface card section). Finally, the level of importance for particles is provided (importance: photons, electrons=1) in this cell (or region). Where specified, a zero (0) importance refers to a non-important region, while a +number importance indicates an important region relative to others.

```
c Germanium crystal
1 1 -5.323   (33:-18:34) -1 18 -3     imp:p,e=1
```

The next follow-up information after all cell cards have been included is for the surface cards. In the box below is an example of a surface card. The number 33 refers to the surface number (unique and cannot be repeated within the surface cards), CY is for the surface type (with C indicating a cylinder in the Y-axis), and then the radius of the cylinder (0.425, in cm) is provided. The information after the $ sign is read as comments by the code.

```
33 CY 0.425       $ core diameter
```

Following the surface cards are the data cards. In this section of the input file, various types of information are defined. For example, the source information, material information, tally (estimator) information, type of particles/photons transported, number of starting particles, etc. are defined in this card. The following example is for the source definition (sdef) card and only one is allowed in the input file. Source specification is used to specify the type of radiation particle to run with various parameters to all properties of the source, position and energy. In the box below, after the sdef command is the position of the starting particle in cell 9 (also coordinates are allowed); then **rad**ial description (defined in distribution 1); followed by the **ext**ension (defined in distribution 2), en**erg**y of the particle (in MeV), axial position (on the y axis in the example) and **par**ticle type whereby 2 refers to photons, refer to [Pel08] for the descriptive numbers of various particles.

```
sdef cel=9 rad=d1 ext=d2 erg=1.46083 axs=0 1 0 par=2
```

For the tally type specification command: the tally is the requested result i.e. answer calculated by MCNPX. The fc18 card is the tally comment card, where one is allowed to any information to describe the properties of estimate required (note this is optional). It is good practice to describe the modification in a comment card that will be printed in the output file for the calculation [Shu10]. Tally F8 :<pl> is the energy distribution of pulses created in a detector by radiation. For pulse-height tallies photons or electrons are a special case: F8: P,E is the same as F8:P and F8:E [Pel08]. Tally card F8 and F18 belong to the F8 tally type, and the first number (1) in the tally designation F18 is simply a counter [Van15]. FT18 tally card is there for special treatment for tally F8 type. The gaussian energy broadening (geb): $FWHM = a + b\sqrt{E + cE^2}$ where E (MeV) is the energy of the particle/photon, parameters a, b and c have units MeV, $MeV^{1/2}$ and $MeV^{-1}$, respectively [Pel08].

```
fc18 Broadened spectrum, 0.2% at 1.33 MeV
f18:p,e 1
ft18 geb 0 0.002 0
```

The material definition card is used to specify various materials used to fill up the cells. This card should have a unique material number, isotopic composition or elemental and cross-section compilation to be used. The arbitrary material number is the same as material number, m, on the cell card. There is a partial ZZZAAA element or nuclide identifier for each constituent, where AAA=000 indicates a naturally occurring element [Pel08]. The natural elements are not available from those listed in the XSDIR file but must be constructed on an m card by adding together the individual isotopes if they are available [Pel08]. The elements in material (m4) of $K_2SO_4$ are from the atomic number (Z) of each element.

```
m4   19000. 2 $ K2 in K2SO4
     16000. 1 $ S in K2SO4
     8000.  4 $ O4 in K2SO4
```

History or time cards: the usual method for limiting how long the input file must run, is to specify either the maximum number of source particle histories or the maximum execution time. The (nps) refers to the number of particles starting (1000000000). The (ctme) refers to

CPU (computer) time (1440 minutes) for the MC run. Then (print) refers to the request to print out specific tabular simulation information in the output file.

```
nps 1000000000
ctme 1440
print
```

For the simulations, the geometry of various settings for this study are shown in Figure 4.3. The two-dimensional views indicate the setups for the point source (Figure 4.3 (a)), pill-bottle (Figure 4.3 (b)) and the Marinelli beaker setup (Figure 4.3 (c)). The numbered regions in the diagrams are (1) core cavity (void/vacuum), (2) Ge crystal, (3) end cap (Al), (4) source and sample holder (plastic), (5) air inside the castle, (6) Cu lining and (7) Pb castle.

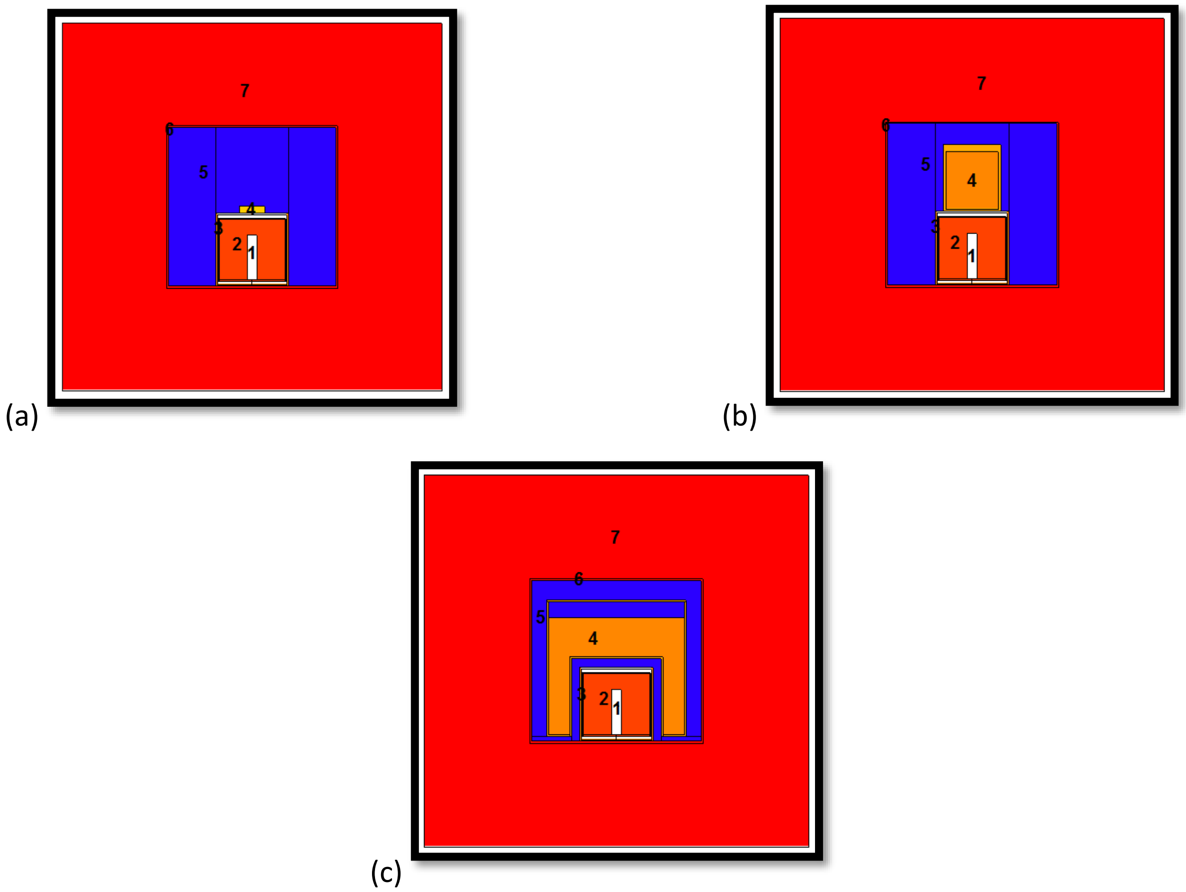

**Figure 4. 3:** Schematic diagrams of sources used in MCNPX simulation for detector with (a) point source, (b) pill bottle and (c) Marinelli beaker.

# Chapter 5: Results and discussion

In this chapter, experimental and simulated results will be presented and discussed. These are results of all radiation sources in various forms, point and volume (pill bottle and Marinelli beaker) geometries. The first set of results will focus on gamma-ray spectra (both experimental and simulated), followed by efficiency calibrations and the effect of densities for the volume sources.

## 5.1 Point source spectra

For experimental measurements, each point source (see Table 5.1) was counted for 24 hours using the ERL HPGe detector. In addition, MC simulations using the MCNPX code for the point sources were calculated for similar experimental setup, with 24 hours computer time. The experimental spectra were corrected for background contribution by subtracting the environmental background spectrum. The simulated spectra were scaled up/down using arbitrary number to match the intensities of the experimental spectra, while the counts in experimental spectra were divided by the live time multiplied by the activity of the source. Table 5.1 shows the radionuclides and their characteristic gamma-ray energies for the point sources used in this study. Only the branching ratios that are considered dominant are presented in Table 5.1. In the follow-up subsections, experimental and simulated spectra for the point sources used are discussed.

**Table 5. 1:** Point source radionuclides and their energies [Fir96].

| Radionuclide | Half-life | Energy (keV) | Gamma-ray emission probability branching ratio |
|---|---|---|---|
| $^{241}$Am | 432.2 y | 59.5 | 0.36 |
| $^{133}$Ba | 10.52 y | 80.9 | 0.34 |
| | | 276.4 | 0.07 |
| | | 302.9 | 0.18 |
| | | 356.0 | 0.62 |
| | | 383.8 | 0.09 |
| $^{60}$Co | 5.271 y | 1173.2 | 0.99 |
| | | 1332.5 | 0.99 |
| $^{137}$Cs | 30.07 y | 661.7 | 0.85 |
| $^{152}$Eu | 13.54 y | 121.8 | 0.28 |
| | | 244.7 | 0.08 |
| | | 344.3 | 0.27 |
| | | 411.1 | 0.02 |
| | | 444.0 | 0.03 |
| | | 778.9 | 0.13 |
| | | 867.4 | 0.04 |
| | | 964.1 | 0.15 |
| | | 1085.8 | 0.10 |
| | | 1112.1 | 0.14 |
| | | 1408.0 | 0.21 |
| $^{22}$Na | 2.602 y | 511.0 | 1.79 |
| | | 1274.5 | 0.99 |

### 5.1.1 $^{22}$Na point source

In Figures 5.1 and 5.2, gamma-ray spectra (experimental and simulated) for the $^{22}$Na source are presented. In Figure 5.1, Compton edge peak is observed and an additional photo-peak (at 1785.5 keV) is observed in the experimental spectrum. This additional peak is illustrated clearly in Figure 5.2. The additional photo-peak is a result of the summation of the two gamma-ray lines of $^{22}$Na (511.0 keV + 1274.5 keV = 1785.5 keV). In Figure 5.1 the difference in spectrum height is observed where experimental spectra is higher than the simulated spectra due to normalisation value in simulated spectrum. The standard MCNPX procedures cannot simulate coincidence-summing effects since no information is available on the duration of a complete photon track and the timing properties of a detector are not part of the input to the code [Pel08].

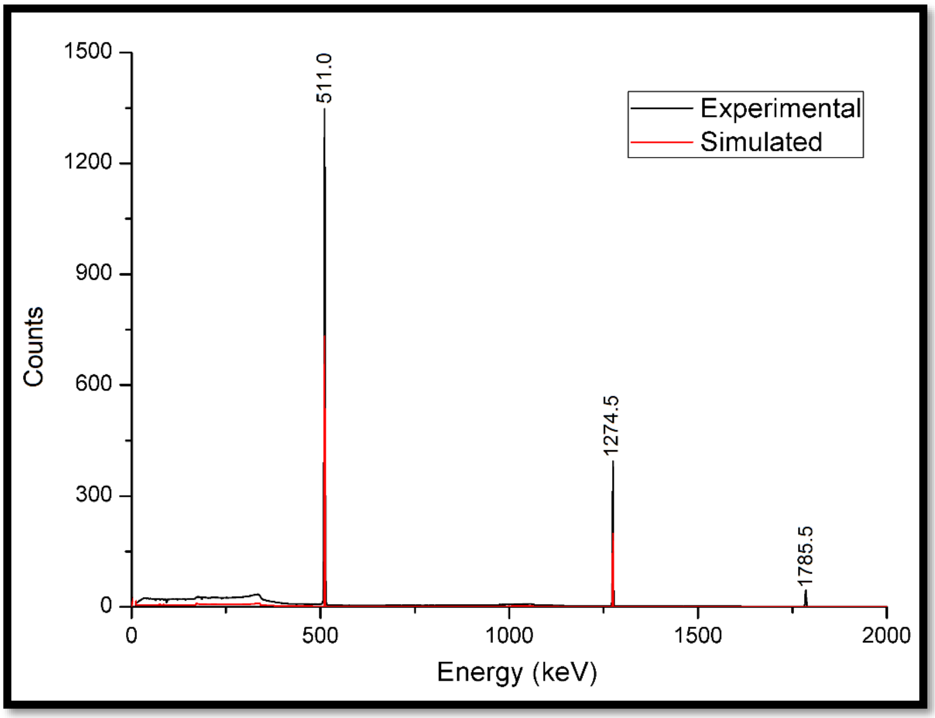

**Figure 5. 1:** The $\gamma$-ray spectra for the $^{22}$Na point source (0 keV – 2000 keV).

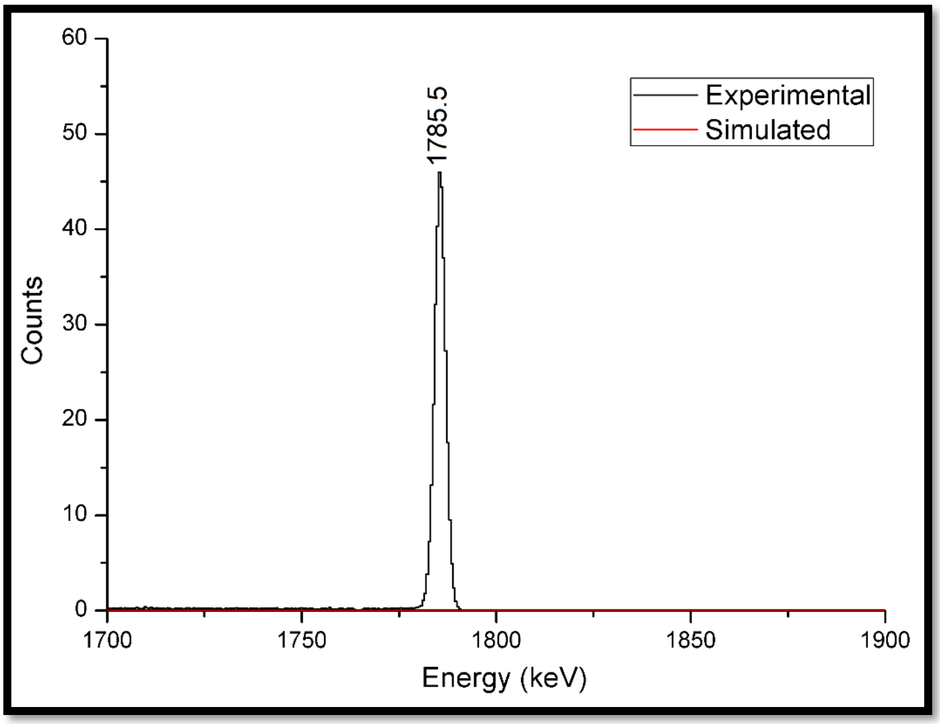

**Figure 5. 2:** The $\gamma$-ray spectra for the $^{22}$Na point source (1700 keV – 1900 keV).

### 5.1.2 $^{60}$Co point source

In Figures 5.3 and 5.4, gamma-ray spectra (experimental and simulated) for the $^{60}$Co source are presented. In Figure 5.3, an additional photo peak at 1173.2 keV + 1332.5 keV = 2505.7 keV is observed in the experimental spectrum. This is related to same effect (coincidence summing) as discussed in the $^{22}$Na subsection.

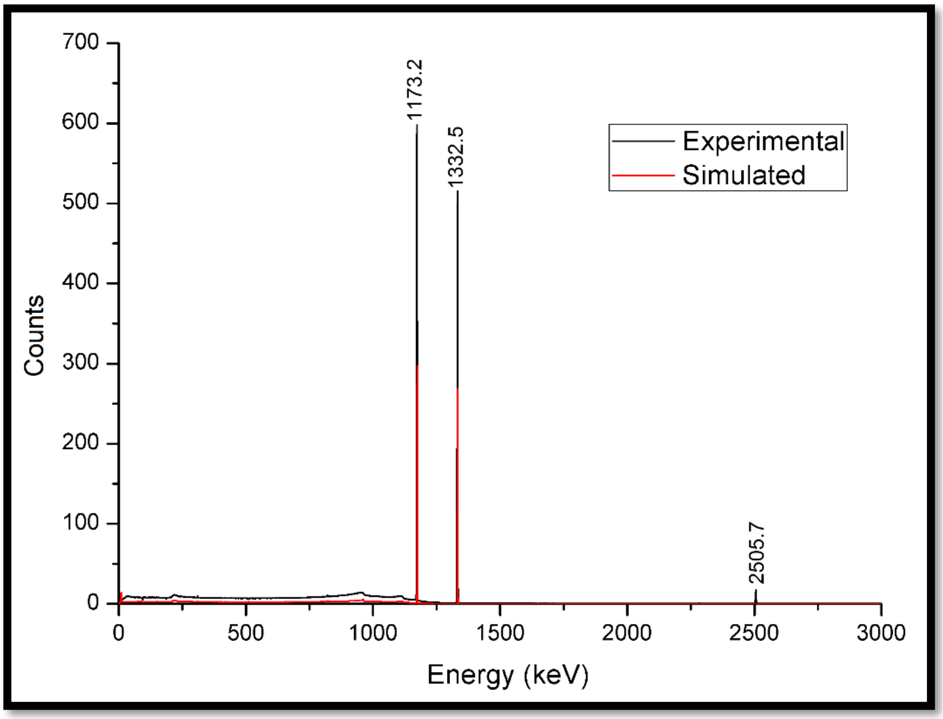

**Figure 5. 3:** The $\gamma$-ray spectra for the $^{60}$Co point source (0 keV – 3000 keV).

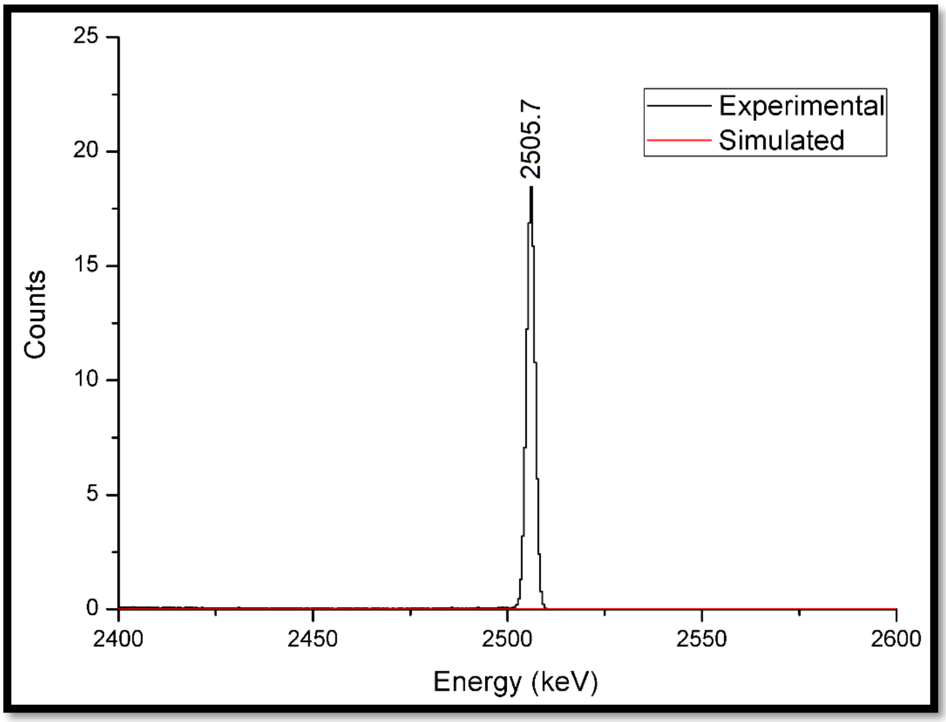

**Figure 5. 4:** The γ-ray spectra for the $^{60}$Co point source (2400 keV – 2600 keV).

### 5.1.3 $^{133}$Ba point source

In Figures 5.5 and 5.6, gamma-ray spectra (experimental and simulated) for the $^{133}$Ba source are presented. The $^{133}$Ba point source has various gamma-ray lines (see also Table 5.1) with relatively high branching ratios and, as a result, the possibility of coincidence summing is also high. The expected additional peaks of the experimental spectrum can be observed in Figure 5.5 and are not visible in the simulated spectrum. One example of the summation photo-peak, for the two-dominant gamma-ray lines (356.0 keV + 80.9 keV = 436.9 keV), is shown in Figure 5.6.

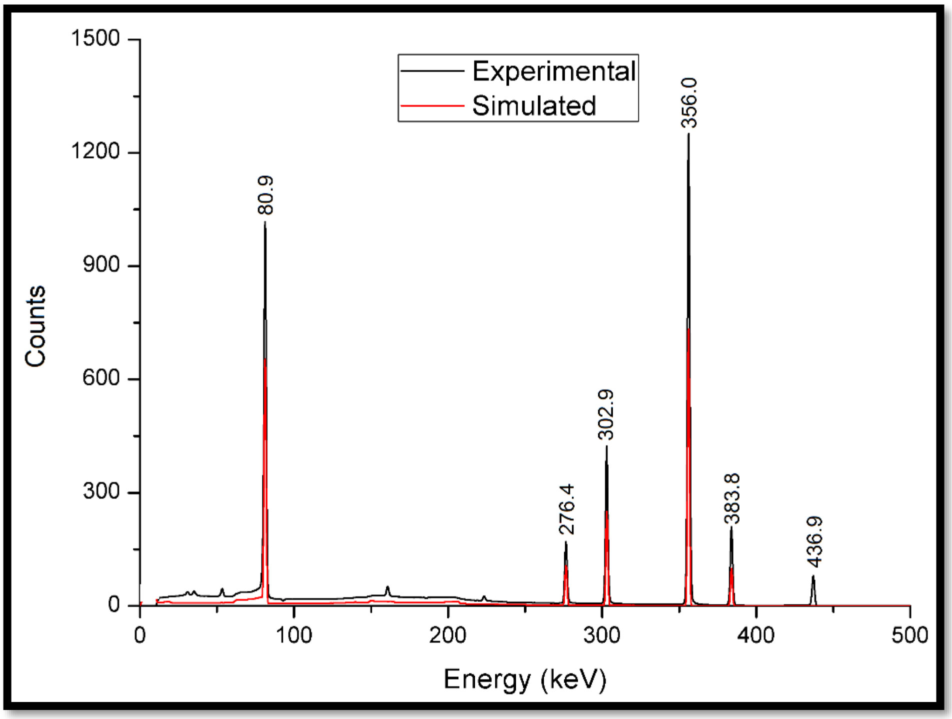

**Figure 5. 5:** The γ-ray spectra for the $^{133}$Ba point source (0 keV – 500 keV).

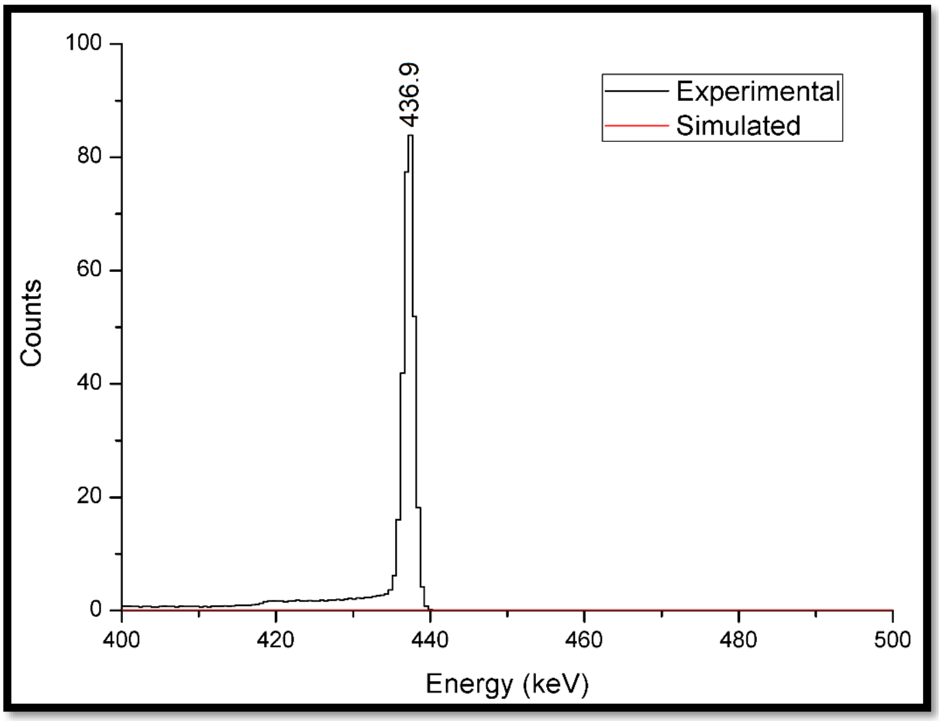

**Figure 5. 6:** The γ-ray spectra for the $^{133}$Ba in point source (400 keV – 500 keV).

### 5.1.4 $^{137}$Cs point source

In Figure 5.7, gamma-ray energy spectra for the $^{137}$Cs source is presented. As presented also in Table 5.1, $^{137}$Cs decays with an emission of a single photon with about 662 keV energy. Hence, no coincidence summing correction is required for this radionuclide.

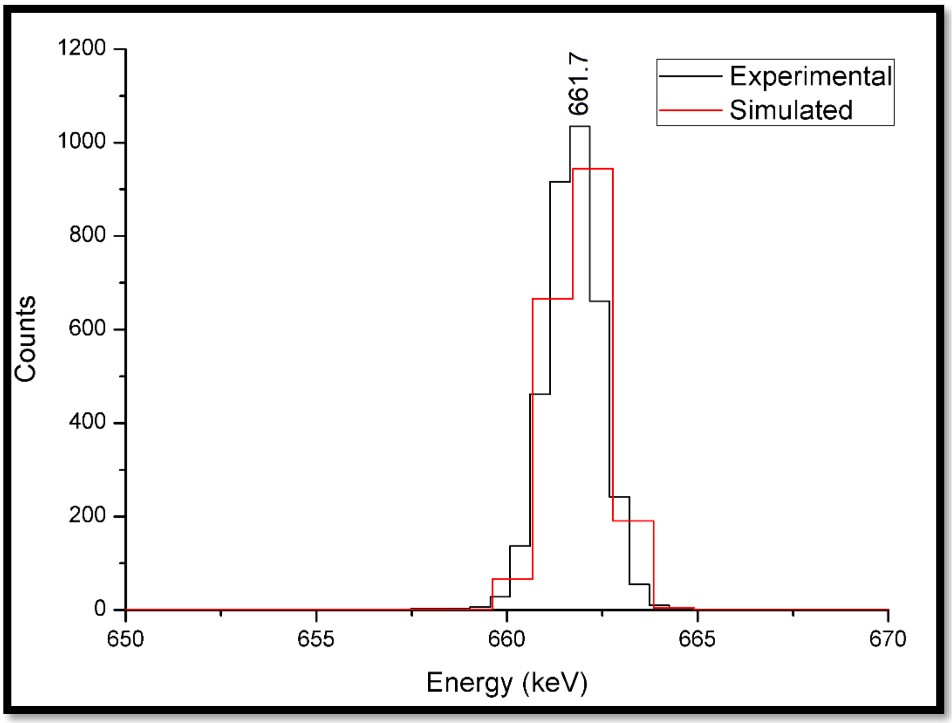

**Figure 5. 7:** The γ-ray spectra for the $^{137}$Cs point source (650 keV – 670 keV).

### 5.1.5 $^{152}$Eu point source

In Figures 5.8 and 5.9, gamma-ray spectra (experimental and simulated) for the $^{152}$Eu source are presented. Similarly, to $^{133}$Ba, the $^{152}$Eu point source has various gamma-ray lines (see also Table 5.1) with relatively high branching ratios, so the possibility of coincidence summing increases. The $^{152}$Eu nuclide decays by two branches (refer also to Figure 2.8), $^{152}$Sm (72%) and $^{152}$Gd (28%) [Fir96]. In Figure 5.9, one of the summation photo-peak in the $^{152}$Eu experimental data is shown. This additional energy photo-peak in Figure 5.9 is a result of summation between the (121.8 keV + 1408.0 keV = 1529.8 keV) from the excited states of $^{152}$Sm.

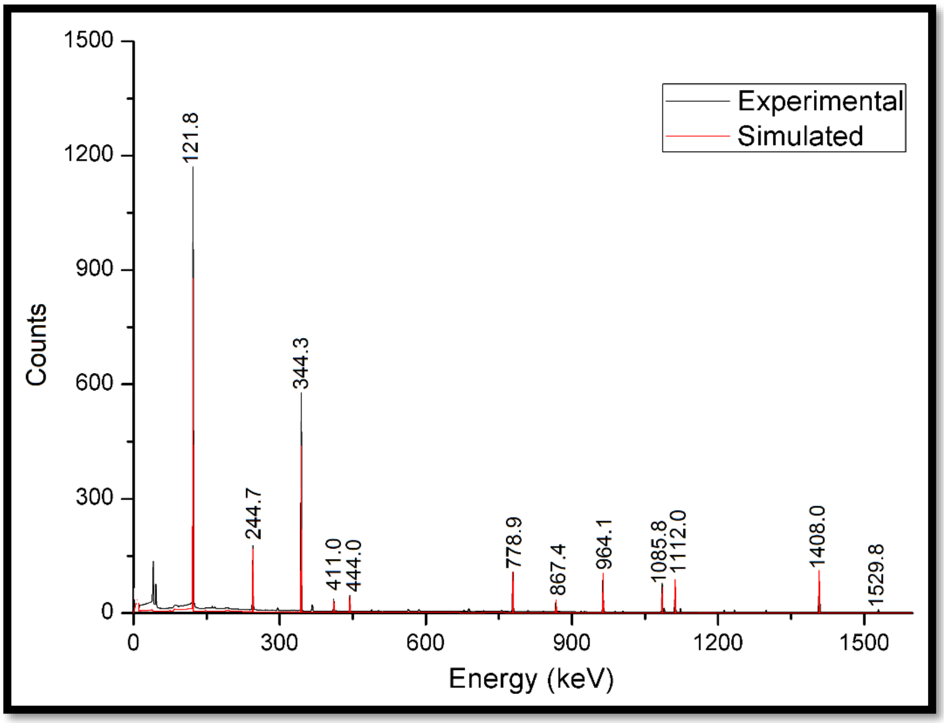

**Figure 5. 8:** The γ-ray spectra for the $^{152}$Eu point source (0 keV – 1600 keV).

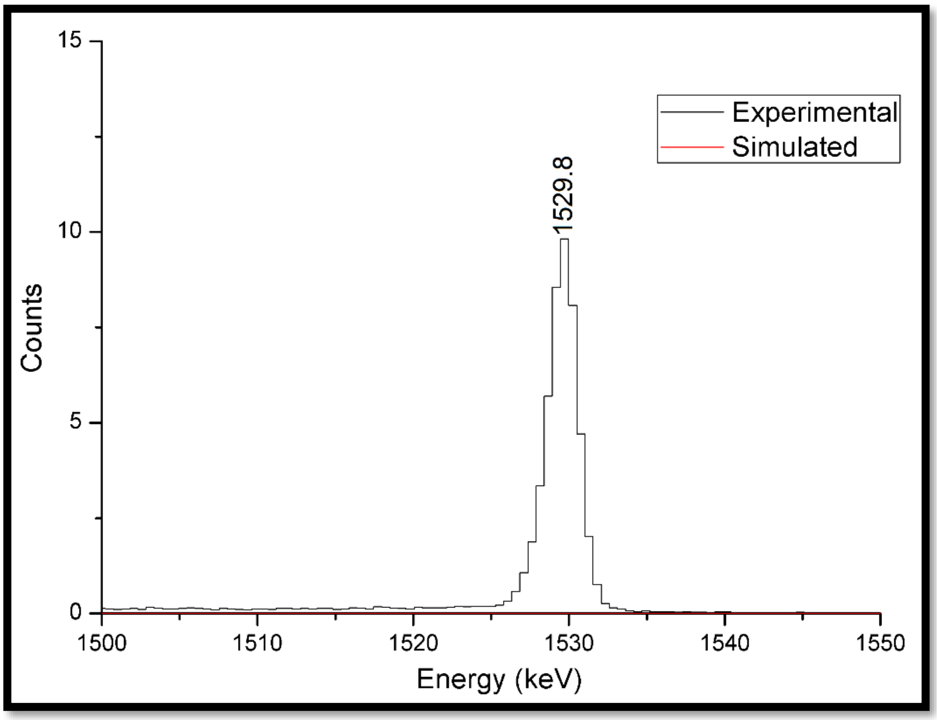

**Figure 5. 9:** The γ-ray spectra for the $^{152}$Eu point source (1500 keV – 1550 keV).

### 5.1.6 $^{241}$Am point source

Figure 5.10 presents the gamma-ray spectra for the $^{241}$Am point source for both the simulated and the experimental data. As listed in Table 5.1, a single gamma-ray with energy of about 60 keV is expected from the decay of $^{241}$Am, no summation effect is expected.

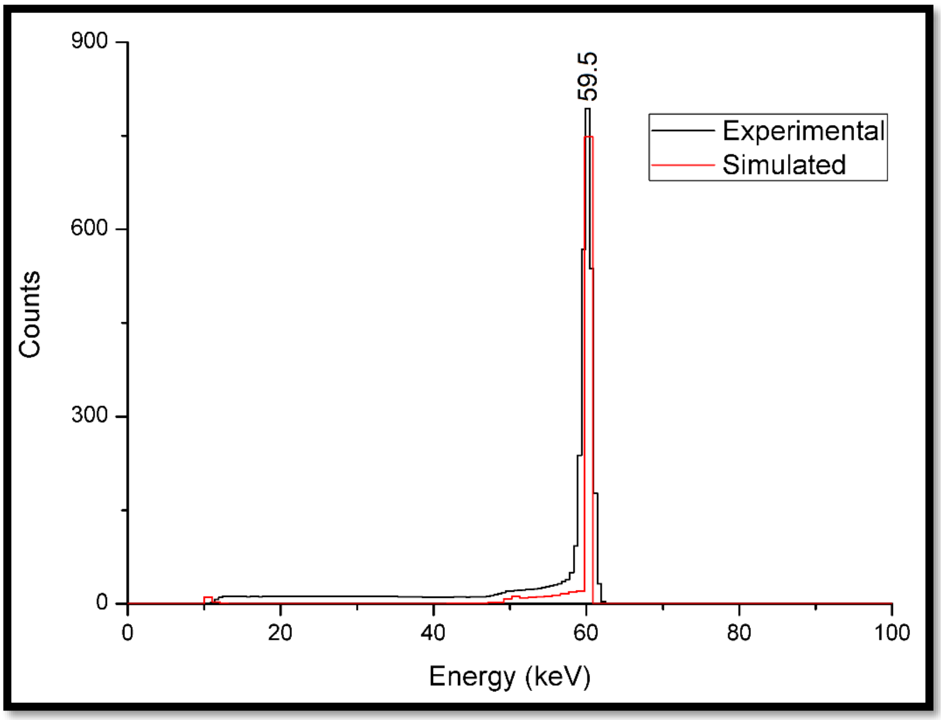

**Figure 5. 10:** The $\gamma$-ray spectra for the $^{241}$Am point source (0 keV -100 keV).

## 5.2 Volume source spectra (i.e. pill bottle (PB) and Marinelli beaker (MB))

Like the point sources discussed in section 5.1, volume sources (in pill bottle and Marinelli beaker) were also measured for 24 hours using the ERL HPGe detector. Following the similar trends, the simulated spectra were scaled up/down to match the intensities of the experimental spectra. The simulation matrices for sources were modelled from the information taken from the reference source certificates.

### 5.2.1 Thorium ore

Table 5.2 shows the gamma-ray emitting radionuclides in the $^{232}$Th-series, their energies and branching ratios. Only the gamma-ray energy lines with branching ratios greater than 1 % were selected and listed in Table 5.2.

**Table 5. 2:** Gamma-ray energy lines from $^{232}$Th decay series [Fir96; New08].

| Parent nuclide | Daughter nuclide | Energy (keV) | Gamma-ray emission probability branching ratio |
|---|---|---|---|
| $^{232}$Th | $^{228}$Ac | 209.3 | 0.039 |
| | | 270.2 | 0.035 |
| | | 338.3 | 0.113 |
| | | 463.0 | 0.044 |
| | | 794.9 | 0.043 |
| | | 911.2 | 0.266 |
| | | 969.0 | 0.162 |
| | | 1588.2 | 0.033 |
| | $^{212}$Pb | 238.6 | 0.436 |
| | $^{212}$Bi | 727.2 | 0.067 |
| | $^{208}$Tl | 510.8 | 0.081 |
| | | 583.2 | 0.304 |
| | | 860.6 | 0.040 |
| | | 2614.5 | 0.357 |

#### 5.2.1.1 Pill bottle geometry

In Figures 5.11 and 5.12, both the experimental and simulated spectra agree in terms of the shape and only vary in the intensities for each gamma-ray line observed. In Figure 5.13, the experimental spectrum shows the additional peaks that are not observed in the simulated spectrum. The summation peaks, as illustrated in Figure 5.13, are an indication of the possibility of coincidence summing. For example, the following photo-peaks, 2689.1 keV (688.1 keV + 2000.9 keV) from $^{228}$Ac and 3197.7 keV (583.2 keV + 2614.5 keV) from $^{208}$Tl are clearly observed.

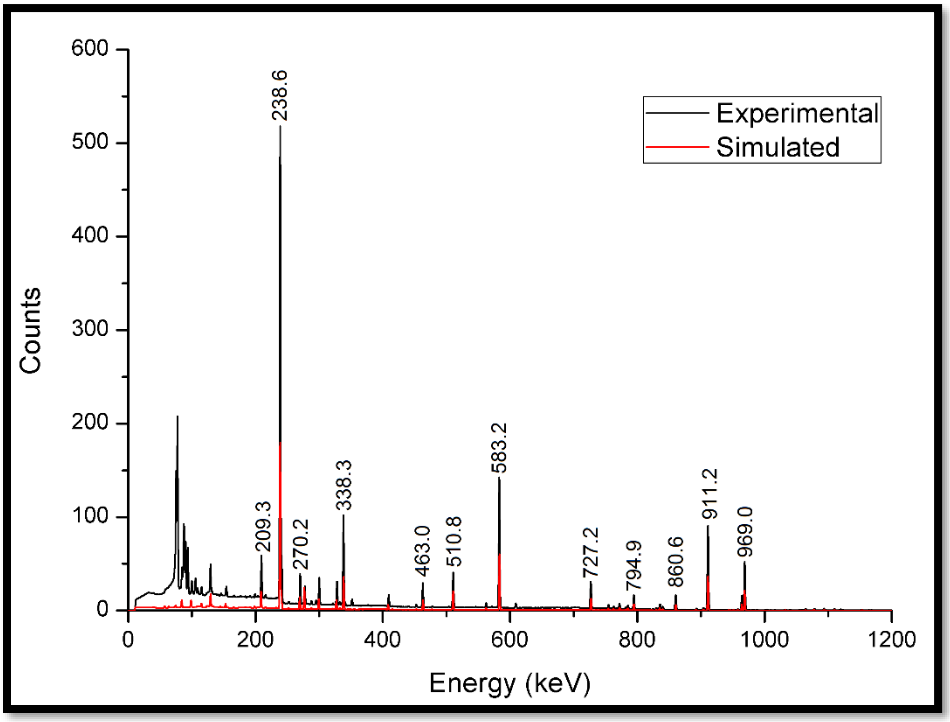

**Figure 5. 11:** The γ-ray spectra for the $^{232}$Th in PB geometry (0 keV – 1200 keV).

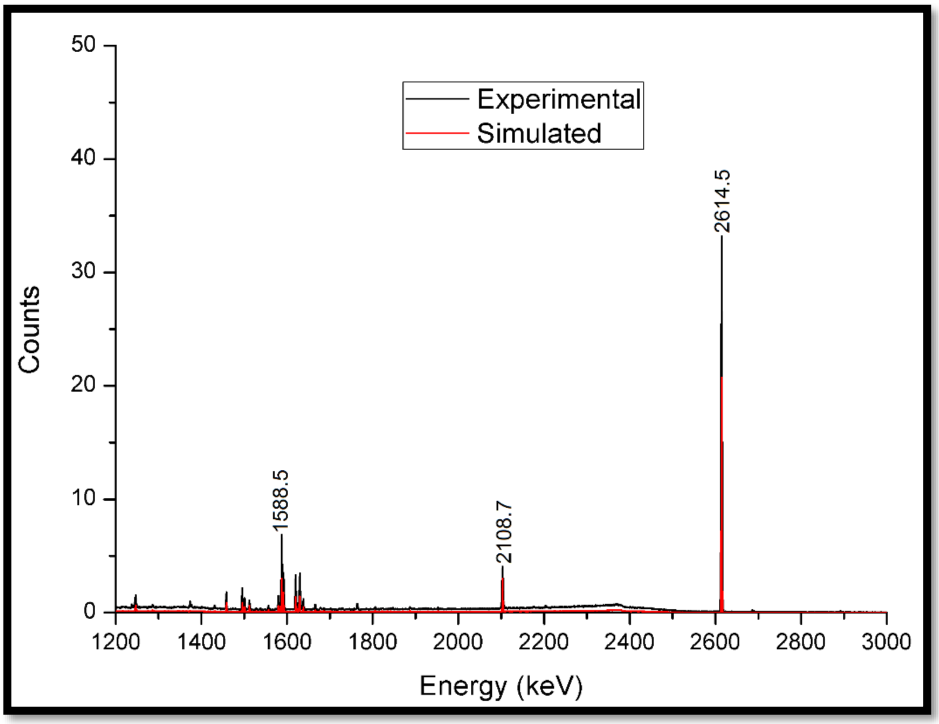

**Figure 5. 12:** The γ-ray spectra for the $^{232}$Th in PB geometry (1200 keV – 3000 keV).

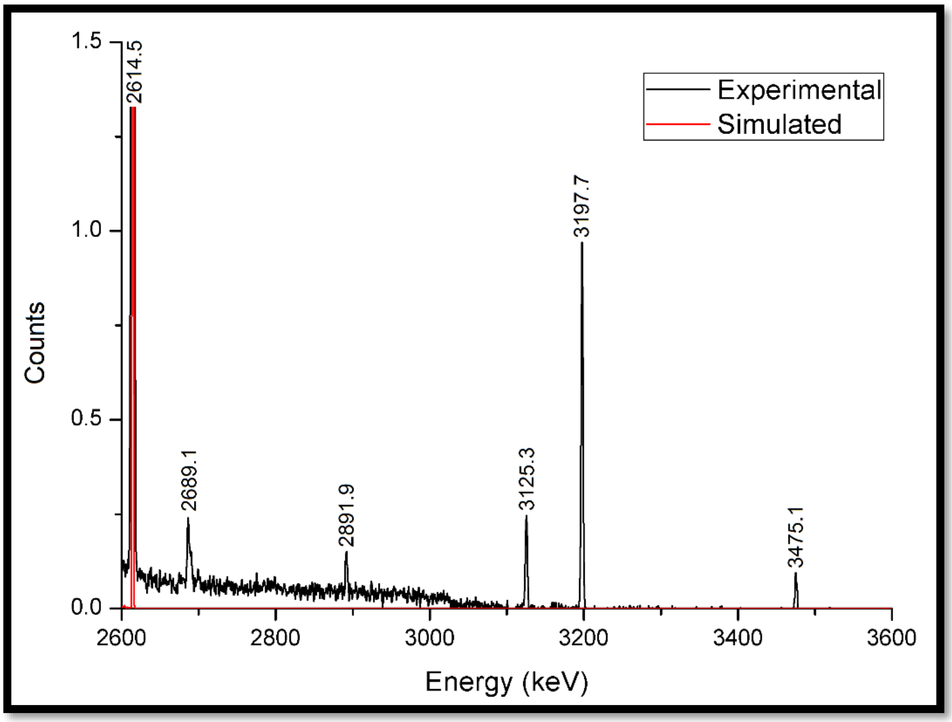

**Figure 5. 13:** The $\gamma$-ray spectra for the $^{232}$Th in PB geometry (2600 keV – 3600 keV).

### 5.2.1.2 Marinelli beaker geometry

The same observations that were observed in Figures 5.11, 5.12 and 5.13 (including the coincidence summing effect) were observed also in Thorium ore prepared for Marinelli beaker sample holder geometry. The only variation between sources prepared in pill bottle and Marinelli beaker geometry is in the spectrum count rates (intensities). In Figures 5.14 and 5.15, both the simulated and experimental spectra presented are showing a good agreement in terms of shape and varying intensities as expected. Also, Dam05 used the similar setup using Marinelli beaker at different volumes (the so-called volume effect).

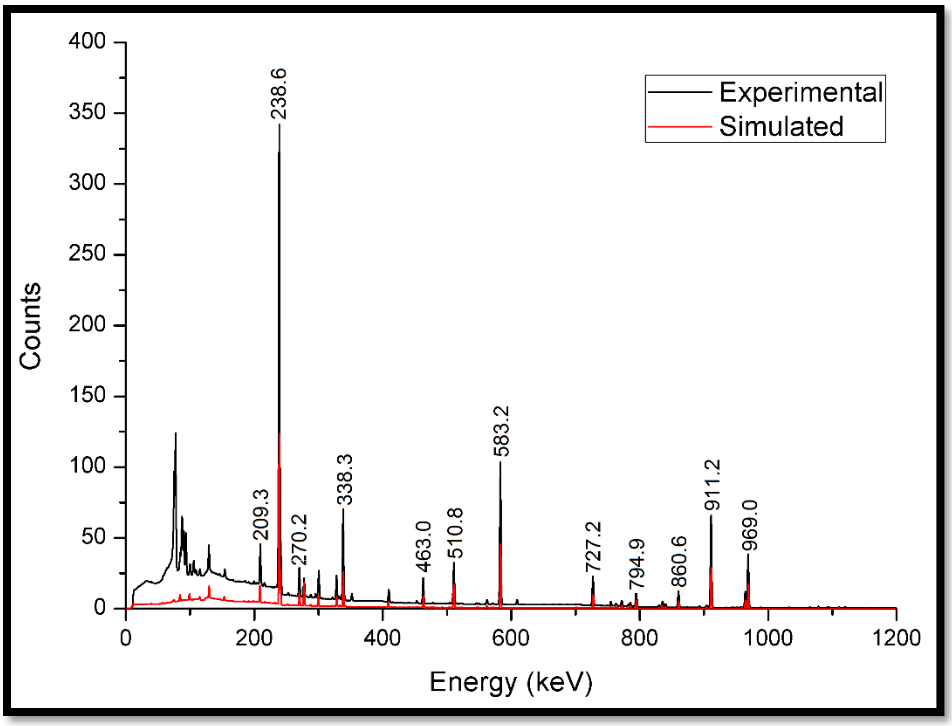

**Figure 5. 14:** The γ-ray spectra for the $^{232}$Th in MB geometry (0 keV – 1200 keV).

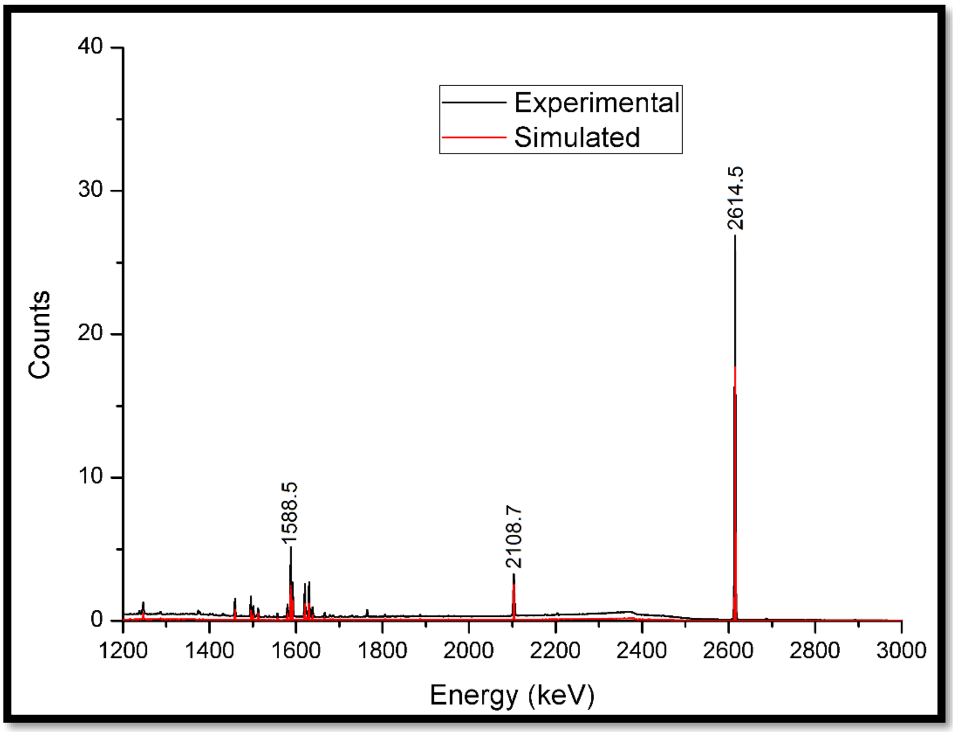

**Figure 5. 15:** The γ-ray spectra for the $^{232}$Th in MB geometry (1200 keV – 3000 keV).

### 5.2.2 Uranium ore

Table 5.3 shows the gamma-ray emitting radionuclides in the $^{238}$U-series, their energies and branching ratios. Only the gamma-ray energy lines with branching ratios greater than 1 % were selected and listed in Table 5.3.

**Table 5. 3:** Gamma-ray energy lines from $^{238}$U decay series [Fir96; New08].

| Parent nuclide | Daughter nuclide | Energy (keV) | Gamma-ray emission probability branching ratio |
|---|---|---|---|
| $^{238}$U | $^{234m}$Pa | 1001.0 | 0.008 |
| | $^{226}$Ra | 186.1 | 0.062 |
| | $^{214}$Pb | 241.9 | 0.075 |
| | | 295.2 | 0.185 |
| | | 351.99 | 0.358 |
| | $^{214}$Bi | 609.3 | 0.448 |
| | | 768.4 | 0.048 |
| | | 934.0 | 0.030 |
| | | 1120.4 | 0.148 |
| | | 1238.8 | 0.059 |
| | | 1377.6 | 0.039 |
| | | 1729.6 | 0.029 |
| | | 1764.6 | 0.154 |
| | | 2204.9 | 0.049 |

#### 5.2.2.1 Pill bottle geometry

In Figures 5.16 and 5.17, the simulated and experimental spectra of the gamma-ray emitting radionuclides in the $^{238}$U series are presented. As expected, the simulated spectrum agrees well with the experimental data in terms of shape and only varies in intensity for photo-peak to photo-peak comparison. Also note that in the experimental spectrum some additional peaks are clearly visible, and some are not due to the summing effect, but from those with lower branching ratios. In Figure 5.18, the photo-peaks that resulted from the summation effects are shown.

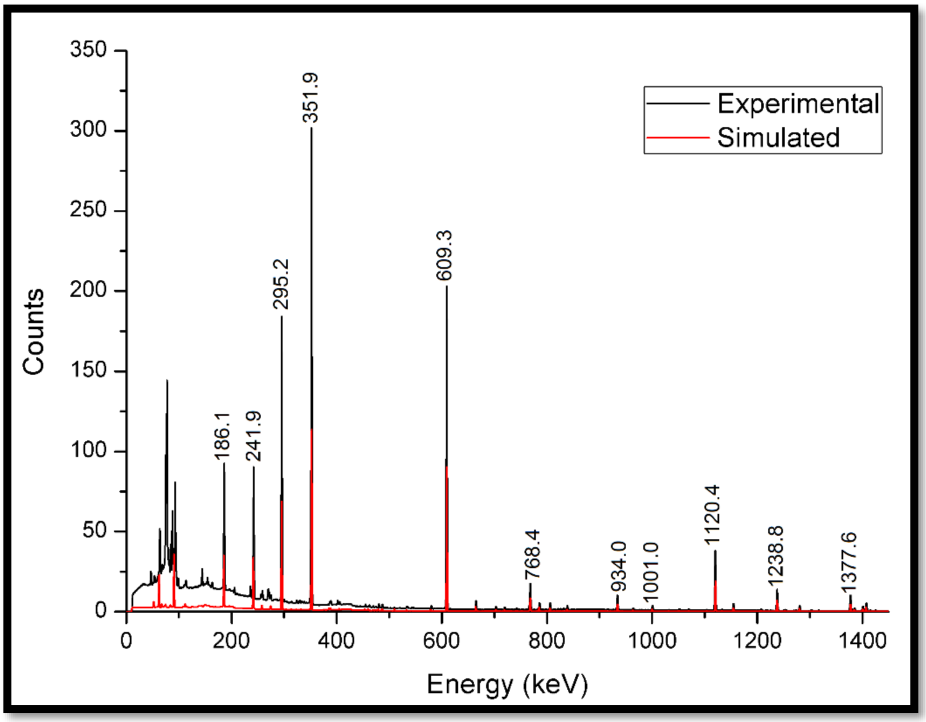

**Figure 5. 16:** The γ-ray spectra for the $^{238}$U in PB geometry (0 keV – 1450 keV).

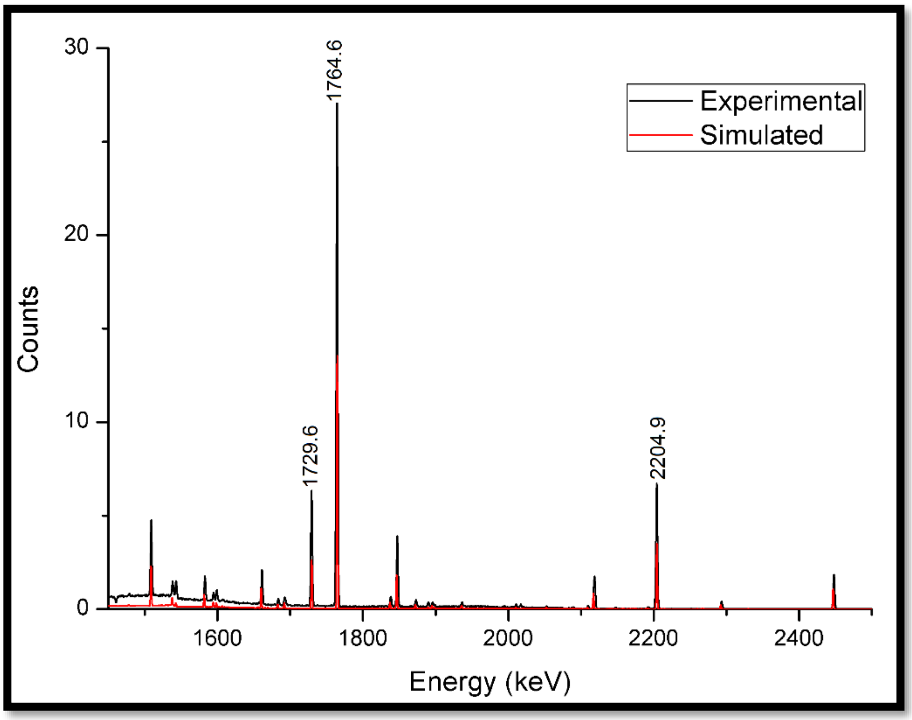

**Figure 5. 17:** The γ-ray spectra for the $^{238}$U in PB geometry (1450 keV – 2500 keV).

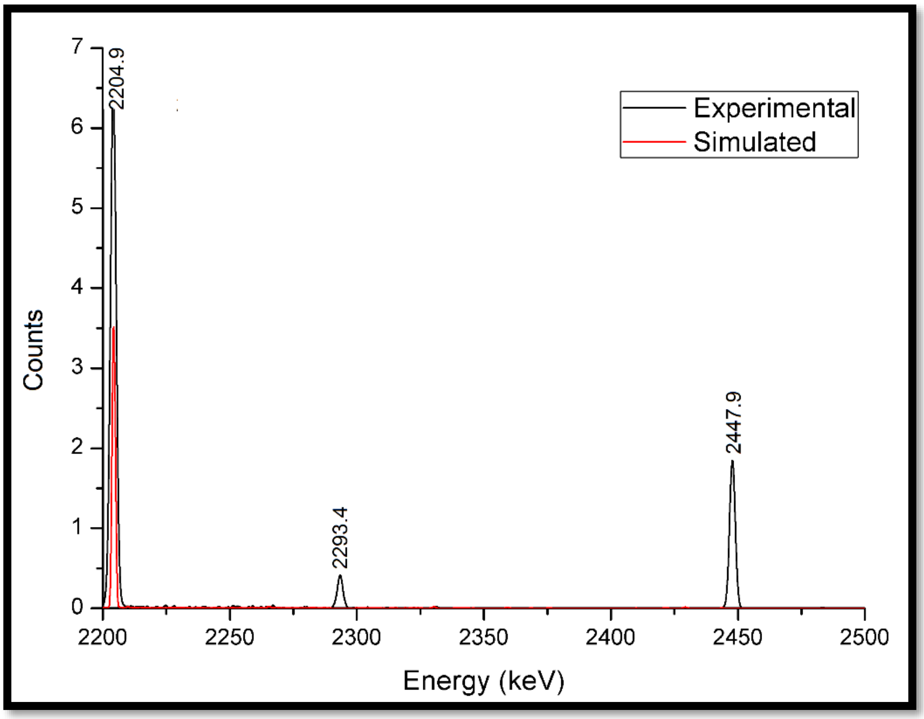

**Figure 5. 18:** The γ-ray spectra for the $^{238}U$ in PB geometry (2200 keV – 2500 keV).

### 5.2.2.2 Marinelli beaker geometry

In Figures 5.19 and 5.20, the same observations that were observed in Figures 5.16 and 5.17 were also observed also from the Uranium ore prepared for Marinelli beaker sample holder geometry. The only difference was in the volume or geometry that resulted from the variation between the spectra count rates.

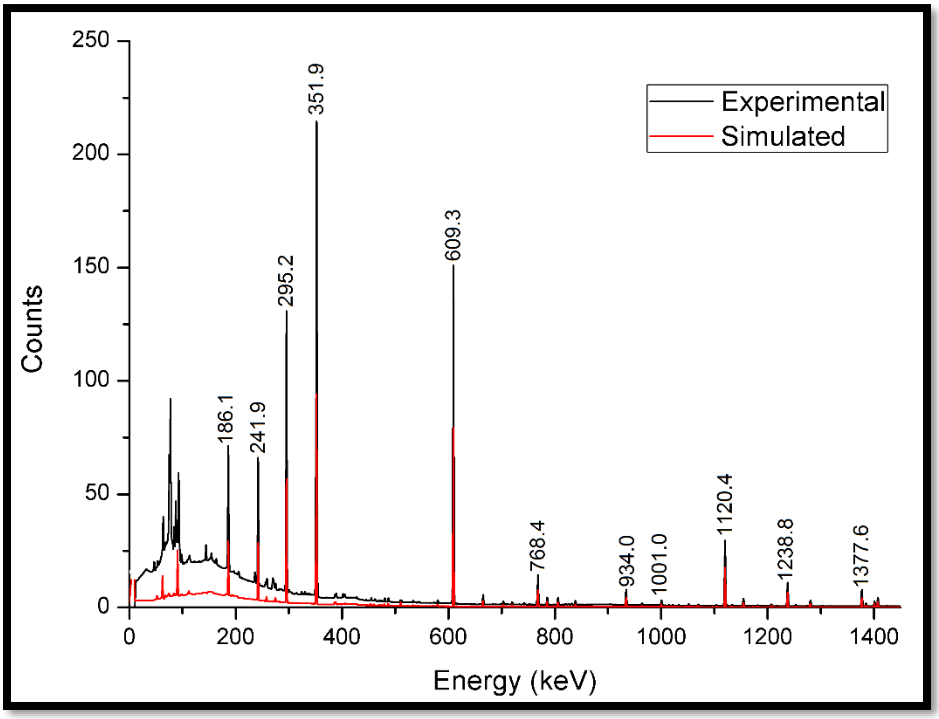

**Figure 5. 19:** The γ-ray spectra for the $^{238}$U in MB geometry (0 keV – 1450 keV).

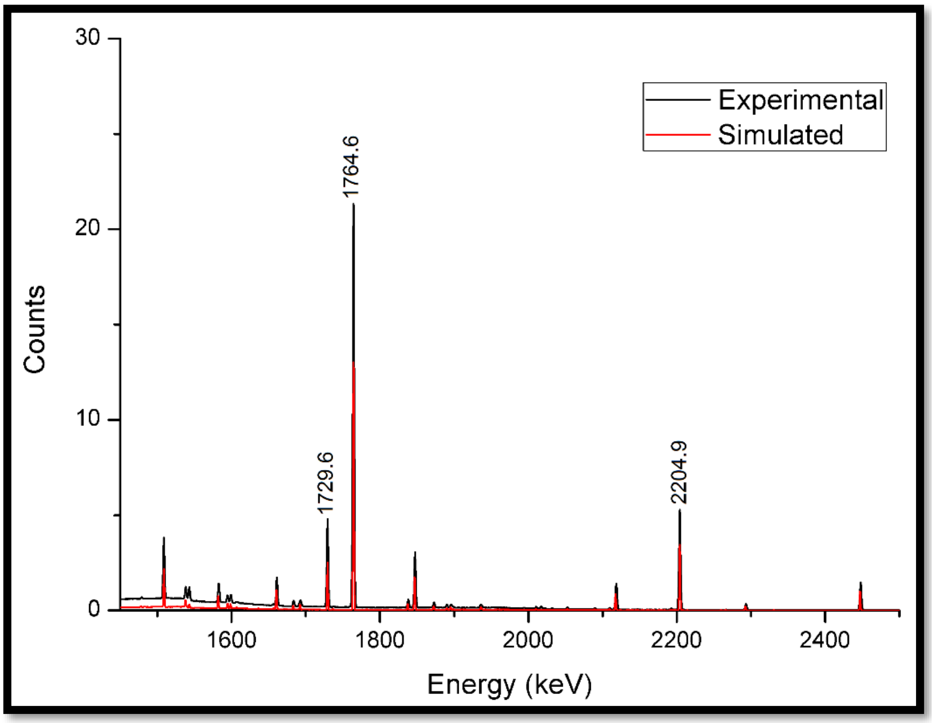

**Figure 5. 20:** The γ-ray spectra for the $^{238}$U in MB geometry (1450 keV – 2500 keV).

## 5.2.3 Potassium Sulphate

For the volume sources prepared using the Potassium Sulphate ($K_2SO_4$), only a single gamma-ray line is expected at about 1461 keV from the decay of $^{40}$K. For this radionuclide, $^{40}$K, there is no summing effect expected. In Figures 5.21, 5.22 and 5.23 are the simulated and experimental spectra are presented for the pill-bottle and Marinelli beaker geometries, respectively. In general, the experimental data from $^{40}$K can also be used to correct the experimental data from the $^{232}$Th and $^{238}$U series, which experience coincidence summing.

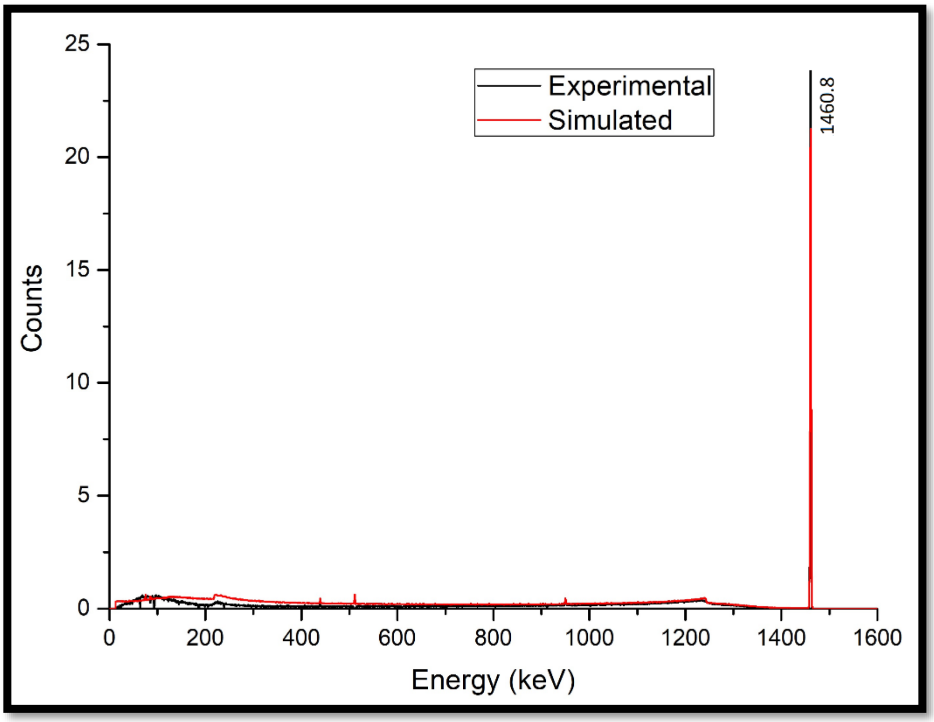

**Figure 5. 21:** The γ-ray energy spectra for the $K_2SO_4$ source in a PB (0 keV – 1600 keV).

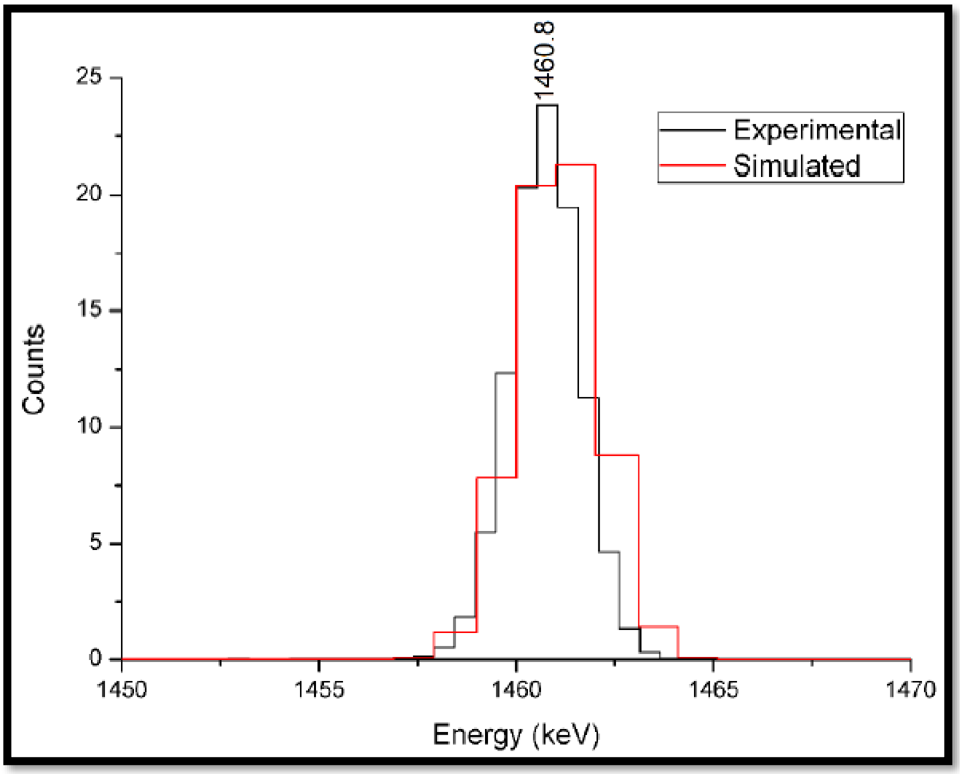

**Figure 5. 22:** The γ-ray energy spectra for the $K_2SO_4$ source in a PB (1450 keV – 1470 keV).

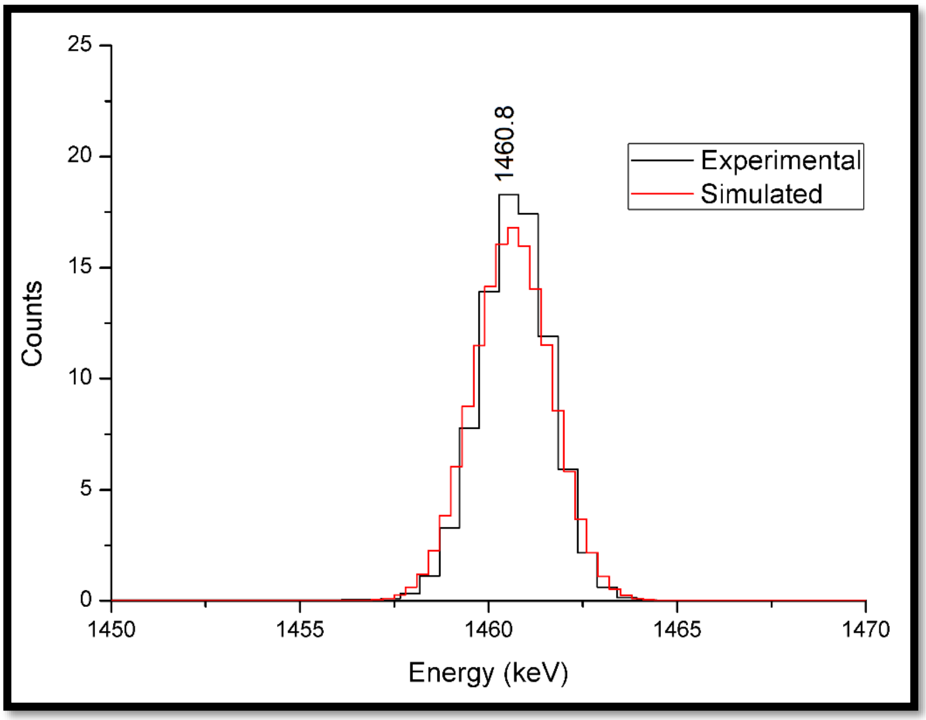

**Figure 5. 23:** The γ-ray energy spectra for the $K_2SO_4$ source in a MB (1450 keV – 1470 keV).

### 5.2.4 IAEA – 375 Soil sample

The IAEA-375 reference soil sample is also available in 1 L Marinelli beaker with about 10 radionuclides listed as indicated in Table A.5. These radionuclides have varying activity concentrations as recorded in the certificate. Note also in Table A.5 is that $^{137}$Cs has the highest activity concentration (5280 ± 91 Bq/kg) as compared to other radionuclides in the mixture. Figure 5.24 shows the experimental spectrum of soil sample with the 661.7 keV energy from $^{137}$Cs being the dominant photo-peak. Figure 5.25 shows a plot of the gamma-ray energy spectra for both experimental and simulated data around the 661.7 keV ($^{137}$Cs) region.

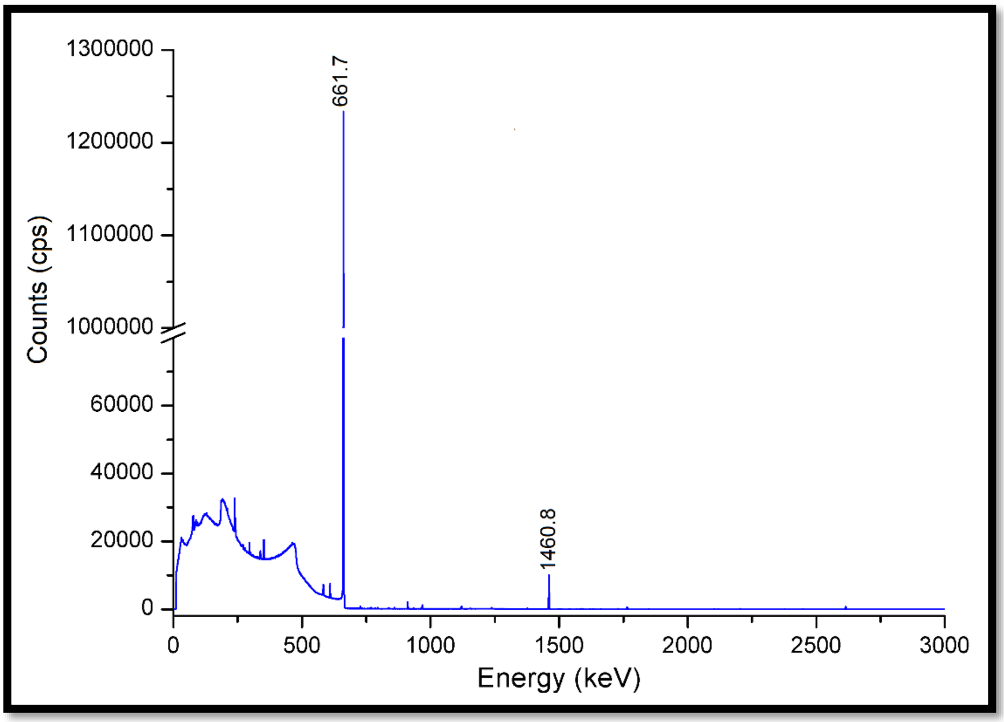

**Figure 5. 24:** The γ-ray energy spectra for the soil source for experimental data (0 keV - 3000 keV).

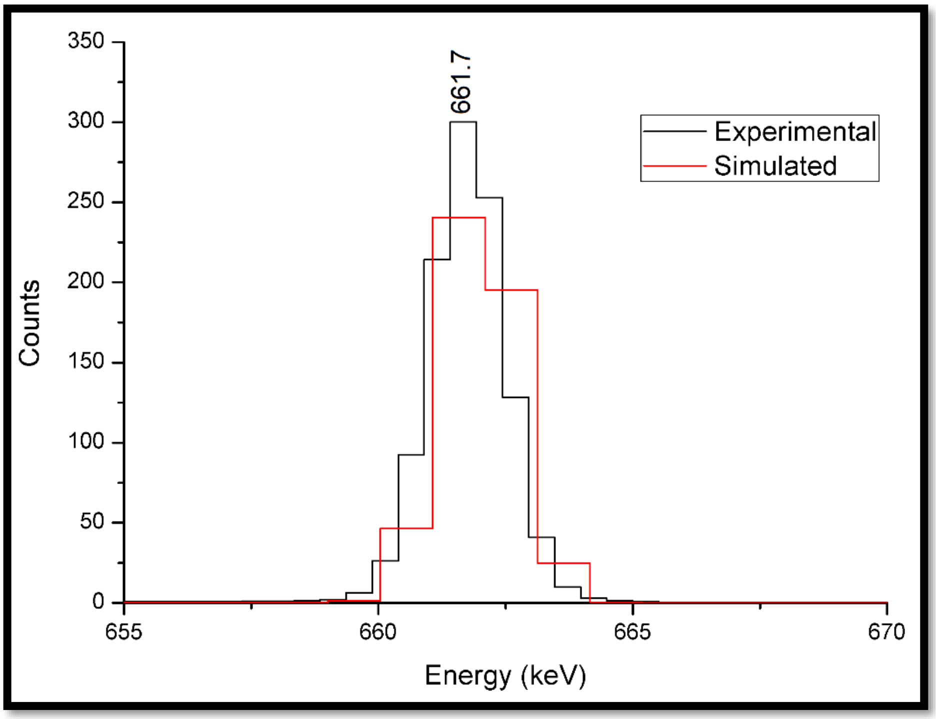

**Figure 5. 25:** The γ-ray energy spectra for the soil source (655 keV – 670 keV).

### 5.2.5 Liquid source

In addition to the volume sources using the ore materials, the ERL also acquired a certified reference source in a liquid form prepared in a Marinelli beaker. This standard source contains a cocktail of radionuclides, $^{60}$Co, $^{137}$Cs and $^{152}$Eu (see also Table A.4 for the details). The decay correction was done in the activity for each nuclide corrected since preparation time of the liquid source as recorded. For simulation results, the matrix was modelled for the values taken from the source certificate.

Figure 5.26 shows the gamma-ray energy spectra of the liquid source in (a) spectrum from simulated and (b) spectrum from experimental data. The gamma-ray energy lines of the radionuclides were corrected and normalised based on their activities (Bq). As expected, for the gamma-ray lines coming from the same radionuclide ($^{152}$Eu for example, refer also to Figure 5.9) will show summation effect in the experimental spectrum, which is not visible in the simulated spectrum. Figure 5.27 shows the experimental and simulation spectra plotted on the same axis.

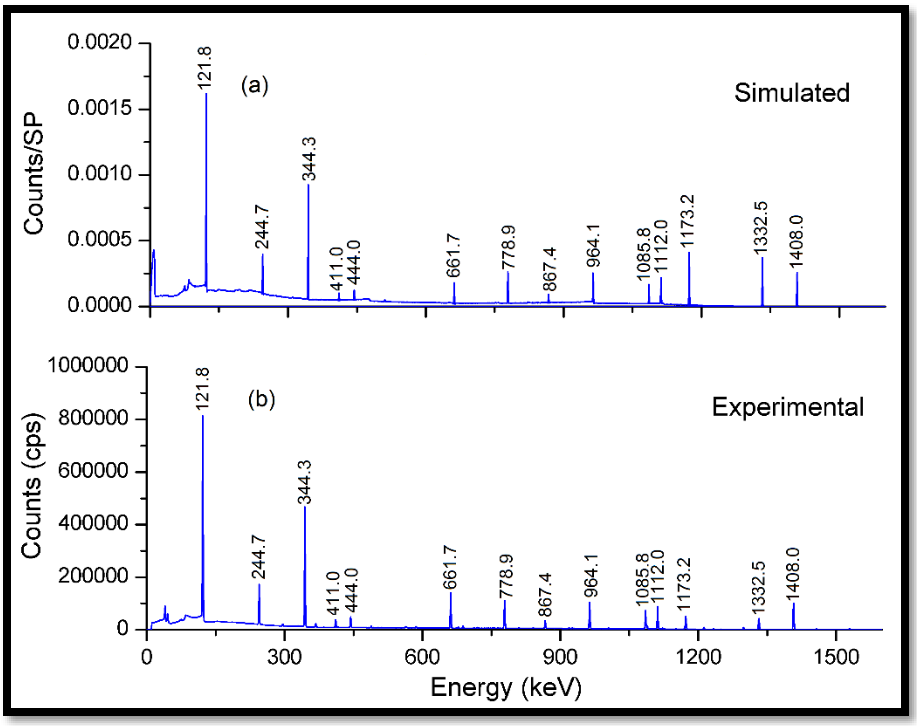

**Figure 5. 26:** The γ-ray energy spectra for the liquid source for; (a) simulated data (b) experimental data (0 keV – 1600 keV).

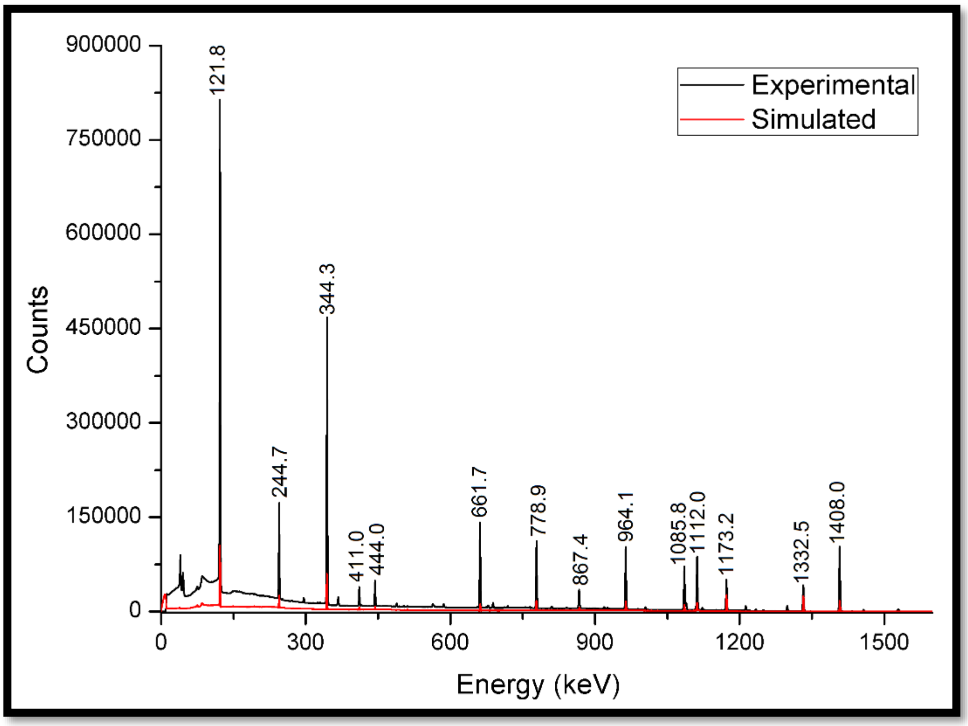

**Figure 5. 27:** The γ-ray energy spectra for the liquid source (0 keV – 1600 keV).

## 5.3 Efficiency calibration

As discussed in section 2.6, the full-energy peak efficiency of the detector is of interest in this study. Also, of interest for this study is to optimise the simulation efficiency values against the experimental data. The following volume sources, pill bottle and Marinelli beaker geometry are dependent on the full energy peak efficiency, which will be presented and discussed in the next subsections. To determine the full-energy peak efficiency, the windows analysis was used and the ATOMKI Palmtop software was used to fit energy peaks used to determine efficiency data. The full-energy peak efficiency data determined from the known sources, was fitted with a power fit function as follows:

$$\varepsilon = aE^b \tag{5.1}$$

where $E = E_\gamma / E_0$; $E_\gamma$ (keV) being the gamma-ray energy, $E_0$ = 1 keV, a and b being fit parameters which are dimensionless. Here a > 0, b < 0 so that the dimensionless efficiency, ε, decreases with the increasing energy E [Deb88].

To get the full energy peak efficiency in equation 3.2 (repeated here as equation 5.2), the background subtracted net (Counts) will be divided by the branching ratio ($B_r$) and activity concentration ($A_c$) mass (m) and time (t).

$$\varepsilon = \frac{Counts}{A_c * B_r * t * m} \tag{5.2}$$

For all the parameters in equation 5.2 for the efficiency calculations, both the mass and time were not included in the uncertainty determination of the efficiency. Therefore, the uncertainty in the efficiency value was determined as follows

$$\Delta\varepsilon = \varepsilon\sqrt{\left(\frac{\Delta Counts}{Counts}\right)^2 + \left(\frac{\Delta B_r}{B_r}\right)^2 + \left(\frac{\Delta A_c}{A_c}\right)^2} \tag{5.3}$$

The efficiency uncertainties in equation 5.1 include the uncertainty in parameters a and b as follows:

$$\Delta\varepsilon^2 = \left(\frac{\partial\varepsilon}{\partial a}\right)^2 \Delta a^2 + \left(\frac{\partial\varepsilon}{\partial b}\right)^2 \Delta b^2 \tag{5.4}$$

Equation 5.4 reduces to:

$$\Delta\varepsilon = \varepsilon\sqrt{(E^b)^2\,\Delta a^2 + \,[E^b(\ln E)a]^2\Delta b^2} \tag{5.5}$$

### 5.3.1 Pill bottle geometry

Full energy peak efficiencies obtained for the pill bottle sample geometry using the gamma-ray energy lines of interest (Uranium and Thorium ores, as well as $K_2SO_4$) are listed in Table 5.4. In Table 5.4, a combination of gamma-ray lines from the $^{238}$U series (refer to Table 5.3), $^{232}$Th series (Table 5.2) and $^{40}$K line at ~1461 keV are used. The data in Table 5.4 shows the experimental determined full energy peak efficiencies and uncertainties (column 2). The normalised experimental efficiency values and uncertainties (column 3), simulated efficiency value and uncertainties (column 4) as well as the corrected simulated efficiency value (column 5) as a function of energies, are also given. The "normalised efficiency" refers to the experimental efficiency data points of the $^{232}$Th and $^{238}$U that were scaled up/down to the experimental data point using the $^{40}$K as point of reference, whereas, the "corrected efficiency" refers to simulated efficiency values scaled to be aligned with the normalised experimental efficiency values.

For the normalised values in column 3, the experimentally determined values for the $^{238}$U series and $^{232}$Th series are normalised based on the $^{40}$K value, i.e. the power fit value at 1461 keV (for both Uranium and Thorium sources) should correspond to the value from the $K_2SO_4$ source. These values are then compared with the simulation data (column 4) and adjusted further to obtain the corrected simulation values (column 5).

Moreover, the data presented in table 5.4 are also plotted in Figures 5.28 and 5.29 as indicated for various settings.

**Table 5. 4:** Table showing gamma-ray energies, experimental and simulated efficiencies from PB.

| Energy (keV) | Experimental Efficiency | Normalised Experimental Efficiency | Simulation Efficiency | Corrected Simulation Efficiency |
|---|---|---|---|---|
| 186.1 | 0.0517 ± 0.0004 | 0.0510 ± 0.0004 | 0.0339 ± 0.0020 | 0.0477 |
| 295.2 | 0.0369 ± 0.0004 | 0.0364 ± 0.0004 | 0.0251 ± 0.0014 | 0.0354 |
| 352.0 | 0.0328 ± 0.0003 | 0.0324 ± 0.0003 | 0.0224 ± 0.0011 | 0.0315 |
| 1001.0 | 0.0154 ± 0.0007 | 0.0152 ± 0.0007 | 0.0113 ± 0.010 | 0.0160 |
| 1238.8 | 0.0112 ± 0.0001 | 0.0111 ± 0.0001 | 0.0099 ± 0.0044 | 0.0139 |
| 1377.6 | 0.0127 ± 0.0002 | 0.0125 ± 0.0002 | 0.0092 ± 0.0056 | 0.0130 |
| 2204.9 | 0.0082 ± 0.0002 | 0.0081 ± 0.0002 | 0.0068 ± 0.0062 | 0.0096 |
| 238.6 | 0.0398 ± 0.0008 | 0.0427± 0.0009 | 0.0288 ± 0.0010 | 0.0406 |
| 338.3 | 0.0315 ± 0.0006 | 0.0338± 0.0007 | 0.0230 ± 0.0022 | 0.0324 |
| 860.6 | 0.0148 ± 0.0004 | 0.0159 ± 0.0004 | 0.0125 ± 0.0054 | 0.0176 |
| 911.2 | 0.0154 ± 0.0003 | 0.0165± 0.0003 | 0.0121 ± 0.0021 | 0.0170 |
| 969.0 | 0.0139 ± 0.0002 | 0.0149 ± 0.0003 | 0.0116 ± 0.0028 | 0.0163 |
| 1460.8 | 0.0111 ± 0.0002 | 0.0111± 0.0002 | 0.0089 ± 0.0022 | 0.0125 |

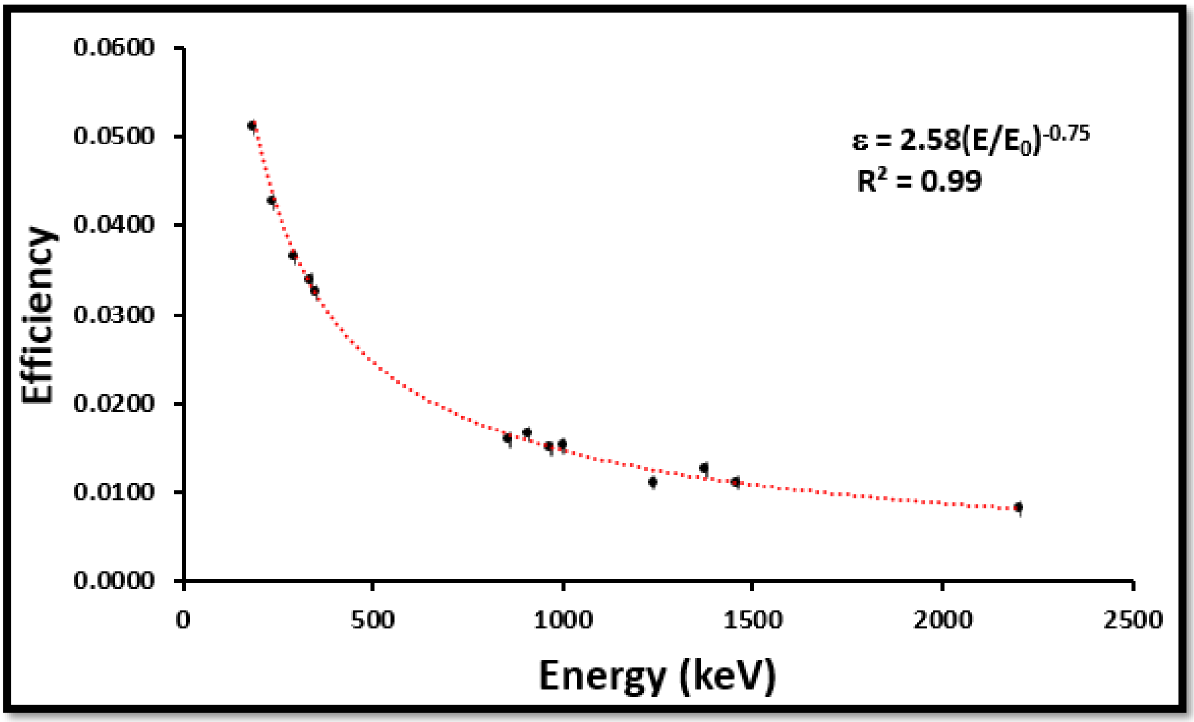

**Figure 5. 28:** Normalised experimental efficiency curve for PB sample holder geometry with power fit function parameters shown.

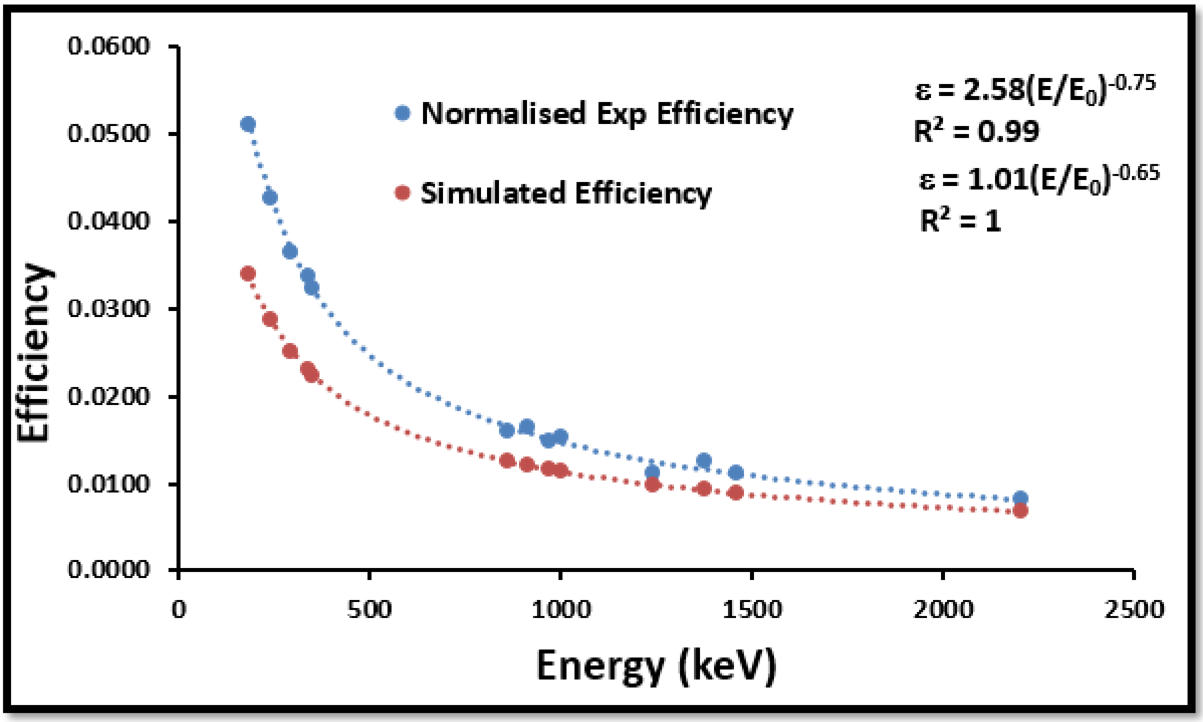

**Figure 5. 29:** Normalised experimental and simulated efficiency curves plotted on the same set of axes for PB with power fit function parameters shown.

### 5.3.2 Marinelli beaker geometry

As was explained for the pill bottle geometry (see section 5.3.1), full energy peak efficiency was also obtained the same way for the Marinelli beaker geometry. The values used to plot efficiency curves (Figures 5.30 and 5.31) are presented in table 5.5. The procedure for Marinelli beaker samples is like the one discussed above in subsection 5.3.1 (pill bottle geometry). In Figure 5.29 the experimental curve lies above the simulated curve while in Figure 5.20 the experimental curve lies above the simulated curve, this is due to the sample geometry used in these Figures. This study is also like the study done by Dam05, where absolute efficiency curves were compared for the natural gamma energies at different volume in the Marinelli beaker. $^{40}$K gamma-ray energy line was used to set the photopeak efficiency on an absolute scale [Dam05].

**Table 5. 5:** Table showing gamma-ray energies, experimental and simulated efficiencies from MB geometry.

| Energy (keV) | Experimental Efficiency | Normalised Experimental Efficiency | Simulation Efficiency | Corrected Simulation Efficiency |
|---|---|---|---|---|
| 186.1 | 0.0361 ± 0.0017 | 0.0384 ± 0.0016 | 0.0516 ± 0.0024 | 0.0382 |
| 295.2 | 0.0271 ± 0.0003 | 0.0288 ± 0.0003 | 0.0381 ± 0.0017 | 0.0282 |
| 352.0 | 0.0243 ± 0.0002 | 0.0258 ± 0.0002 | 0.0340 ± 0.0013 | 0.0251 |
| 1001.0 | 0.0109 ± 0.0002 | 0.0115 ± 0.0002 | 0.0171 ± 0.0111 | 0.0126 |
| 1238.8 | 0.0087 ± 0.0001 | 0.0093 ± 0.0001 | 0.0148 ± 0.0049 | 0.0110 |
| 1377.6 | 0.0093 ± 0.0001 | 0.0098 ± 0.0001 | 0.0138 ± 0.0062 | 0.0102 |
| 2204.9 | 0.0065 ± 0.0002 | 0.0069 ± 0.0001 | 0.0102 ± 0.0067 | 0.0075 |
| 238.6 | 0.0354 ± 0.0008 | 0.0407 ± 0.0009 | 0.0438 ± 0.0011 | 0.0324 |
| 338.3 | 0.0236 ± 0.0005 | 0.0271 ± 0.0005 | 0.0348 ± 0.0025 | 0.0258 |
| 860.6 | 0.0122 ± 0.0003 | 0.0140 ± 0.0003 | 0.0189 ± 0.0059 | 0.0140 |
| 911.2 | 0.0123 ± 0.0003 | 0.0142 ± 0.0003 | 0.0182 ± 0.0024 | 0.0134 |
| 969.0 | 0.0101 ± 0.0002 | 0.0116 ± 0.0002 | 0.0174 ± 0.0031 | 0.0129 |
| 1460.8 | 0.0090 ± 0.0001 | 0.0090 ± 0.0001 | 0.0133 ± 0.0022 | 0.0098 |

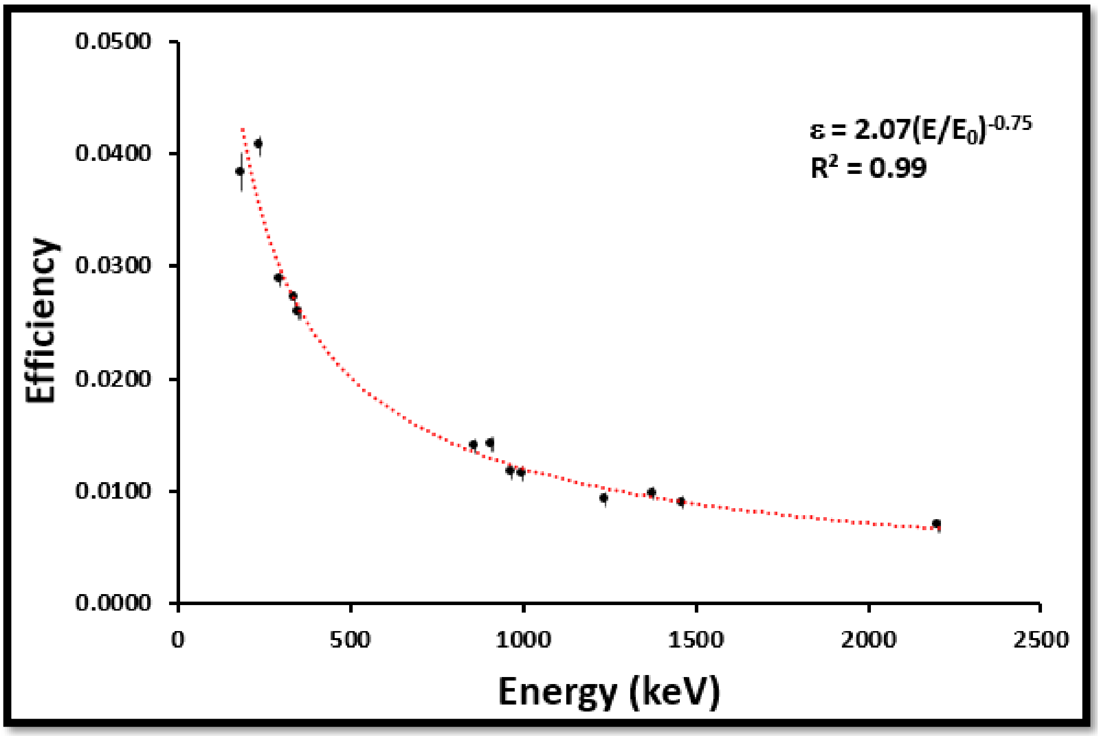

**Figure 5. 30:** Normalised experimental efficiency curve for MB sample holder geometry with power fit function parameters shown.

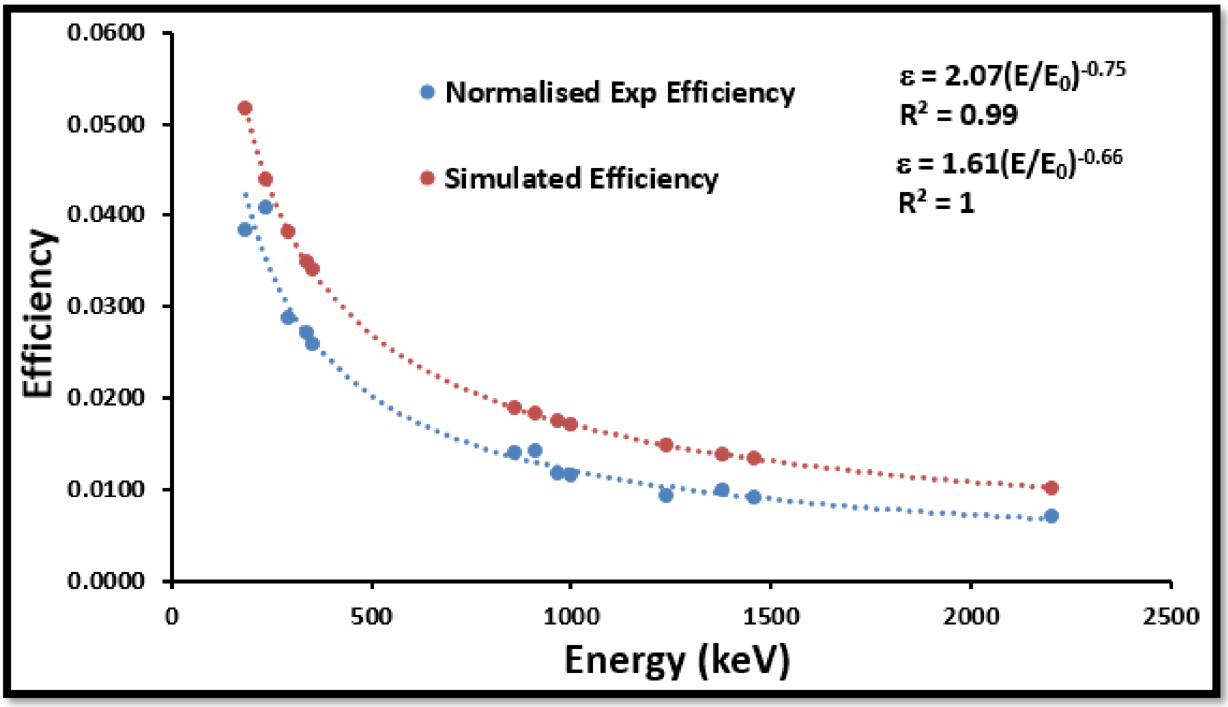

**Figure 5. 31:** Normalised experimental and simulated efficiency curves plotted on the same set of axes for MB with power fit function parameter shown.

### 5.3.3 Density effect

Full-energy peak efficiency values are also affected by the self-absorption within the sample. This effect is more pronounced in volume sources. To investigate this effect, MC simulations of typical sand represented as silicon dioxide ($SiO_2$) material, was modelled with varying density values. Random gamma-ray energies ranging from 120 keV up to 3000 keV were used. The assumption was that all these gamma-ray energy lines have the same branching ratio. In the lower density at 1.0 g.cm$^{-3}$ (corresponding to water density) and to the higher density at 3 g.cm$^{-3}$ (for heavy mineral samples).

In Figures 5.32 and 5.33, the detection efficiency as a function of density is shown for various energy values. The efficiency values decrease with increasing density. Moreover, and as expected, the efficiency values are high at low energies and lower at high energy values.

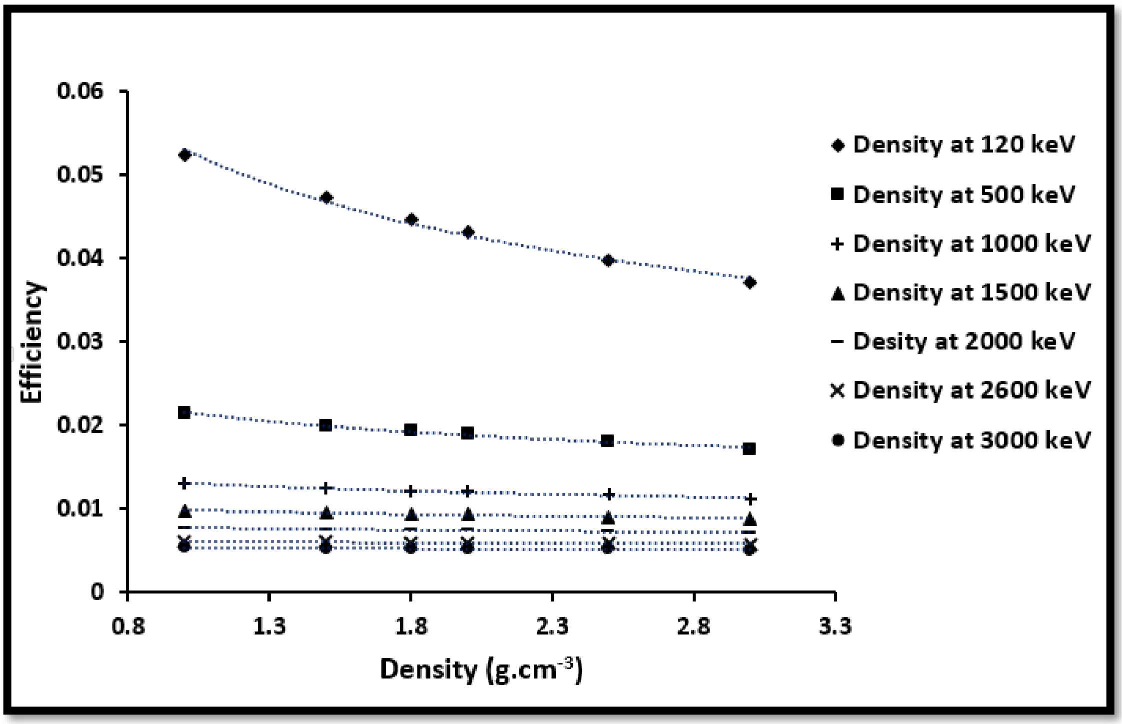

**Figure 5. 32:** Efficiency curves at different densities for the PB sample geometry.

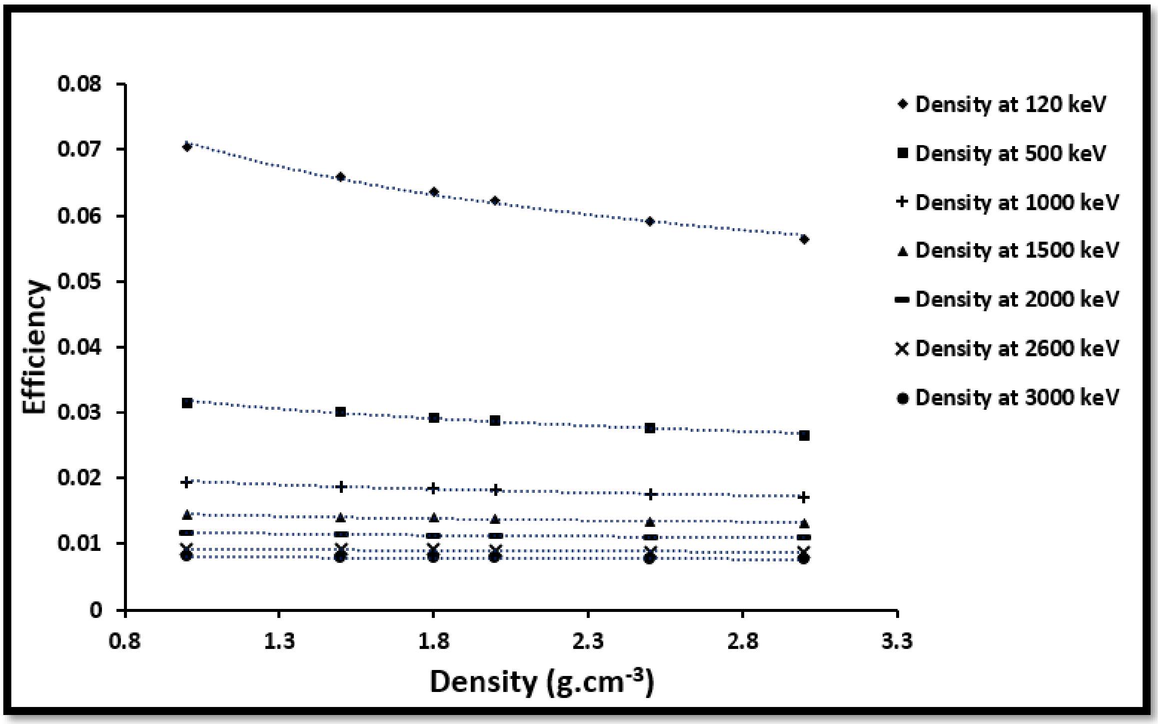

**Figure 5. 33:** Efficiency curves at different densities for the MB sample geometry.

# Chapter 6: Summary and Conclusion

The purpose of this study was to optimise the available HPGe gamma-ray detector that is used at iThemba LABS for efficiency calibration of various sample geometries. The exercise was carried out using both experimentally determined data and Monte Carlo simulations.

The experiments were done with certified reference sources with known activity concentrations. This available information was then used to determine the full-energy peak efficiency values of the iThemba LABS HPGe detector system, subsequently the fit parameters for the pill bottle (100 mL) and Marinelli Beaker (1 L) counting geometry. Both point sources and "bulk" (a cylindrical 100 mL pill bottle and a 1 L Marinelli beaker) sources were used. Measured and calculated efficiency values were determined by series of experiments and MC simulations (MCNPX code). From Figures 5.28 to 5.31; the full energy peak efficiency of the detector as a function of energy generated from the experimental data, the simulated data, as well as the correction of the two methods, were presented. In the comparison, as shown in Figure 5.29, it has been observed that the measured efficiency curve is higher than the calculated one for the pill bottle geometry, whereas in Figure 5.31 the measured efficiency curve is lower than the calculated one for the Marinelli beaker geometry. Moreover, Figures 5.32 and 5.33 show the simulated efficiency functions with various densities. Efficiency calibration parameters (power fit function) for the volume sources were determined from experimental and simulated data; $a = 2.58$; $b = -0.75$ experiment and $a = 1.01$; $b = 0.65$ simulated (100 mL pill bottle) and $a = 2.07$; $b = -0.75$ experiment and $a = 1.61$; $b = 0.66$ simulated (1 L Marinelli beaker).

Experimental data were also compared with the simulated data and were found to be in good agreement. The simulated data were used to correct the effect of coincidence summing in the experimental data for full energy peak efficiency. This was clearly observed in experimental spectra data for some of the photo-peaks showing the effects of coincidence summing, while no effect was observed in simulated spectra data. In simulations, each particle is tracked individually in a given time. The simulated corrected parameters for the efficiency as determined can be used for future calculations of activity concentrations when the 100 mL pill bottle or 1 L Marinelli Beaker sample holder is used. Note also that to improve the accuracy in these calculations, sample density should be considered.

Additionally, the simulation input files used to generate these efficiencies is available and can be modified to match any sample holder geometry, as well as any density that might be required in future counting.

# Appendix A

**Standard reference material tables of certification**

**Table A. 1:** Uranium reference source, IAEA/RGU-1 [Pre87].

| Component | Concentration | Confidence Interval | Reference year |
|---|---|---|---|
| Uranium | 400 μg/g | ± 2 μg/g | 1987 |
| Thorium | Less than 1 μg/g | | |
| Potassium | Less than 20 μg/g | | |

**Table A. 2:** Thorium reference source, IAEA/RGTh-1 [Pre87].

| Component | Concentration | Confidence Interval | Reference Year |
|---|---|---|---|
| Thorium | 800 μg/g | ± 16 μg/g | 1987 |
| Uranium | 6.3 μg/g | ± 0.4 μg/g | |
| Potassium | 0.02 % | ± 0.01 % | |

**Table A. 3:** Potassium Sulphate reference source, IAEA/RGK-1 [Pre87].

| Component | Concentration | Confidence Interval | Reference year |
|---|---|---|---|
| Potassium | 44.8 % | ± 0.3 % | 1987 |
| Uranium | Less than 0.001 μg/g | | |
| Thorium | Less than 0.01 μg/g | | |

**Table A. 4:** Liquid source with $^{152}$Eu, $^{137}$Cs and $^{60}$Co radionuclides [Csi02].

| Radionuclide | Activity | Uncertainty (1σ) | Reference date |
|---|---|---|---|
| $^{152}$Eu | 6.550 kBq (0.177 μCi) | ± 3.0 % | 14 January 2002 |
| $^{137}$Cs | 0.661 kBq (0.018 μCi) | ± 2.0 % | |
| $^{60}$Co | 1.907 kBq (0.052 μCi) | ± 2.0 % | |

**Table A. 5:** Soil sample; IAEA- 375 soil [Str96].

| Radionuclides | Recommended Values | Confidence Interval (Bq/kg) | N* | Reference date |
|---|---|---|---|---|
| Cs-134 | 463 | 454 - 472 | 87 | 31 December 1991 |
| Cs-137 | 5280 | 5200 - 5360 | 91 | |
| I-129 | $1.7\text{x}10^{-3}$ | $1.3\text{x}10^{-3}$ – $2.1\text{x}10^{-3}$ | 10 | |
| K-40 | 424 | 417 - 432 | 84 | |
| Ra-226 | 20.0 | 18.0 – 22.0 | 35 | |
| Ru-106 | 56 | 53 - 58 | 26 | |
| Sb-125 | 77 | 74 - 79 | 38 | |
| Sr-90 | 108 | 101 - 114 | 43 | |
| Th-232 | 20.7 | 20.1 – 21.3 | 37 | |
| U-238 | 22.6 | 20.6 – 24.6 | 38 | |

**Table A. 6:** NMISA point sources [Nmi14]**.**

| Source ID | Activity (Bq) | Uncertainty at 1σ (Bq) | Relative Uncertainty at 1σ (%) | Reference Date & Time |
|---|---|---|---|---|
| NMISA Am-241 01 | 671 | ± 23 | ± 3.4 | 01 September 2014, 12h00 (SAST) |
| NMISA Ba-133 02 | 804 | ± 27 | ± 3.4 | |
| NMISA Co-60 01 | 1 073 | ± 36 | ± 3.4 | |
| NMISA Cs-137 01 | 1 322 | ± 46 | ± 3.6 | |
| NMISA Eu-152 03 | 1 209 | ± 62 | ± 5.1 | |
| NMISA Na-22 02 | 458 | ± 16 | ± 3.4 | |

# Appendix B

## MCNPX input file of $K_2SO_4$ source in MB sample holder geometry

```
Germanium detector and 1.0 litre Marinelli beaker setup (K2SO4 sample)
c
c *** CELL CARDS ***
c
c ** Detector information **
c
c *Germanium crystal*
1 1  -5.323   (33:-18:34) -1 18 -3  imp:p,e=1
c *Core cavity8
14 0         -33 18 -34             imp:p,e=1
c *Dead layer*
3 1  -5.323   (1:-18:3) -4 19 -6    imp:p,e=1
c *Al holder*
4 6  -2.700   (4:-19:6) -7 -6 19    imp:p,e=1
c *Vacuum space*
5 0           (7:-19:6) -10 -2 5    imp:p,e=1
c *Al cryostat*
13 6  -2.700  (10:2:-5) -30 -31 32  imp:p,e=1
c
c ** Sample holder information **
c * Marinelli Beaker *
c Air between detector and beaker
2 5  -1.20484e-3 (30:31) 32 -16 -15 imp:p,e=1
c MB wall
6 3  -1.65  (16:15) -17 20 -21      imp:p,e=1
7 3  -1.65  (22:-18) 17 -23 20 -25  imp:p,e=1
8 3  -1.65  -23 25 -26              imp:p,e=1
c Sample and air inside
9 4  -1.44   (17:21) 18 -22 -24    imp:p,e=1
10 5  -1.20484e-3    -22 24 -25     imp:p,e=1
c Air outside
11 5  -1.20484e-3   16 -27 -20 32   imp:p,e=1
```

```
12 5  -1.20484e-3  (23:26) 20 -27 -29 imp:p,e=1
c
c Copper lining
40  40  -8.920      (27:-32:29) -40 41 -42   imp:e,p=1
c lead castle
41  41  -11.324     (40:-41:42) -46 47 -48    imp:e,p=1
 c
c whole universe
999 0         46:48:-47            imp:p,e=0
c

c  SURFACE CARDS
c
33  cy 0.425       $ core diameter
34  py 4.58        $ top plane
1   cy 3.125       $ Ge crystal
3   py 6.13        $ top plane
18  py 0.18        $ bottom plane of Ge
4   cy 3.175       $ Dead layer
6   py 6.18        $ top plane
19  py 0.08        $ bottom plane of Dead layer
10  cy 3.353       $ vacuum space
2   py 6.53        $ top plane
5   py -0.27       $ bottom plane
7   cy 3.251       $ Al holder
c 9 py 0.01        $ bottom plane
c 11 py 6.34       $ top plane
15  py 7.50        $ Marinelli
16  cy 4.25        $
17  cy 4.43
20  py 0.00
21  py 7.68
22  cy 6.42
23  cy 6.60
24  py 11.474
25  py 13.00
```

```
26  py 13.18

27  cy 8.00

29  py 15.00

30  cy 3.503      $ Al cryostat

31  py 6.68       $ top plane

32  py -0.42      $ bottom plane

40  cy   8.2

41  py  -0.62

42  py   15.2

46  cy   18.2

47  py  -10.62

48  py   25.2


c  DATA CARDS

c

mode p e

cut:e j 0.02 j j j     $ E_cut(e) = 20 keV

c

sdef cel=9 rad=d1 ext=d2 erg=1.46083 axs=0 1 0 par=2

c

si1  0 13.019                $ thickness

si2  0.18001 11.276          $ extent

c

f8:p,e 1

c

fc18 Broadened spectrum, 0.2% at 1.33 MeV

f18:p,e 1

ft18 geb 0 0.002 0

c

fc28 Broadened spectrum, 0.8% at 122 keV

f28:p,e 1

ft28 geb 0 0.0029 0

c

e0  0 1e-5 1e-3 &

    0.01 3000i 3.10

c
```

```
c
m1   32000. 1
m3   6000. -0.3844
     1000. -0.0484
     7000. -0.5672
m4   19000. 2 $ K2SO4
     16000. 1
     8000.  4
c
m5   8000. -0.231781
     7000. -0.755267
     6000. -0.000125
     18000. -0.012827
m6   13000. 1
m40    29000. 1
m41    82000. 1
c
nps  1000000000
ctme 1440
print
```

# Appendix C

**Table C. 1:** Measured sources and background date and time

| Source | Geometry | Live time (s) | Date of measurement | Time of measurement |
|---|---|---|---|---|
| $^{241}$Am | Point source | 86400 | 15/12/2015 | 12:56:26 |
| $^{133}$Ba | Point source | 86400 | 14/12/2015 | 12:31:05 |
| $^{60}$Co | Point source | 86400 | 21/10/2015 | 14:16:22 |
| $^{137}$Cs | Point source | 86400 | 20/10/2015 | 09:43:38 |
| $^{152}$Eu | Point source | 86400 | 15/10/2015 | 15:41:05 |
| $^{22}$Na | Point source | 86400 | 17/12/2015 | 08:45:31 |
| $^{232}$Th | Marinelli beaker | 86400 | 22/12/2015 | 18:03:10 |
| $^{232}$Th | Pill bottle | 86400 | 28/10/2015 | 13:14:34 |
| $^{238}$U | Marinelli beaker | 86400 | 21/12/2015 | 17:10:27 |
| $^{238}$U | Pill bottle | 86400 | 02/11/2015 | 12:28:52 |
| $K_2SO_4$ | Marinelli beaker | 86400 | 25/01/2016 | 12:50:56 |
| $K_2SO_4$ | Pill bottle | 86400 | 03/11/2015 | 16:04:26 |
| KCl | Marinelli beaker | 86400 | 18/01/2016 | 11:10:58 |
| KCl | Pill bottle | 86400 | 29/10/2015 | 13:48:03 |
| Soil | Marinelli beaker | 86400 | 14/08/2017 | 15:11:10 |
| Liquid | Marinelli beaker | 86400 | 25/04/2017 | 16:02:01 |
| Background 1 | Empty lead castle | 237081 | 30/10/2015 | 16:20:37 |
| Background 2 | Empty lead castle | 402520 | 04/11/2015 | 15:05:50 |
| Background 3 | Empty lead castle | 494363 | 26/01/2016 | 16:15:48 |

**Gamma-ray spectra and efficiency calibration curves of sources.**

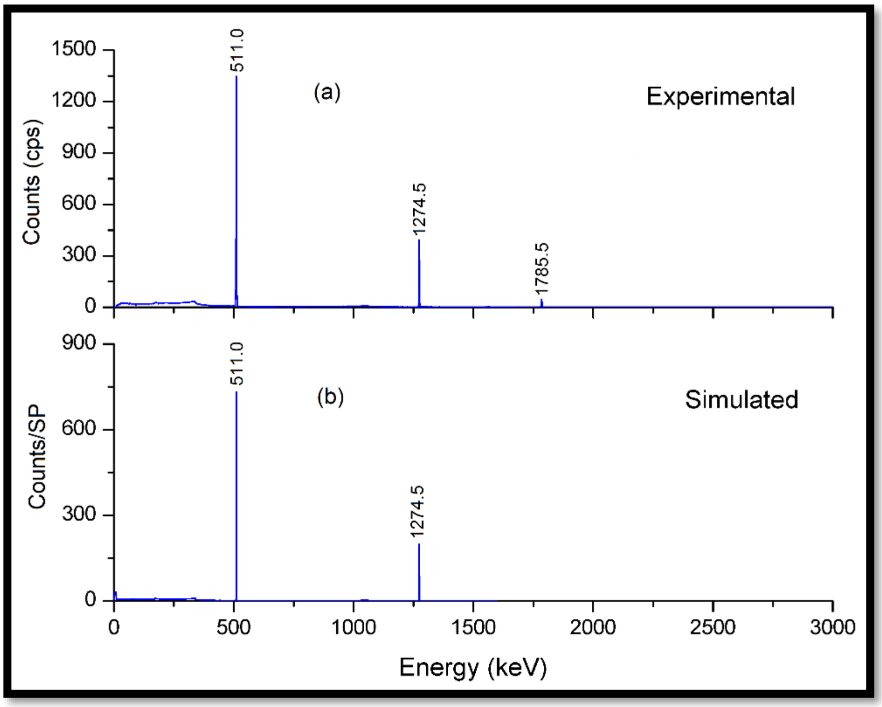

**Figure C. 1:** The γ-ray spectra for the $^{22}$Na for (a) experimental data and (b) simulated data.

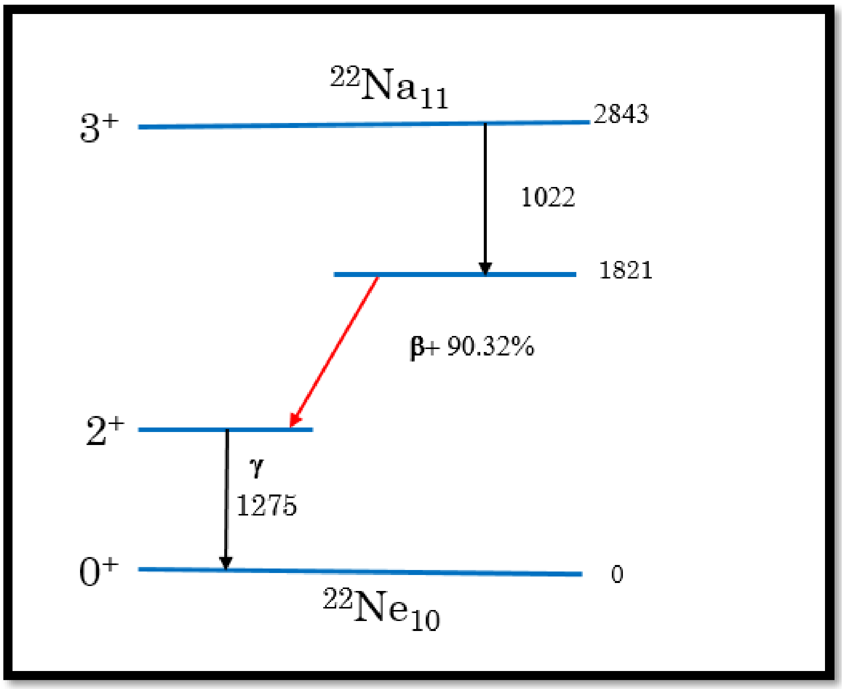

**Figure C. 2:** Decay scheme for the $^{22}$Na [Fir96].

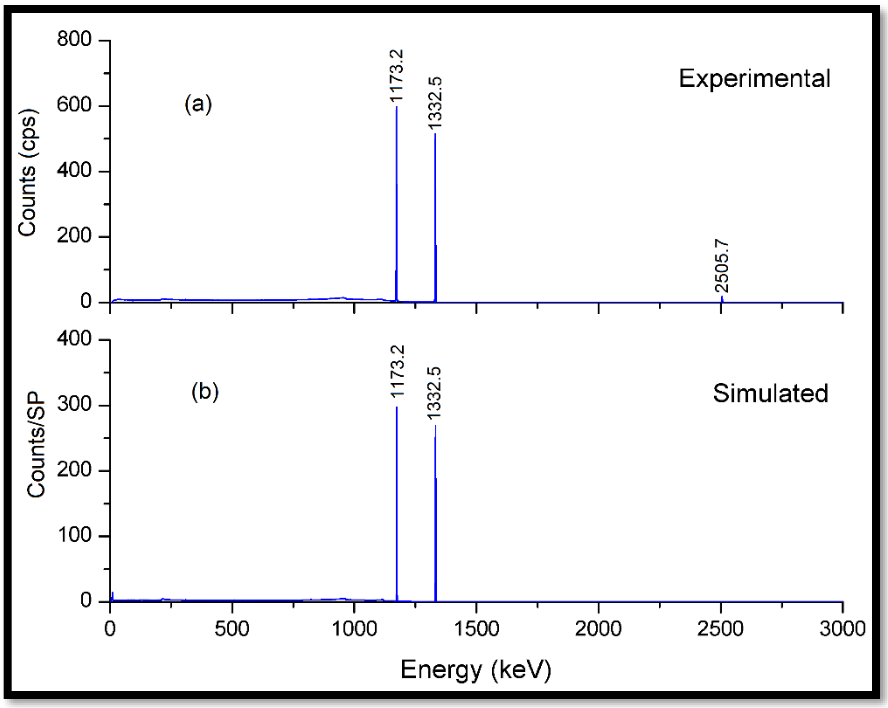

**Figure C. 3:** The γ-ray spectra of $^{60}$Co for (a) experimental data and (b) simulated data.

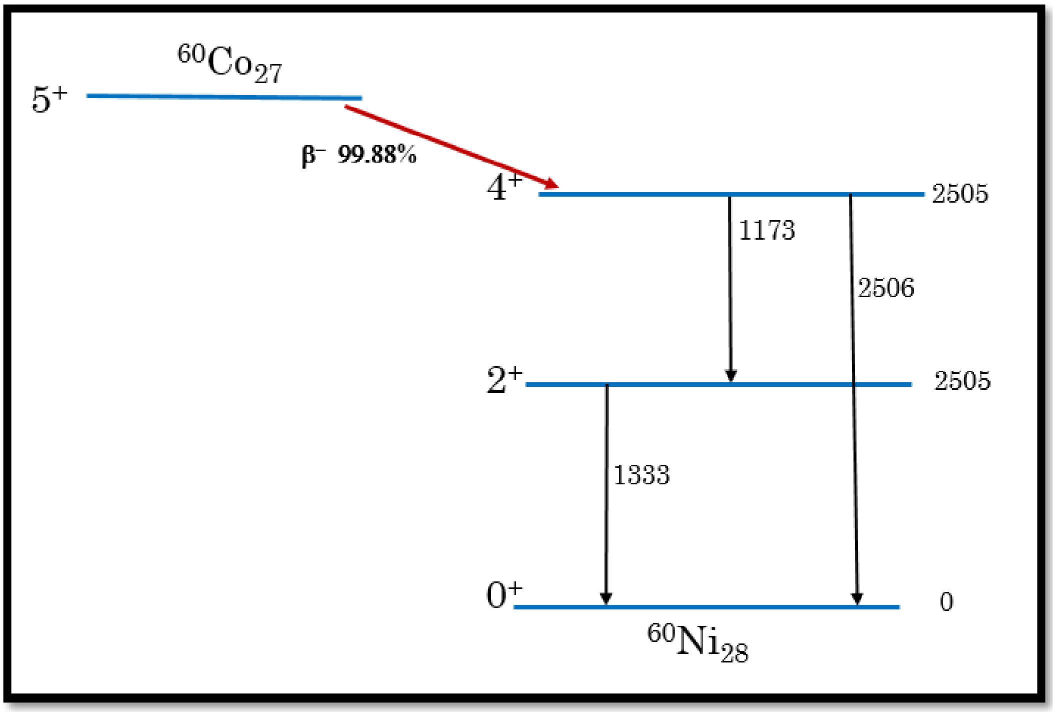

**Figure C. 4:** Decay scheme for the $^{60}$Co [Fir96].

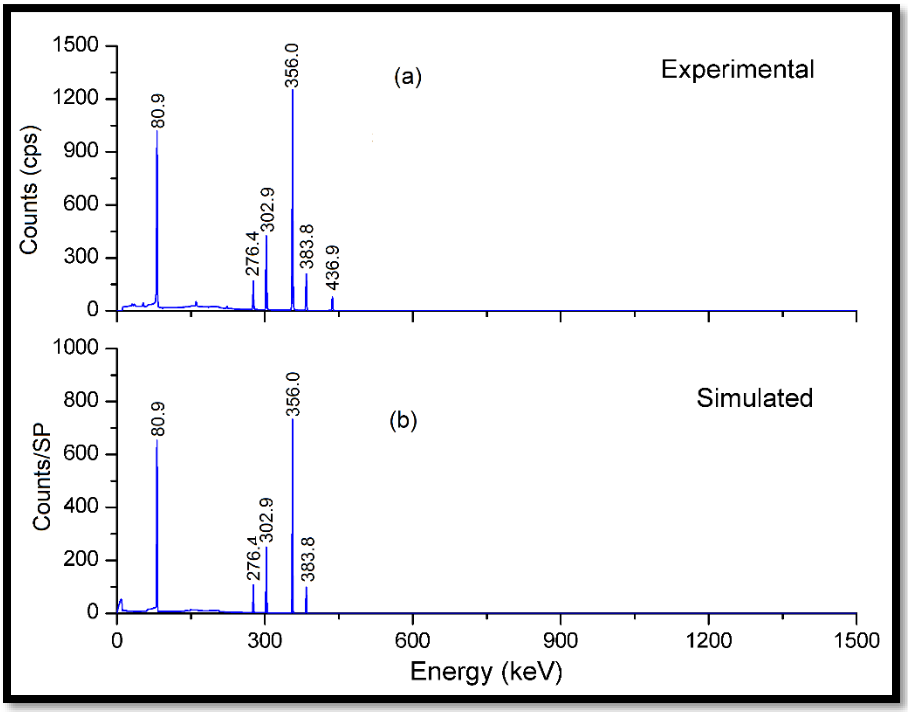

**Figure C. 5:** The γ-ray spectra for the $^{133}$Ba for (a) experimental data and (b) simulated data.

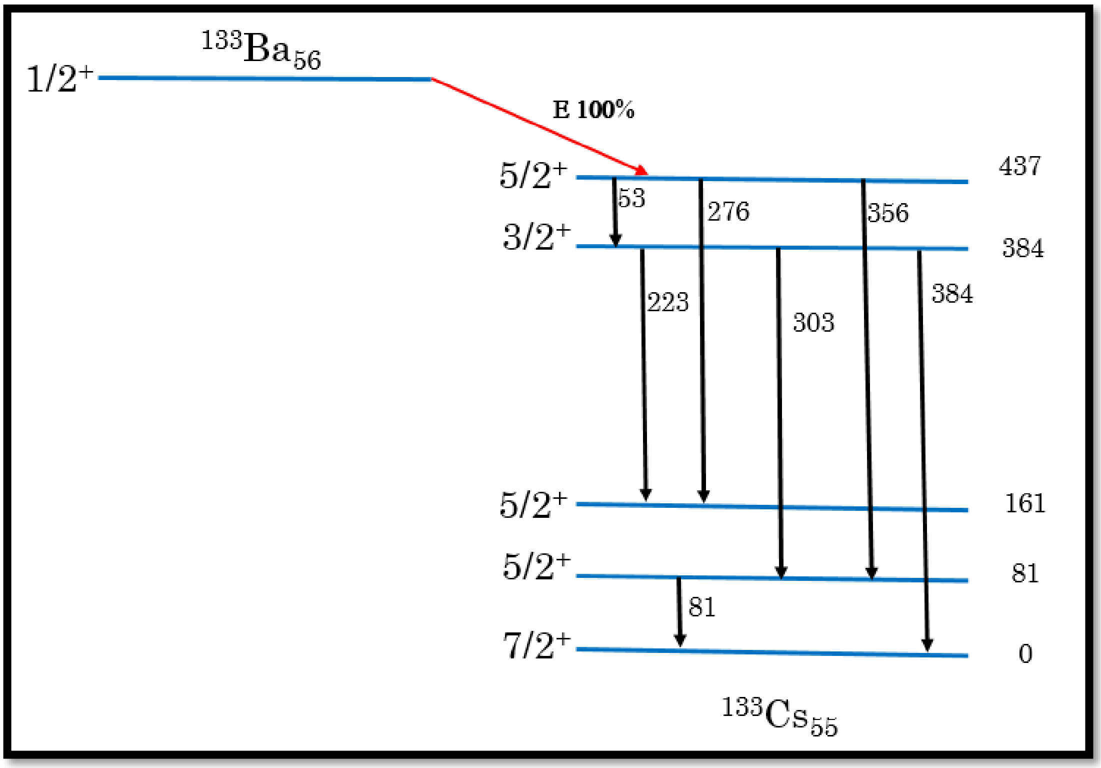

**Figure C. 6:** Decay scheme for the $^{133}$Ba [Fir96].

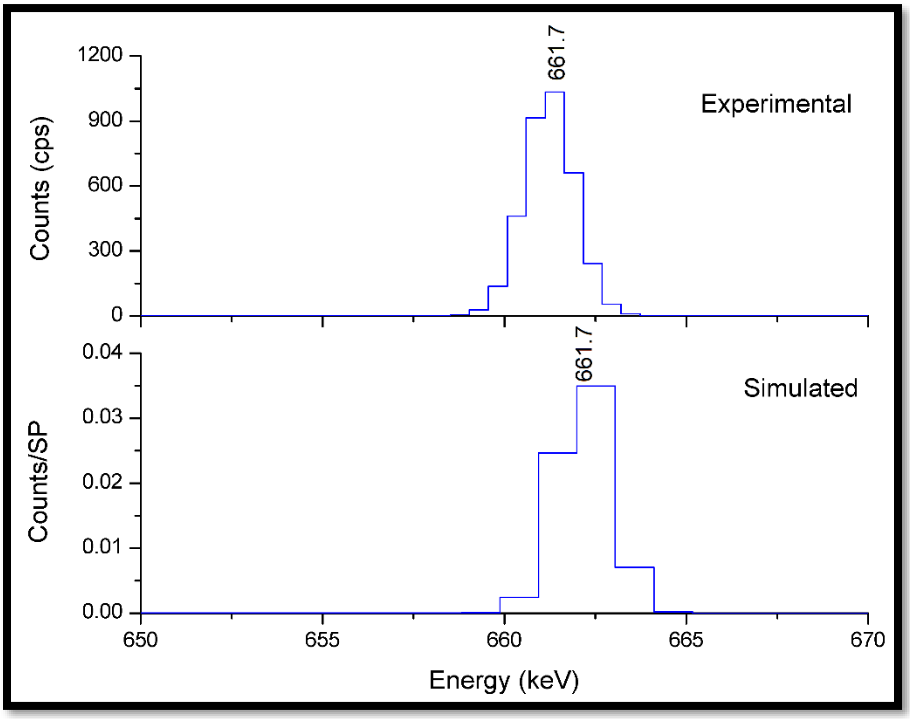

**Figure C. 7:** The γ-ray spectra for the $^{137}$Cs for (a) experimental data and (b) simulated data.

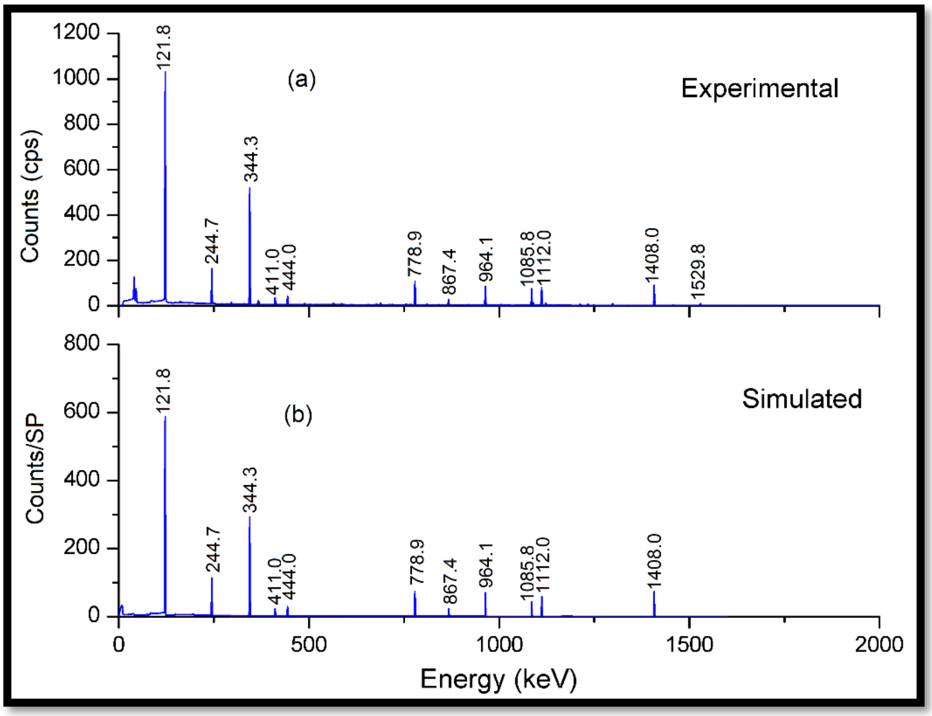

**Figure C. 8:** The γ-ray spectra for the $^{152}$Eu for (a) experimental data and (b) simulated data.

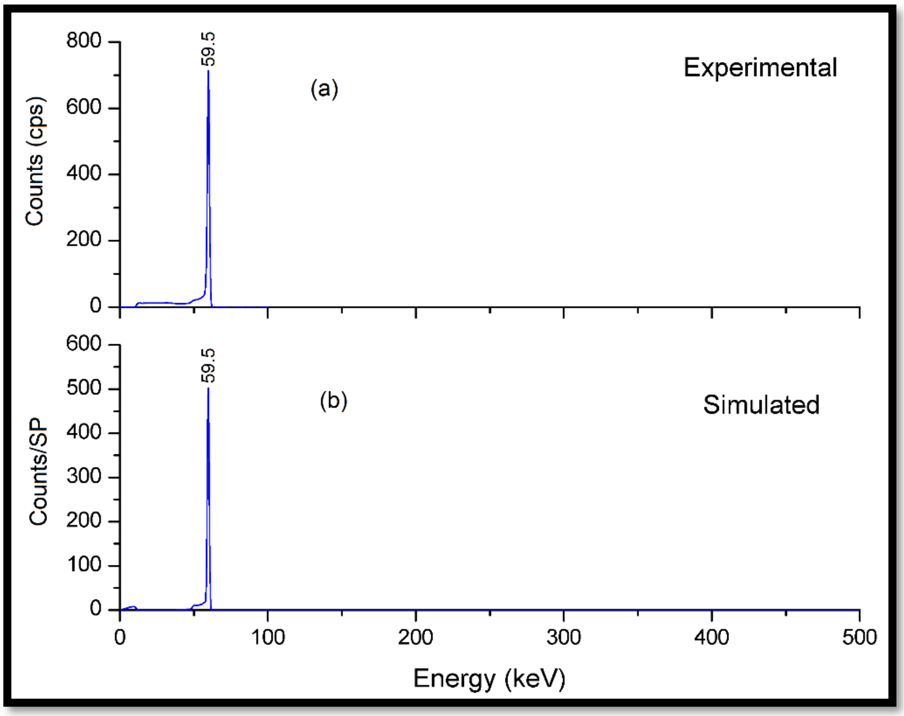

**Figure C. 9:** The γ-ray spectra for the $^{241}$Am for (a) experimental data and (b) simulated data.

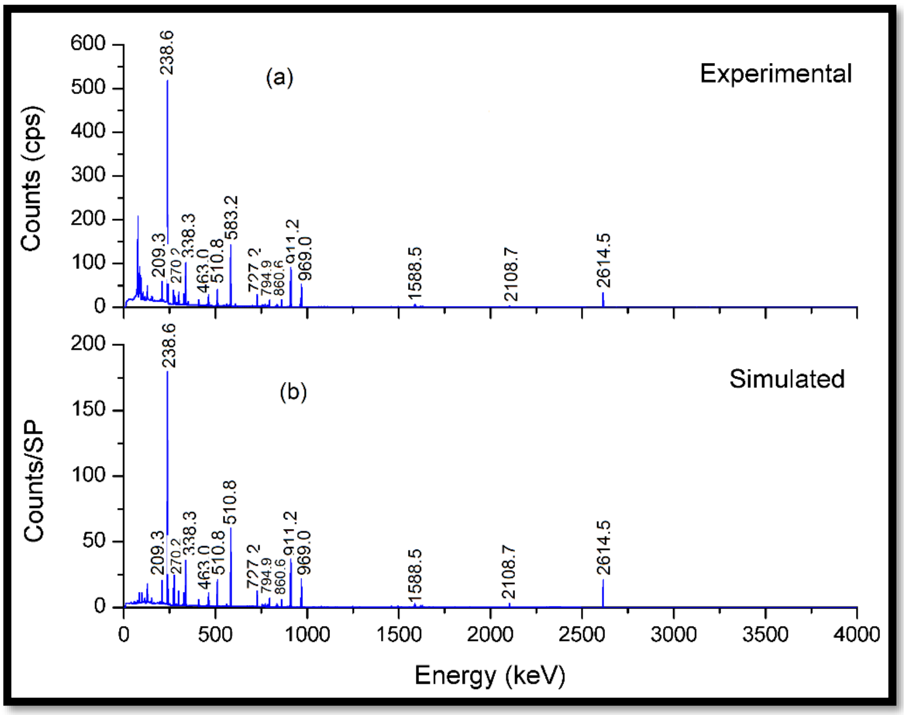

**Figure C. 10:** The γ-ray spectra for the $^{232}$Th for (a) experimental data and (b) simulated data in a PB.

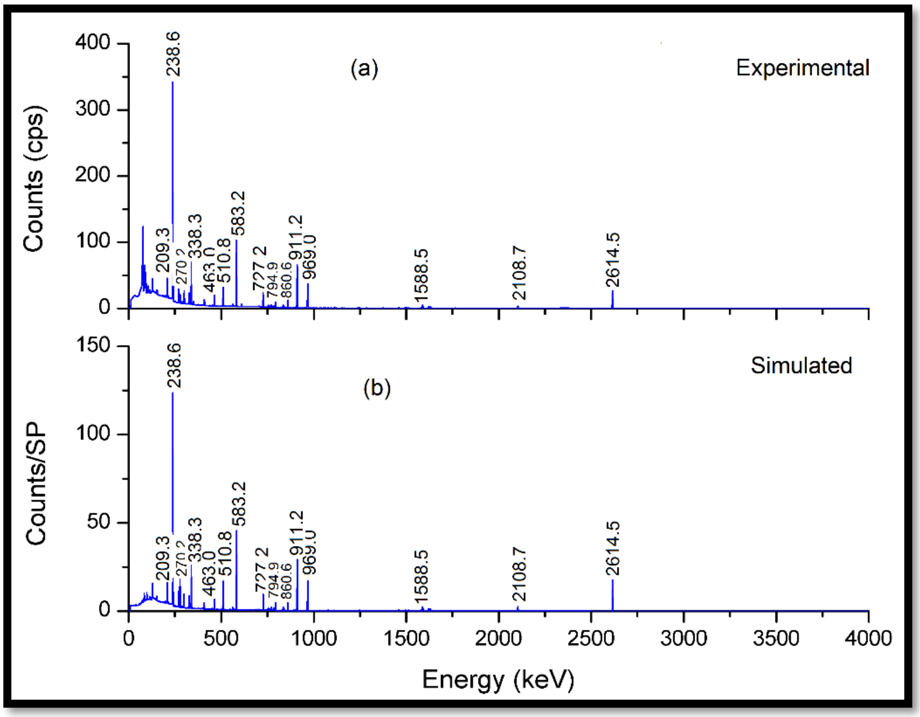

**Figure C. 11:** The γ-ray spectra for the $^{232}$Th for (a) experimental data and (b) simulated data for MB.

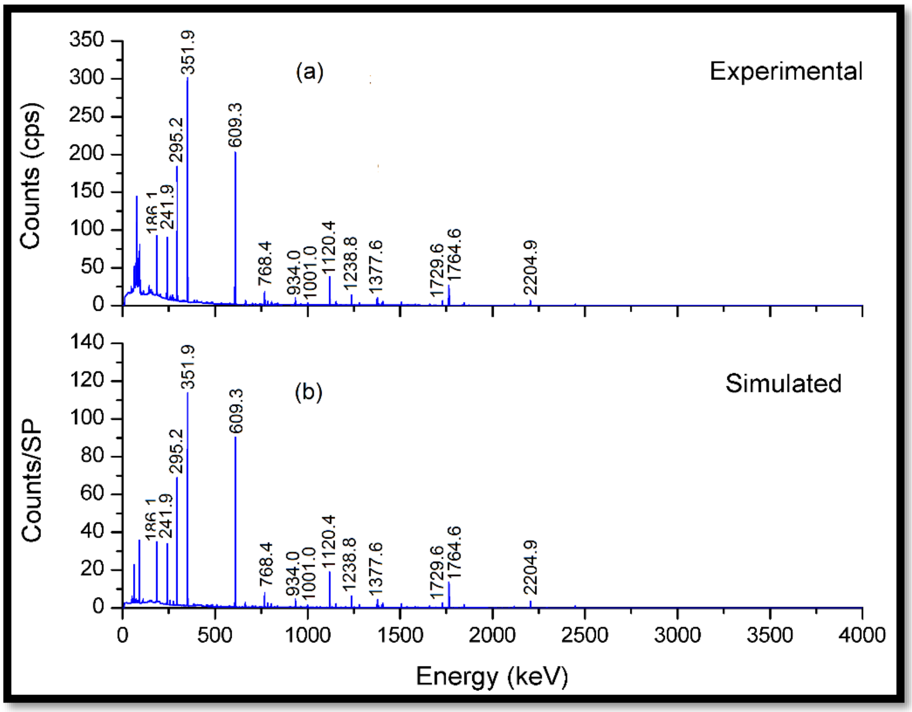

**Figure C. 12:** The γ-ray energy spectra for the $^{238}$U for (a) experimental data and (b) simulated data using PB.

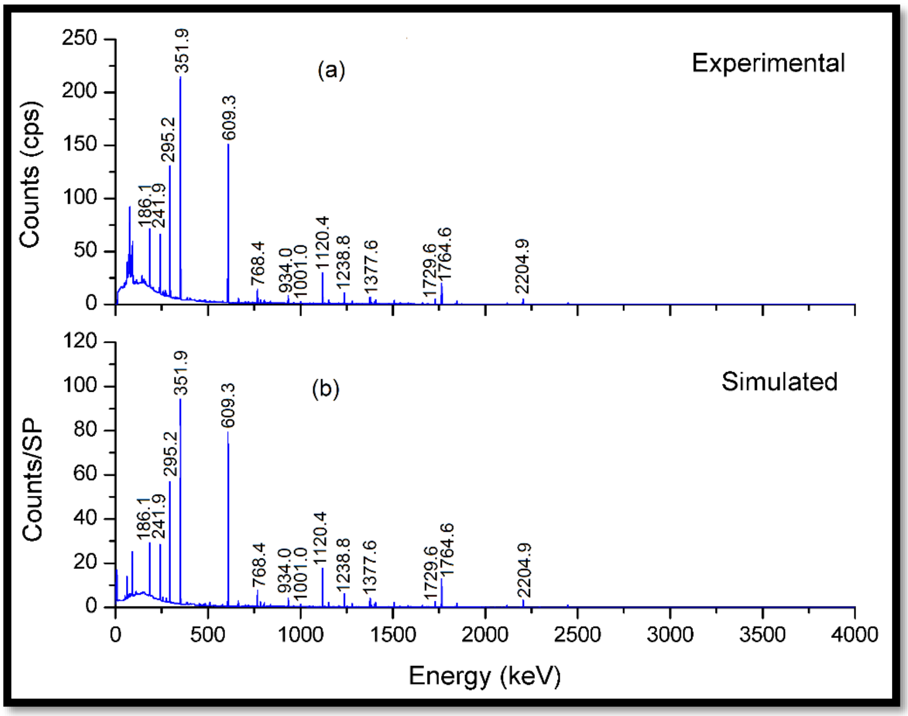

**Figure C. 13:** The γ-ray energy spectra for the $^{238}$U for (a) experimental data and (b) simulated data using MB.

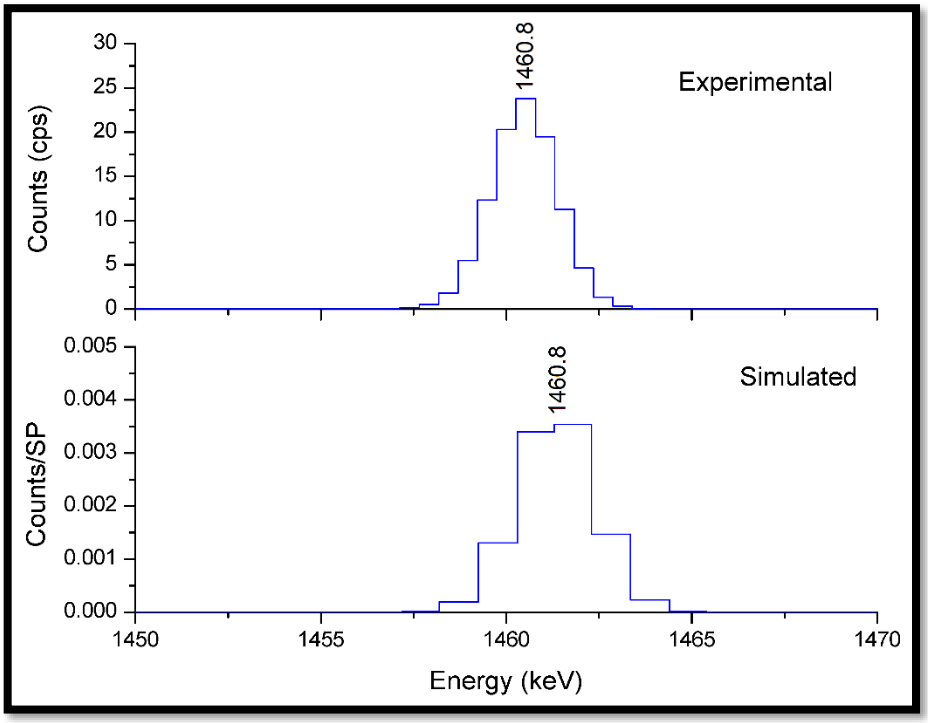

**Figure C. 14:** The γ-ray energy spectra for the $K_2SO_4$ source for PB from (a) experimental data and (b) simulated data.

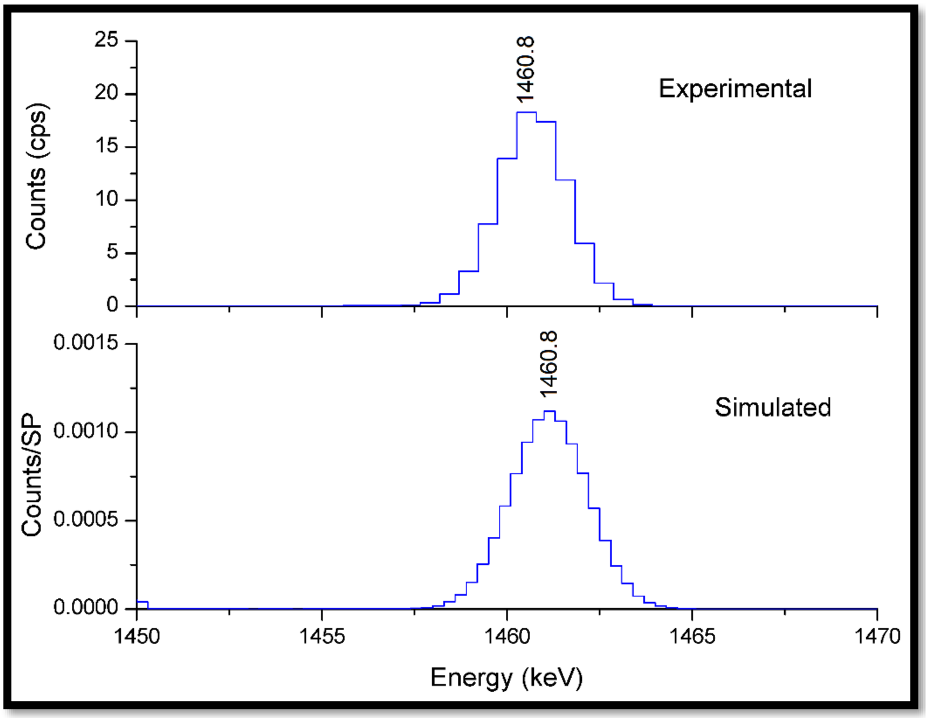

**Figure C. 15:** The γ-ray energy spectra for the $K_2SO_4$ source for MB for (a) experimental data and (b) simulated data.

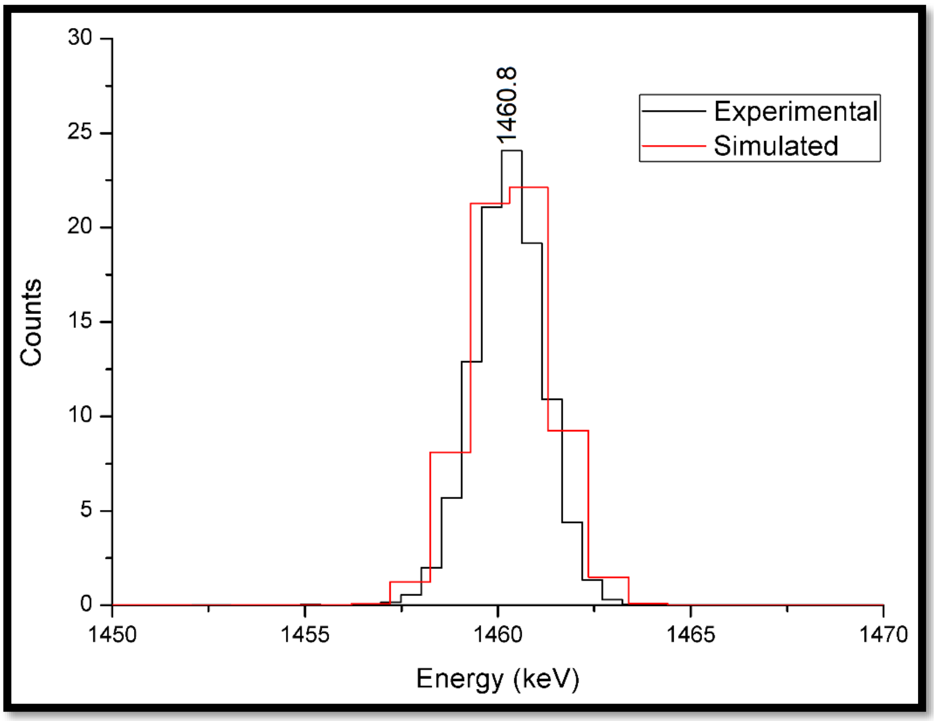

**Figure C. 16:** The γ-ray energy spectra for the KCl source for PB sample holder geometry.

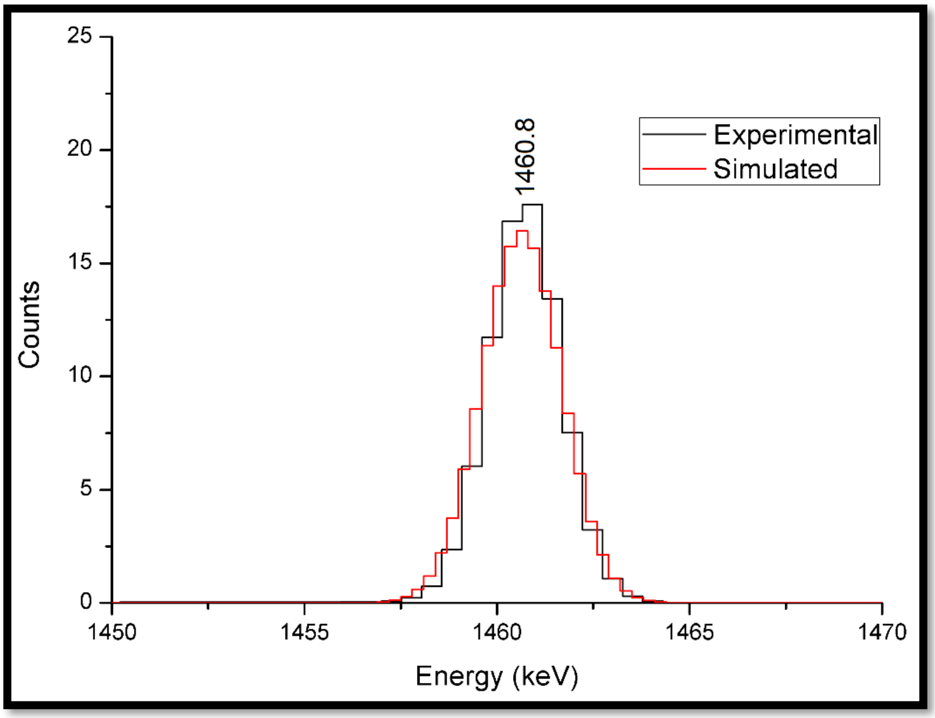

**Figure C. 17:** The γ-ray energy spectra for the KCl source for MB sample holder geometry.

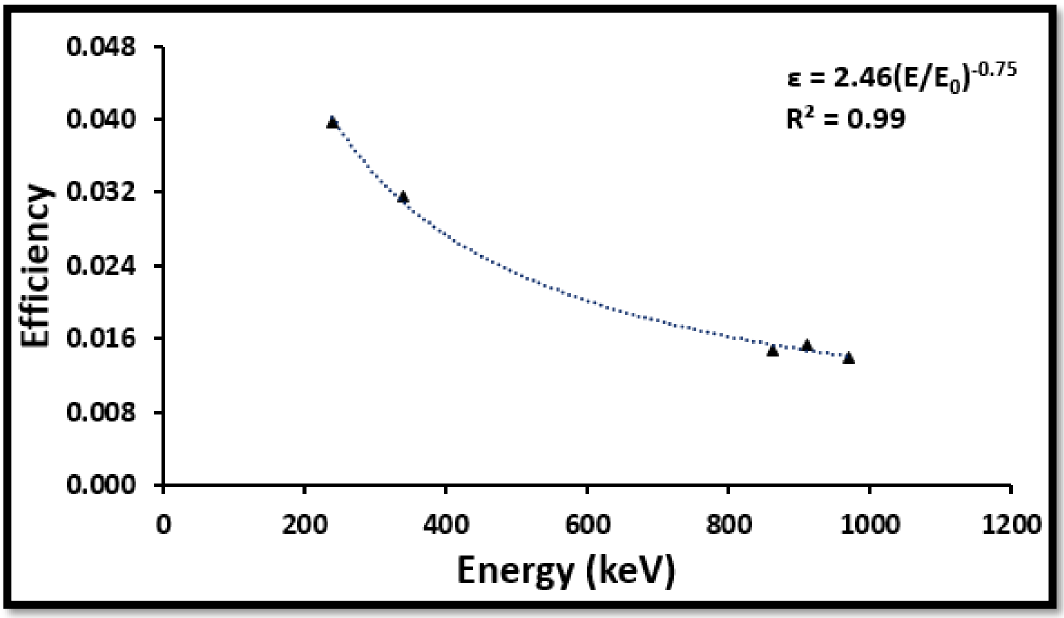

**Figure C. 18:** $^{232}$Th efficiency curve for PB sample holder geometry.

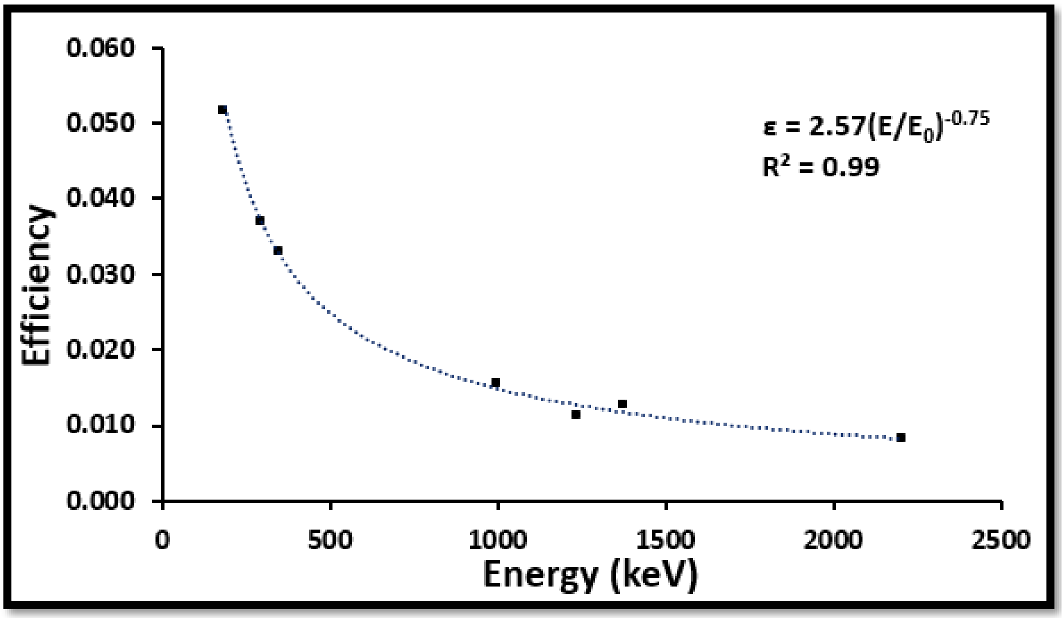

**Figure C. 19:** $^{238}$U efficiency curve for PB sample holder geometry.

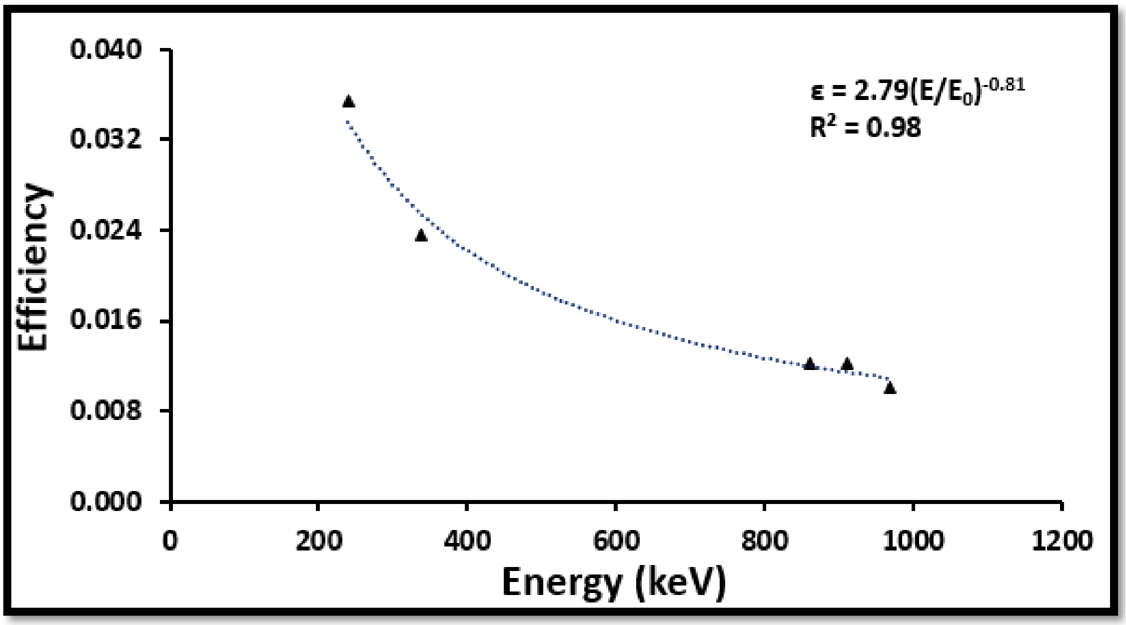

**Figure C. 20:** $^{232}$Th efficiency curve for MB sample holder geometry.

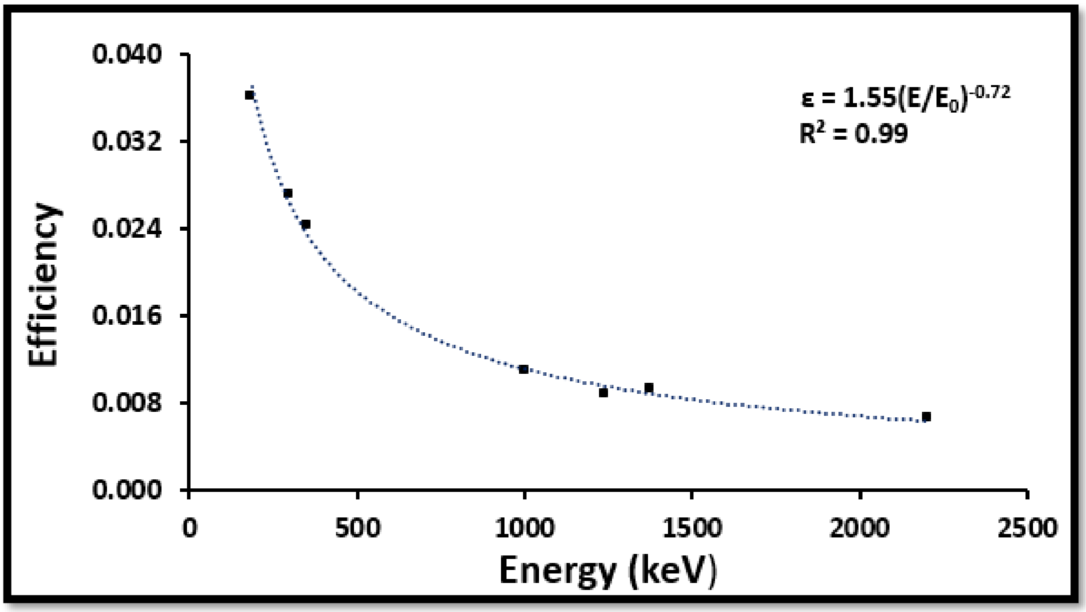

**Figure C. 21:** $^{238}$U efficiency curve for MB sample holder geometry.

**Table C. 2:** Simulated efficiency values as a function of density for various gamma-ray energies in PB.

| Densities (g.cm$^{-3}$) | Efficiency at 120 keV | Efficiency at 500 keV | Efficiency at 1000 keV | Efficiency at 1500 keV | Efficiency at 2000 keV | Efficiency at 2600 keV | Efficiency at 3000 keV |
|---|---|---|---|---|---|---|---|
| 1.0 | 0.0524 | 0.0214 | 0.0130 | 0.0098 | 0.0077 | 0.0061 | 0.0054 |
| 1.5 | 0.0473 | 0.0200 | 0.0125 | 0.0095 | 0.0076 | 0.0060 | 0.0053 |
| 1.8 | 0.0446 | 0.0194 | 0.0122 | 0.0094 | 0.0075 | 0.0059 | 0.0053 |
| 2.0 | 0.0431 | 0.0190 | 0.0121 | 0.0093 | 0.0074 | 0.0060 | 0.0052 |
| 2.5 | 0.0399 | 0.0180 | 0.0117 | 0.0091 | 0.0073 | 0.0059 | 0.0051 |
| 3.0 | 0.0371 | 0.0172 | 0.0112 | 0.0088 | 0.0072 | 0.0058 | 0.0051 |

**Table C. 3:** Simulated efficiency values as a function of density for various gamma-ray energies in MB.

| Densities (g.cm$^{-3}$) | Efficiency at 120 keV | Efficiency at 500 keV | Efficiency at 1000 keV | Efficiency at 1500 keV | Efficiency at 2000 keV | Efficiency at 2600 keV | Efficiency at 3000 keV |
|---|---|---|---|---|---|---|---|
| 1.0 | 0.0705 | 0.0316 | 0.0195 | 0.0145 | 0.0117 | 0.0092 | 0.0081 |
| 1.5 | 0.0660 | 0.0302 | 0.0188 | 0.0142 | 0.0115 | 0.0092 | 0.0079 |
| 1.8 | 0.0636 | 0.0293 | 0.0184 | 0.0140 | 0.0113 | 0.0091 | 0.0079 |
| 2.0 | 0.0623 | 0.0288 | 0.0182 | 0.0138 | 0.0112 | 0.0090 | 0.0078 |
| 2.5 | 0.0591 | 0.0276 | 0.0176 | 0.0135 | 0.0111 | 0.0088 | 0.0078 |
| 3.0 | 0.0565 | 0.0266 | 0.0172 | 0.0132 | 0.0109 | 0.0087 | 0.0077 |

**Table C. 4:** Density parameters a and b for the PB and MB.

| **Energy (keV)** | **Pill bottle** | | **Marinelli beaker** | | |
|---|---|---|---|---|---|
| | **a** | **b** | **a** | **b** | **Function** |
| 120 | 0.0531 | - 0.314 | 0.0712 | -0.202 | $\varepsilon = a\rho^b$ |
| 500 | 0.0216 | - 0.198 | 0.0319 | -0.156 | |
| 1000 | 0.0131 | - 0.133 | 0.0196 | -0.114 | |
| 1500 | 0.0099 | - 0.094 | 0.0146 | -0.084 | |
| 2000 | 0.0078 | - 0.07 | 0.0117 | -0.063 | |
| 2600 | 0.0061 | - 0.046 | 0.0093 | -0.048 | |
| 3000 | 0.0054 | - 0.048 | 0.0081 | -0.044 | |

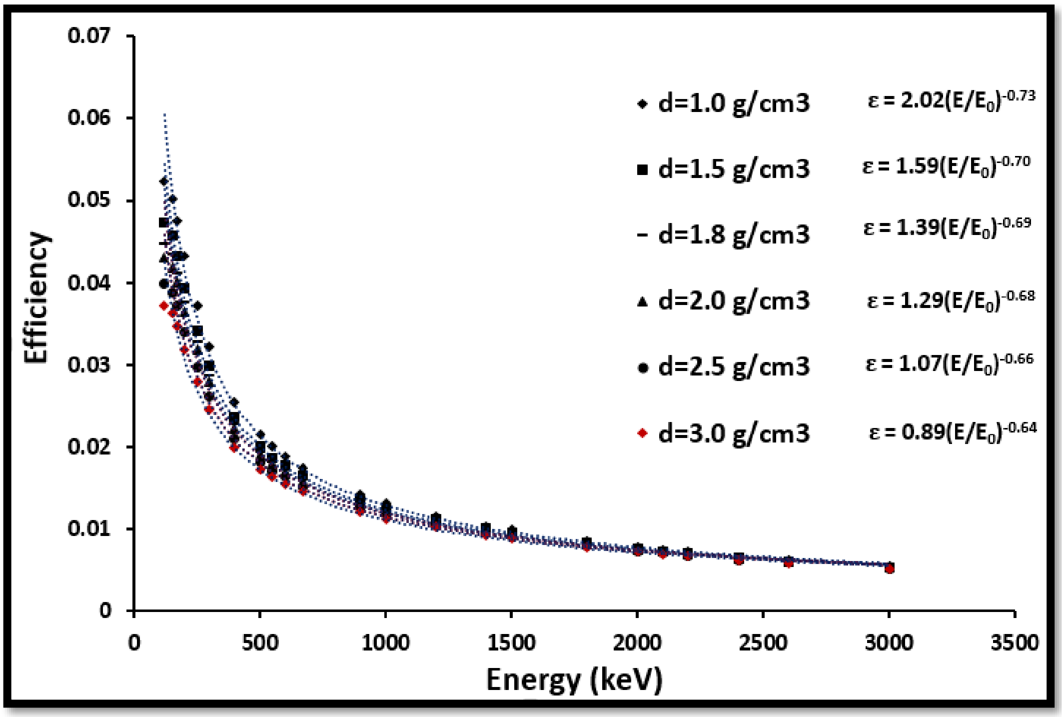

**Figure C. 22:** Efficiency curves at different densities for the PB sample geometry.

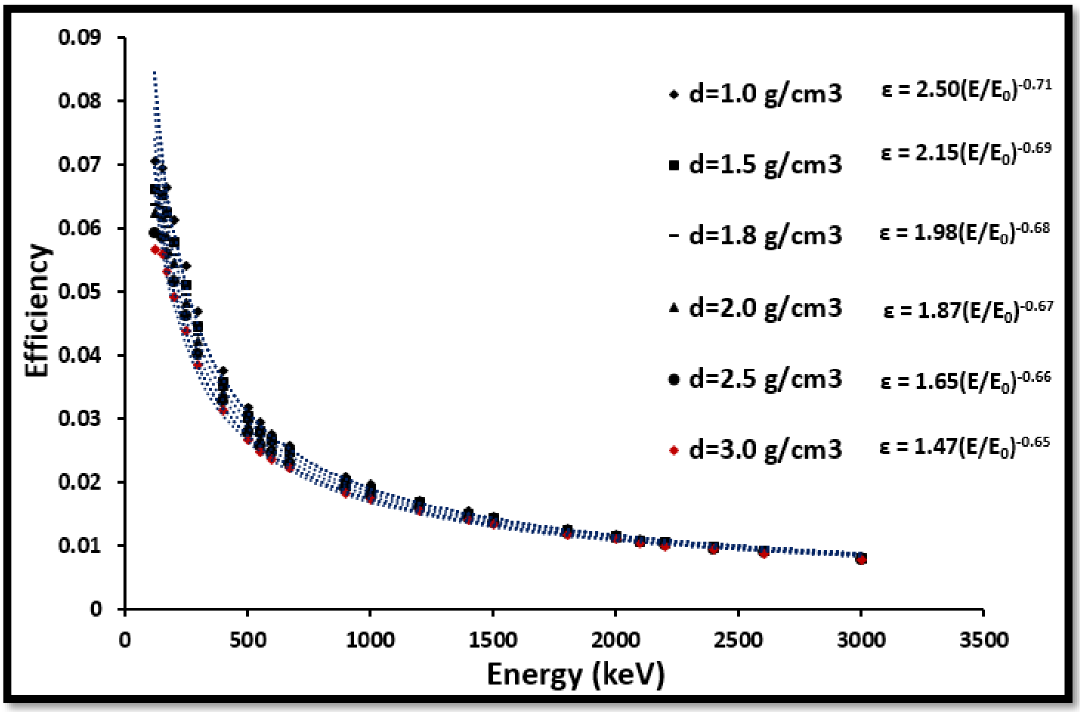

**Figure C. 23:** Efficiency curves at different densities for the MB sample geometry.

# References

[Azb15] Azbouche, A., Belgaid, M. and Mazrou, H., *Monte Carlo calculations of the HPGe detector efficiency for radioactivity measurement of large volume environmental samples*. Journal of Environmental Radioactivity 146 (2015) 119-124.

[Can99] Canberra Detector specification and performance data sheet supplied with the detector user's manual, 1999.

[Csi02] CSIR National Metrology Laboratory, Certificate RS\02-2 mixed volume source, Cape Town, 2002.

[Dam05] Damon, R.W. *Determination of the photopeak detection efficiency of a HPGe detector, for volume sources, via Monte Carlo simulation.* MSc thesis, University of the Western Cape. South Africa, 2005.

[Daz01] Daza, M.J., Quintana, B., Garcia-Talavera, M. and Fernandez, F., *Efficiency calibration of a HPGe detector in the [46.54-2000] keV energy range for the measurement of environmental samples.* Nuclear Instruments and Methods in Physics Research A 470 (2001) 520-532.

[DeM97] De Meijer, R.J., Stapel, C., Jones, D.G., Roberts, P.D., Rozendaal, A. and Macdonald, W.G., *Improved and new uses of natural radioactivity in mineral exploration and processing*. Exploration and Mining Geology 6 (1997) 105-117.

[Deb88] Debertin, K. and Helmer, R.G., (1988). *Gamma and X-ray spectrometry with semiconductor detectors.* Elsevier Science Publishers B.V. Amsterdam. Oxford.

[Ewa01] Ewa, I.O.B., Bodizs, D., Czifrus, S.Z. and Molnar, Z.S., *Monte Carlo determination of full energy peak efficiency for HPGe detector*. Applied Radiation and Isotopes 55 (2001) 103-108.

[Fad15] Fadhil, S.S., Kadhim, A.B., *Calculation of Full Peak Efficiency for HPGe Detector Using Monte Carlo Method*. Iraqi Journal of Science 56 (2015) 3246-3255.

[Fir96] Firestone, R.B., Chu, S.Y.F., Baglin, C.M., and Zipkin, J., (1996). *Table of Isotopes CD ROM (Ed. Shirley V.S)*. John Wiley and Sons, New York.

[Fuj09] Fujiyoshi, R., Satake, Y., and Sumiyoshi, T., *Depth profile of potassium and its isotopes ratio (K-40/K) in several forest soils.* Journal of Radioanalytical and Nuclear Chemistry 281(3) (2009) 553-561.

[Geh05] Gehreke, R.J., Davidson, J.R., *Acquisition of quality γ-ray spectra with HPGe spectrometers.* Applied Radiation and Isotopes 62 (2005) 479-499.

[Gil08] Gilmore, G., (2008). *Practical Gamma-ray spectrometry*. Second edition. John Wiley & Sons Ltd, Chichester, United Kingdom.

[Gra14] van der Graaf, E.R., Dendooven, P., and Brandenburg, S., *Using standard calibrated geometries to characterize a coaxial high purity germanium gamma detector for Monte carlo simulation.* Review of Scientific Instruments 85, 065110 (2014).

[Hen02] Hendriks, P.H.G.M., Maucec, M. and de Meijer, R.J., *MCNP modelling of scintillation-detector $\gamma$-ray spectra from natural radionuclides*. Applied Radiation and Isotopes 57 (2002) 449-457.

[Hla07] Hlatshwayo, N.I. *In-situ gamma-ray mapping of environmental radioactivity at iThemba LABS and associated risk assessment*. MSc thesis, University of Zululand. South Africa, 2007.

[Kno90] Knoll, G.F., (1990). *Radiation Detection and measurement*. Second edition. Wiley & Sons Inc., New York USA.

[Kno00] Knoll, G.F., (2000). *Radiation detection and measurement*. 3rd edition. John Wiley & Sons Inc., New York USA.

[Kno10] Knoll, G.F., (2010). *Radiation detection and measurement*. Fourth edition. John Wiley & Sons Inc., New York USA.

[Kra88] Krane, K.S., (1988). *Introductory Nuclear Physics*. John Wiley & Son Inc., New York USA.

[L'An07] L'Annunziata, M.F., (2007). *Radioactivity introduction and history*. (First edition). Elsevier, Amsterdam.

[Lab00] Laborie, J.M., Le Petit, G., Abt, D. and Girard, M., *Monte Carlo calculation of the efficiency calibration curve and coincidence-summing corrections in low-level gamma-ray spectrometry using well-type HPGe detectors*. Applied Radiation and Isotopes 53 (2000) 57-62.

[Leo87] Leo, W.R., (1987). *Techniques from Nuclear and Particle Physics Experiments*. Springer-Verlag Berlin Heidelberg.

[Lil01] Lilley, J., (2001). *Nuclear Physics Principles and Applications*. John Wiley & Sons Ltd, England.

[Lip13] Lipscy, P.Y., Kushida, K.E., and Incerti, T., *The Fukushima Disaster and Japan's Nuclear Plant Vulnerability in Comparative Perspective.* Environmental Science & Technology 47 (2013) 6082-6088.

[Liy06] Liye, L., Jizeng, M., de Carlan, L., and Binquan, Z., *Monte Carlo efficiency transfer method for full energy peak efficiency calibration of three type HPGe detectors: A coaxial N-type, a coaxial P-type and four BEGe detectors.* Nuclear Instruments and Methods in Physics Research A 564 (2006) 608-613.

[Mal10] Maleka, P.P. *In-situ Elemental analysis from gamma-ray and neutron spectra using a pulsed-neutron source. PhD thesis, University of Groningen. Netherlands, 2010.*

[Map04] Maphoto, K.P. *Determination of natural radioactivity concentrations in soil: a comparative study of windows and full spectrum analysis*. MSc thesis, University of the Western Cape. South Africa, 2004.

[Mba07] Mbatha, N.B. *Radiometric study of beach sand deposits along the coast of Western Cape province.* MSc thesis, University of the Western Cape. South Africa, 2007.

[Mic98] Michael, M. and Colm, O.S., (1998). *Understanding Physics*. John Wiley & Sons Inc., Chichester. New York.

[New08] Newman, R.T., et al., *Determination of soil, sand and ore primordial radionuclide concentrations by full-spectrum analyses of high-purity germanium detector spectra*. Applied Radiation and Isotopes 66 (2008) 855-859.

[Nmi14] NMISA certificate of measurements NMISA Am-241 01, NMISA Ba-133 02, NMISA Co-60 01, NMISA Cs-137 01, NMISA Eu-152 03 & NMISA Na-22 02, Cape Town, 2014.

[Oak99] Oak Ridge Associated universities, Marinelli (ca 1950), Donated by Ron Katherin,www.orau.org/ptp/collection/Miscellaneouse/marinelli.htm, (1999).

[Ong13] Ongori, J.N. *In-situ measurements and calculation of Radon gas concentration and exhalation from a tailings mine dump.* PhD thesis, University of the Western Cape. South Africa, 2013.

[Pel08] Pelowitz, D.P., (Editor). "MCNPX$^{TM}$ User's Manual, version 2.6.0." LA-CP-07-1473 Los Alamos Laboratory, (2008).

[Par03] Park, C.S., et al. *Determination of Single Escape and Double Escape Peak Efficiency for a HPGe Detector.* Journal of the Korean Nuclear Society, 35(6): 532-528,2003.

[Pre87] Preparation of Gamma-ray Spectrometry Reference Materials RGU-1, RGTh-1 and RGK-1 Report – IAEA/RL/148, Vienna, 1987.

[Qui96] Quintana, B., Fernandez, F., Wordel, R., and Mouchel, D., *Automatic analysis of continuum phenomena in gamma spectra.* Applied Radiation and Isotopes 47 (1996) 911-917.

[Sal17] Saleh, I.H., and Abdel-Halim, A.A., *$^{7}$Be in soil, deposited dust and atmospheric air and its using to infer soil erosion along Alexandria region, Egypt.* Journal of Environmental Radioactivity 172 (2017) 24-29.

[San12] Santawamaitre, T. *An Evaluation of the level of Naturally occurring Radioactive materials in soil samples along the Chao Phraya River Basin.* PhD thesis, University of Surrey. United Kingdom, 2012.

[Sed03] Sedumedi. L. *Radiometry of milk and mineral water from the Western Cape*. MSc thesis, North-West University. South Africa, 2003.

[Shu10] Shultis, J.K. and Faw, R.E., (2010). *An MCNP Primer.* Kansas State University. United States of America.

[Str96] Strachnov, V., et al., Report on the intercomparison run IAEA-375: determination of radionuclides in soil sample IAEA-375, IAEA/AL/075, Vienna, 1996.

[Tso83] Tsoufanidis, N.T., (1983). *Measurement and Detection of Radiation*. McGraw-Hill book company.

[Tyk95] Tykva, R., Sabol, J., (1995). *Low level environmental radioactivity sources and evaluation*. Techonomic Publishing Company, Lancaster, Pennsylvania.

[Rad16] http://radiopurity.in2p3.fr/conversion.html Accessed on 20/01/2016.

[Ram97] Ramos-Lerate, I., Barrera, M., Ligero, R.A., and Casaa-Ruiz, M., (1997). *A new summing-correction method for gamma-efficiency calibration with multi-gamma-ray radionuclides.* Nuclear Instruments and Methods in Physics Research, A, 395, 202-206.

[Rap16] www.rapidtables.com/convert/number/PPM_to_Percent.html#calculator Accessed 20/01/2016.

[Van15] Van Rooyen, J., (2015). *Transport and shielding of Ionising Radiation*. http://www.radiation-shielding.co.za Lecture notes, iThemba LABS, Cape Town, South Africa.

[Var03] Vargas, M.J., Diaz, N.C., and Sanchez, D.P., *Efficiency transfer in the calibration of a coaxial p-type HPGe detector using the Monte Carlo method.* Applied Radiation and Isotopes 58 (2003) 707-712.